2

Detonation of Gas–Particle Flow

F. Zhang

2.1 Introduction

Fine organic or metallic particles suspended in an oxidizing or combustible gas form a reactive particle–gas mixture. Explosion pressures in such mixtures are remarkably higher than those of gaseous fuel–air mixtures because of the high energy content of particles and the initial particle mass that transitions to explosion product gases. According to the component reactivity, detonation in particle–gas mixtures may be classified as:

1. "Heterogeneous detonation" in a reactive particle–oxidizing gas mixture
2. "Hybrid detonation" in a reactive particle–reactive gas mixture
3. "Dusty detonation" in an inert particle–reactive gas mixture

Reactive particles can be fuel particles or monopropellant particles that contain both fuel and oxidizer.

While dust explosions have been recognized from the beginning of coal mine exploitation, fundamental studies of heterogeneous detonation in gas–particle flow may trace their origin to the experimental work of Strauss [1] in 1968 for aluminum particle–oxygen mixtures, Nettleton and Stirling [2] in 1973 for coal dust–oxygen mixtures, Cybulski [3] in 1971 for coal dust–air mixtures, and Bartknecht [4] for other organic dust–air mixtures. Since then the fundamental heterogeneous detonation studies might be divided into two periods: global phenomenon studies between the 1970s and 1980s and transverse wave detonation studies since the late 1980s. Representative works in the first period include Wolanski and his coworkers [5,6] for coal dusts, Kauffman et al. [7] for grain dusts, and Peraldi and Veyssiere [8] for cornstarch. Most of the experiments were conducted in small tubes of a few centimeters in cross-sectional dimension by a few meters long, where solid particles were dispersed in pure oxygen to increase mixture sensitivity. The deflagration-to-detonation transition (DDT) observed in these experiments mainly exhibited a progressive nature where the flame was gradually accelerated to a quasi steady state without an abrupt onset of overdriven detonation accompanied

F. Zhang (ed.), *Shock Wave Science and Technology Reference Library: Heterogeneous Detonation*, DOI: 10.1007/978-3-540-88447-7_2,

by a retonation wave. The detonation velocities determined were up to 20–40% less than those predicted by the equilibrium Chapman–Jouguet (CJ) theory. While this phenomenon was termed "quasi-detonation" [9], its propagation mechanism remains a subject of current research. Some global phenomena of marginal spinning detonation were also observed in certain oxygen experiments [1]. In the same period, Wolanski et al. [10], Lee and Sichel [11], and Fan and Sichel [12] extended the one-dimensional Zeldovich–von Neumann–Döring (ZND) detonation model to the heterogeneous detonation where a generalized CJ condition was assumed at the phase-frozen or gaseous sound speed. Perhaps the most fundamental lesson learned in this period was that even when the explosion pressure is invaluably high, micrometric organic or metallic particles are not sensitive to detonation owing to the additional time scales inherent in the mass, momentum, and heat transfer between the finite-sized particles and the gas. Large tubes would be required to observe the DDT and propagation of a self-sustained heterogeneous detonation wave with a strong initiation and a sufficient tube length.

In 1982 Tulis and Selman [13] reported aluminum–air experiments in a 152-mm-diameter tube with a short length of 5.5 m and a 3-g condensed explosive for initiation. It was found that detonation was only achieved for flaked aluminum with a surface area to mass ratio of $3-4\,\mathrm{m^2\,g^{-1}}$, equivalent to spherical particles of diameter less than 1 μm. The observed detonation velocity fluctuated between 1,350 and 1,640 $\mathrm{m\,s^{-1}}$ with a deficit of 10–30% relative to the CJ values. Later, in 1991, Borisov et al. [14] reported more consistent aluminum–air detonation velocities between 1,700 and 1,800 $\mathrm{m\,s^{-1}}$ in a 122-mm-diameter tube for flakes and 1-μm atomized particles. A strong direct initiation of the detonation technique was employed owing to the short tube length of 4.2 m; thus, it was unclear whether the detonation wave observed was still influenced by the initiation. In 1986, Gardner et al. [15] for the first time clearly recorded the transition with a violent onset to detonation for a coal dust–air mixture in a tube 600 mm in diameter by 42 m in length. At the end of the tube, the transient velocity of the combustion wave reached 2,850 $\mathrm{m\,s^{-1}}$ and a peak pressure of 80 atm was measured. However, the tube, with a length–diameter ratio of 70, was still too short to record a self-sustained detonation wave. Since 1987, Zhang, Grönig, and their coworkers [16–20] have reported a number of conclusive results for the existence of a self-sustained detonation wave for particles suspended in oxygen and air through observation of the detailed transverse wave structure (spinning and cellular detonation) using a 140-mm- and a 300-mm-diameter tube with a length–diameter ratio larger than 120. The detonation waves observed for aluminum, anthraquinone, and cornstarch particles in air had a transverse wave spacing of 0.4–1 m with a velocity deficit less than 10% relative to the CJ values; the DDT was mostly characterized by an abrupt onset of overdriven detonation accompanied by a retonation wave. The large transverse wave spacing suggests that observation of unconfined detonation in reactive particle–air mixtures would require

a much larger scale than that of confined tubes and much stronger initiation. Evidence of the transverse wave structure has recently arisen for unconfined heterogeneous detonation [21, 22].

While a large transverse wave spacing is inherent to detonation in reactive particle–air flow, reactive particles added to a detonable gas mixture can cause a variety of detonation modes as a result of the interaction between the gas reaction and the additional physical processes involved in the mass, momentum, and heat transfer between the two phases. Fast deflagration of particles in gas detonation flow may enhance gas detonation or the DDT and has been referred to as "hybrid detonation" or "hybrid DDT" [23–25]. In 1982, Veyssiere [23, 24] reported for the first time the observation of a detonation wave composed of a double shock structure when aluminum particles were suspended in a lean reactive gas mixture in a 69-mm-diameter tube. In the same time period, Afanasieva et al. [26] theoretically postulated the existence of "double-shock" detonation in multiphase media due to two successive energy releases. Khasainov and Veyssiere [27] applied a two-phase ZND model to show that a "steady" double-shock detonation structure can exist, in which the two fronts are stabilized by a generalized CJ condition for the particle–gas mixture at two subsequent phase-frozen sound speed locations. Their further analysis explored the multiplicity of steady solutions for given initial conditions and nonmonotonic behavior of the heat release process [28]. Wolinski et al. [29] reported that the addition of oat particles into methane–air mixtures may promote methane–air detonation and that a secondary compression wave appeared owing to the late particle combustion. Recent experiments have provided more conclusive evidence on the self-sustained propagation of double-shock detonation for aluminum particles suspended in various detonable gas mixtures [30–33]. In an 80-mm-diameter, 10-m-long tube, Zhang et al. [32, 33] found that the double-shock detonation can quasi-steadily propagate in two modes: either the second shock has the same velocity as the leading shock, or the second shock velocity is less than the leading shock velocity. It was explained as the weak detonation solutions supported by the particle reaction in different time delays and energy release rates. The variety and complexity of hybrid detonation waves and their propagation mechanisms have yet to be fully understood and remain an active area of current detonation research.

It is noticeable that monopropellant or explosive particles can be added into particle–gas mixtures to increase the detonation sensitivity and readers can find relevant results, for example, in the work of Tulis et al. [34]. Detonation in layered dust is less sensitive than in the suspension and the DDT in layered grain dust was investigated by Li et al. [35] in a 300-mm-diameter, 70-m-long air-filled tube.

This chapter focuses on the physical phenomena of heterogeneous detonation and hybrid detonation for particles suspended in gas, while the features of dusty detonation are described briefly. The gas–particle detonation theory is introduced in Sect. 2.2, where particular characteristics of the equilibrium CJ model, the two-phase ZND model, and the unsteady two-phase fluid

dynamics model are discussed according to detonation types in gas–particle flow. Sections 2.3 and 2.4 concentrate on the heterogeneous detonation. The types of DDT in tubes and initiation of unconfined detonation are described, followed by a summary of the heterogeneous detonation velocity and pressure. The transverse wave structure that characterizes the heterogeneous detonation is then reviewed and the detonation dynamic parameters are discussed. In Sect. 2.5, the characteristics and limit of the quasi-detonation in reactive particle–oxidizing gas mixtures are examined. The important types of hybrid detonation and their influencing parameters are described in Sect. 2.6. This is followed by a brief concluding remark on the current state of the art and possible developments in the future. Finally, the governing equations of the two-phase fluid dynamics, the equations of state, and the transfer functions between two phases can be found in the Appendix for specific descriptions of modeling dilute and dense particle–gas flow topology.

2.2 Detonation Theory of Gas–Particle Flow

2.2.1 Equilibrium CJ Detonation Model

The equilibrium CJ detonation theory assumes a detonation wave to be a strong discontinuity within which the chemical reaction has ended and produces a final equilibrium detonation products state at an equilibrium sonic locus with respect to the detonation wave. A unique steady solution to the one-dimensional conservation equations across the discontinuity can be found to correspond to the minimum detonation velocity solution where the Rayleigh line is a tangent to the final equilibrium Hugoniot curve. The CJ steady solution has been remarkably successful in predicting the detonation velocity in uniform gas, liquid, and solid matter for conditions well within the detonation limits, given a reasonable equation of state for the detonation products. The detonation pressure, temperature, and flow velocity obtained from the CJ theory can be considered as the mean values at a mean equilibrium sonic locus averaged over the cross section perpendicular to the direction of propagation. It has been experimentally difficult, however, to determine the sonic locus where the averaging can be taken behind the shock front [36–38], since in reality detonation waves have a limited thickness and a three-dimensional structure. The success of the CJ theory lies in the simplicity of assuming a strong discontinuity without the need to consider the details of chemical nonequilibrium processes and the detonation wave structure. This assumption, however, prevents one from gaining insights into the detonation initiation and propagation mechanisms responsible for predicting detonation velocity deficit, failure limits, and other dynamic parameters.

Apart from the chemical nonequilibrium process, detonation of a solid particulate two-phase mixture comprises other nonequilibrium processes of mass, momentum, and energy transfer between the two phases owing to the finite

sizes of solid particles. A full or final equilibrium state includes all chemical, mechanical (pressure and particle velocity), and thermal (temperature) equilibria between the phases. In general, the nonequilibrium momentum and heat transfer depend on the physical properties of the particles and do not have the same relaxation length scales as that of the mass transfer or chemical nonequilibrium processes. Since the CJ theory assumes a unique final equilibrium detonation products state at the equilibrium sonic locus, it cannot predict the detonation velocity precisely for finite-sized particulate mixtures with large interphase momentum and heat transfer length scales.

Figure 2.1 illustrates the predictability of the CJ theory by comparing the theoretical predictions from the Cheetah code with the experimental results obtained in various aluminum particle–RDX ($C_3H_6N_6O_6$) mixtures at a common initial mixture density $\rho = 1.66\,\mathrm{g\,cm^{-3}}$ [39]. While dense matter is used here owing to available experimental data, the conclusion is generally valid for dilute hybrid reactive mixtures as well. RDX was chosen owing to its oxygen deficiency. For sufficiently small particles (e.g., 0.1 µm), an increase in aluminum mass fraction results in a decrease in detonation velocity. The experimental detonation velocities are in agreement with the theoretical prediction, regardless of the reactive or chemically frozen nature of the particles. This fact clearly indicates the significance of the momentum and heat transferred to the particles during the process towards the mixture equilibrium state as the flow approaches the sonic locus. The momentum and heat

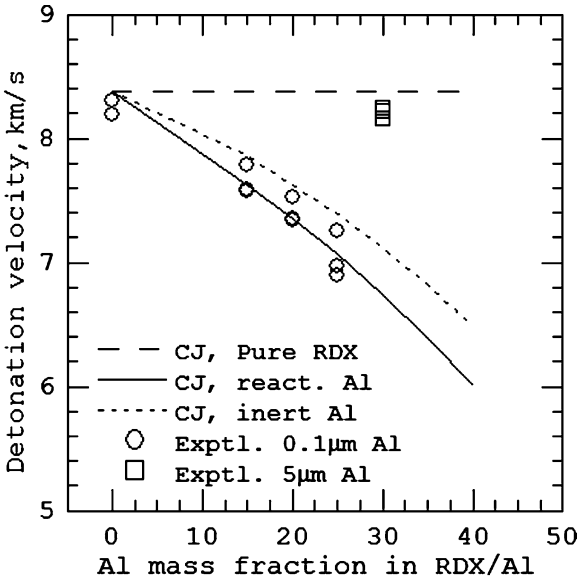

Fig. 2.1. Comparison of experimental detonation velocities with the equilibrium Chapman–Jouguet (CJ) theory for aluminum particle–RDX mixtures at $1.66\,\mathrm{g\,cm^{-3}}$ initial density

transferred are responsible for the velocity deficit with respect to pure RDX detonation. In contrast, for sufficiently large particles (e.g., 5 μm), the experimental velocity is much higher than the final equilibrium prediction and is close to that of pure RDX, thus suggesting a nearly frozen transfer of momentum and heat between the two phases within the detonation zone. The experimental detonation velocity is therefore a strong function of particle size and ranges between the final equilibrium value and the phase-frozen limit.

Detonation of reactive solid particulate mixtures can also result in condensed-phase products that do not contribute to gas pressure, thus reducing expanding work in sustaining the propagation of the detonation wave. For example, the CJ detonation can exist in an aluminum–oxygen mixture owing to the gas-phase detonation products of AlO and Al_2O at high detonation temperature. As the aluminum mass fraction increases, the condensed-phase products such as liquid Al_2O_3 and aluminum increase and the minimum detonation velocity as a unique steady solution is not attainable at the sonic point and instead is subsonic. Hence, there exists a limit for the amount of condensed-phase detonation products above which the CJ detonation solution does not exist.

2.2.2 Two-Phase ZND Detonation Model

The ZND detonation model in uniform matter developed by Zeldovich, von Neumann, and Döring assumes a detonation wave structure that consists of a leading shock front followed by a continuous reaction zone. The ZND model provides a mechanism for detonation propagation. The leading shock front adiabatically compresses a material to an autoignition temperature to initiate chemical reaction, while the expansion of high-pressure reacting gases in turn provides work to sustain the propagation of the shock front. A unique steady solution is obtained by integrating the one-dimensional ordinary differential conservation equations along the reaction progress path to the CJ sonic locus, where the Rayleigh line is tangential to the final equilibrium Hugoniot curve. To calculate detonation velocity deficits and detonation limits, Zeldovich and others [40, 41] further proposed a quasi-one-dimensional model in which the source terms are introduced in the conservation equations to consider lateral boundary effects such as friction and heat loss to the tube wall or expansion into the surroundings. Owing to the presence of loss source terms competing with exothermic reactions, the flow may become sonic prior to the final chemical equilibrium such that the ideal CJ equilibrium sonic condition is no longer valid. An alternative, referred to as the "generalized CJ condition," was introduced as a mathematical saddle point on which the exothermic heat release rate equals the energy loss rate at the gaseous sonic locus with respect to the shock front. For a reactive system with nonmonotonic heat release behavior, Kuznetov [42] demonstrated that the steady ZND solution may not be unique and multiple detonation solutions are possible for given initial conditions. Theoretically, the one-dimensional ZND structure can be unstable [43–49],

while observed detonation waves have an unsteady three-dimensional structure. Hence, the one-dimensional detonation wave structure (the profiles of pressure, temperature, and flow velocity along the reaction path) obtained from the steady ZND model may be regarded as a mean structure averaged over the cross section perpendicular to the direction of propagation, and over an unstable period in the propagation direction.

For solid particle–fluid mixtures, strictly speaking, a steady solution cannot be achieved a priori without integration along the reaction path to determine the mechanical and thermal partial equilibrium between the two phases. Hence, a two-phase ZND model has been introduced with a generalized CJ condition as a rear boundary condition, where the net heat release rate resulting from the chemical reactions and interphase nonequilibrium mass, momentum, and heat transfer approaches zero at the phase-frozen or gaseous sonic locus [10–12,27,28,50,51]. The two-phase ZND model can be derived from the one-dimensional, two-phase fluid dynamics governing equations based on the control volume analysis of the continuum theory. In this theory, the fluid and the solid particles are treated as two separated continua with mass, momentum, and energy conservation equations for each phase, continuity equations for species, and conservation equations for solid particle numbers. The interactions between the two continua are described using the source terms for the rate of mass, momentum, and energy transfer. Particle agglomeration or breakup is controlled through a source term for the rate of particle number change. When the solid particle flow is granular or extremely dense, a dynamic compaction equation can be employed where a source term is introduced to describe the rate of solid volume compaction [51–54]. The latter is caused by mechanical nonequilibrium between the internal stresses and the forces exerted by neighboring particles and the interpore fluid. If the reaction zone is large, the loss due to the tube wall or other lateral boundary conditions must also be included and modeled by the source terms for the rate of the momentum and heat exchange with the lateral boundaries. Various forms of source term functions can be found in [10–12,27,28,50–56]. Whereas in a rigorous multiphase continuum theory the source terms must follow constraints imposed by the conservation laws and the entropy inequality of the mixture, they are modeled on the basis of first principles physical rules, often in the form of empirical correlations. Therefore, appropriate choice of the source term functions for a particular flow topology is crucial for the reliability of the solution. The detailed description of the governing equations and some of the source term functions can be found in the Appendix.

From the governing equations in the coordinate frame with respect to the leading shock front propagating at velocity D, a system of ordinary differential equations can be derived in which the change of the fluid velocity u_g along the propagation distance x is given by

$$\frac{\mathrm{d}u_g}{\mathrm{d}x} = \Phi/\eta, \tag{2.1}$$

where

$$\eta = 1 - u_{\mathrm{g}}^2/a_{\mathrm{g}}^2 \tag{2.2}$$

is a sonic parameter of the flow with respect to the phase-frozen or gaseous sound speed a_{g}. The quantity Φ represents the "thermicity," a measure of the rate of net energy release from all nonequilibrium processes to molecular and bulk translational energy. A "generalized multiphase CJ condition" serves as the rear boundary condition at the phase-frozen or gaseous sonic point imbedded in the reaction zone by finding the common zeros of the thermicity Φ and the sonic parameter η:

$$\Phi = 0 \text{ at } \eta = 0. \tag{2.3}$$

The detailed expression of the thermicity depends on the nonequilibrium processes and equations of state. To elucidate the physical meaning of the net energy release rate, an analytical expression is given below for a simple system comprising a perfect gas with single exothermic (heat $q_{\mathrm{g}} > 0$ in joules per kilogram), irreversible gaseous reaction (rate $w_{\mathrm{g}} > 0$) and a negligible volume fraction of incompressible solid particles with exothermic particle combustion (heat $q_{\mathrm{p}} > 0$, rate of mass transfer $J_{\mathrm{p}} < 0$) and conservation of particle number:

$$\Phi = \frac{\gamma - 1}{\rho_{\mathrm{g}} a_{\mathrm{g}}^2} \left(\begin{array}{l} q_{\mathrm{g}} w_{\mathrm{g}} - (q_{\mathrm{p}} + cT_{\mathrm{p}}) J_{\mathrm{p}} \\ \qquad - \left[\frac{(u_{\mathrm{g}} - u_{\mathrm{p}})}{2} \left(\frac{\gamma+1}{\gamma-1} u_{\mathrm{g}} - u_{\mathrm{p}} \right) J_{\mathrm{p}} - \left(\frac{\gamma}{\gamma-1} u_{\mathrm{g}} - u_{\mathrm{p}} \right) f_{\mathrm{p}} + Q_{\mathrm{p}} \right] \\ \qquad + \left(\frac{\gamma}{\gamma-1} u_{\mathrm{g}} - D \right) f_{\mathrm{W}} + Q_{\mathrm{W}} \end{array} \right). \tag{2.4}$$

Variables ρ, u, and T here are the material density, flow velocity, and temperature, respectively; γ stands for the ratio of specific heats for the fluid and c is the specific heat for the solid phase. The subscripts p and g refer to the solid particle and fluid phase, respectively.

The first term on the right-hand side of (2.4) describes the energy release rate of the gas-phase reaction. The second term (with source term J_{p}) represents the rate of energy release into the gas due to particle reaction. Evaporation and combustion of solid particles are included in the rate of mass transfer J_{p}, which adopts a negative value when particle depletion occurs. The third term (in square brackets) corresponds to the rate of gas energy change caused by the nonequilibrium flow velocity and temperature between the two phases. The rate of momentum transfer f_{p} and the rate of energy transfer Q_{p} have the same sign as the phase velocity difference $u_{\mathrm{g}} - u_{\mathrm{p}}$ and phase temperature difference $T_{\mathrm{g}} - T_{\mathrm{p}}$, respectively. The last two terms (with f_{W} and Q_{W}) represent the rate of gas energy change due to the momentum and heat transfer to the tube wall or other lateral boundaries, and they become important in describing detonation limits. The value of f_{W} or Q_{W} is negative if the exchange results in a loss to the lateral boundaries and hence further competes with the exothermic terms for the flow to reach the sonic locus earlier. For finite-sized

particle–gas flow, the nonequilibrium momentum and heat transfer between the two phases described in the third term on the right-hand side of (2.4) can result in an energy loss rate competing with exothermic reaction rates of the first and second terms at the phase-frozen sonic locus, thus providing a mechanism that is possible to satisfy the generalized CJ condition shown in (2.3). To elucidate the intrinsic mechanism for the multiphase detonation, all discussions in this chapter, except when specifically noted, do not include lateral boundary source terms.

The generalized CJ condition (2.2)–(2.4) at the frozen sonic locus is derived from the steady gas-phase conservation equations of two-phase fluid dynamics equations and contains no information from the conservation equations for the solid particle phase. This limits the application of the model, particularly to detonation with very small particles whose velocity and temperature are rapidly equilibrated with gas velocity and temperature behind the shock front. In this case, the third term on the right-hand side of (2.4) would disappear. Equations (2.1)–(2.4), without lateral boundary source terms, indicate that the flow would approach the phase-frozen or gaseous sound speed as the chemical reactions [the first and second terms on the right hand side of (2.4)] reach an equilibrium state. This solution, however, conflicts with the CJ equilibrium solution where the flow approaches the phase-equilibrium sound speed as the mechanical, thermal, and chemical equilibrium is achieved. In fact, following a control volume analysis in a steady detonation frame one can find that the steady solution with respect to the phase-frozen sonic locus does not exist in this case as demonstrated in Fig. 2.2 (the minimum detonation Mach number as the unique solution is attainable at the control volume exit local Mach number $M_1 = 1$ with respect to the full equilibrium sound speed, while it is subsonic relative to the phase-frozen sound speed).

The phase-equilibrium sound speed a_e can be expressed by [57]

$$\left(\frac{a_e}{a_g}\right)^2 = \frac{(1-\alpha)}{(1-\phi_p)^2}\,\Gamma/\gamma, \quad \Gamma = \gamma\frac{1-\alpha+\alpha c/c_{pg}}{1-\alpha+\gamma\alpha c/c_{pg}}, \tag{2.5}$$

where $\alpha = \sigma_p/(\sigma_g+\sigma_p)$ is the mass fraction of the solid phase (σ denotes the partial density or mass concentration), ϕ_p refers to the solid volume fraction, c_{pg} stands for the specific heat of the gas phase at constant pressure, and Γ is defined as the ratio of the specific heats for the two-phase mixture. The solid particle material was assumed to be incompressible. From (2.5), the equilibrium sound speed is less than the frozen sound speed and their ratio decreases with increasing mass fraction of the solid phase. Hence, the fully equilibrated two-phase flow is still subsonic with respect to the frozen sonic speed as the CJ equilibrium detonation solution is achieved.

For the two-phase flow approaching $u_g = u_p = u$ and $T_g = T_p = T$ before the equilibrium sonic locus, the thermicity and the sonic parameter in (2.1) and (2.3) must therefore be rederived from the conservation equations of both the gas and the solid phase. They are

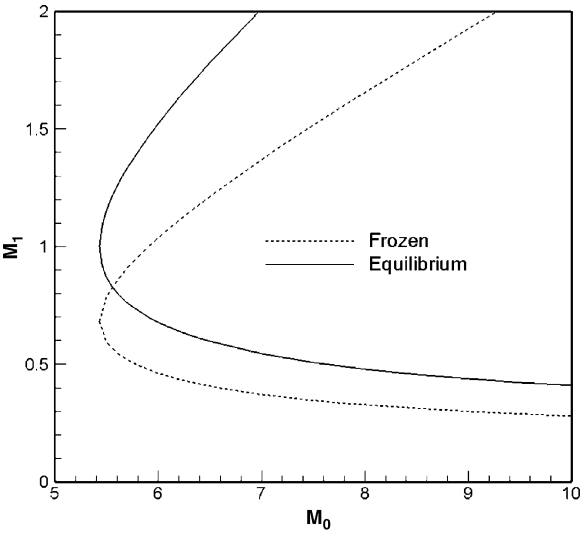

Fig. 2.2. Steady control volume solution for the local Mach number at the exit, M_1, as a function of detonation Mach number, M_0, with respect to the gaseous sound speed. The control volume has the initial $500\,\mathrm{g\,m^{-3}}$ aluminum and air at the entry and the detonation products including nitrogen and condensed aluminum and Al_2O_3 at the exit. The velocity and temperature equilibrium between the two phases is assumed at the exit [22]

$$\Phi = \frac{(\Gamma - 1)}{\rho a_{\mathrm{e}}^2}\left[q_{\mathrm{g}} w_{\mathrm{g}} - (q_{\mathrm{p}} + cT)J_{\mathrm{p}} - \frac{1 - \Gamma/\gamma}{\Gamma - 1} c_{\mathrm{pg}} T J_{\mathrm{p}} + \left(\frac{\Gamma}{\Gamma - 1}u - D\right) f_{\mathrm{W}} + Q_{\mathrm{W}}\right] \tag{2.6}$$

and

$$\eta = 1 - u^2/a_{\mathrm{e}}^2 \tag{2.7}$$

for the simple system used in deriving (2.4). Here, $\rho = \sigma_{\mathrm{g}} + \sigma_{\mathrm{p}}$ is the mixture density. The third term on the right-hand side of (2.6) is attributed to the change of the rate of the ratio of the specific heats for the two-phase mixture.

The ordinary differential equation system deduced from the governing equations, the equations of state for the particles and gas phase, together with the generalized CJ condition (2.3) form the closure of the mathematical description of the two-phase ZND model, given the source terms for the exchange between the two phases (and to the lateral boundaries if included). Here, the generalized CJ condition (2.3) contains Φ and η from (2.2) and (2.4) if $u_{\mathrm{p}} \neq u_{\mathrm{g}}$ or $T_{\mathrm{p}} \neq T_{\mathrm{g}}$ at the phase-frozen sonic locus, or Φ and η from (2.6), (2.7) if $u_{\mathrm{p}} = u_{\mathrm{g}}$ and $T_{\mathrm{p}} = T_{\mathrm{g}}$ at the full equilibrium sonic locus. Thus, under the initial conditions of the postshock state, a steady ZND solution can be obtained for the propagation velocity and reaction zone structure of the detonation wave in an inert particle–reactive fluid system, in a reactive particle–oxidizing fluid system, or in a reactive particle–reactive fluid system.

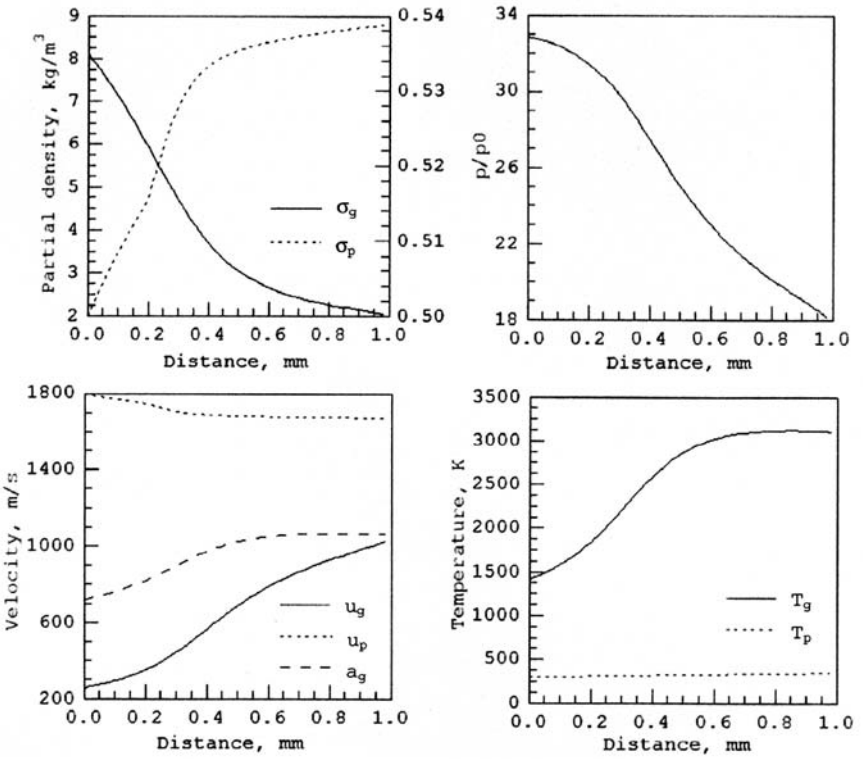

Fig. 2.3. Zeldovich–von Neumann–Döring (ZND) detonation structure in a mixture of stoichiometric C_2H_2–air and $\sigma_p = 500\,g\,m^{-3}$, $d_p = 10\,\mu m$ inert aluminum particles [55]

The steady ZND detonation structure in a dilute, inert particle–reactive gas system is analogous to a frictional detonation [58, 59], in which the frictional force is replaced by a drag force determining the momentum transfer between the two phases. Figure 2.3 shows an example in a mixture of stoichiometric acetylene–air (modeled by a single-step Arrhenius rate law) and 10-μm inert aluminum particles at $0.5\,kg\,m^{-3}$ concentration, where the detonation structure is terminated at the frozen sonic locus with the generalized CJ condition (2.2)–(2.4) [55]. The drag force influences the wave structure in two aspects. While it causes a shock velocity deficit with respect to the gas CJ detonation and therefore a drop in shock gas pressure and temperature, the drag compression in the gas reaction zone behind the shock front gradually amplifies the gas pressure and temperature. For the current particle size and concentration, the velocity and temperature relaxation length scales of the particle flow are 2 orders of magnitude larger than the gas reaction zone length. Thus, the drag compression is more than compensated for by the gaseous combustion expansion, so that the pressure monotonically

decreases from the shock front to the frozen sonic locus. While the combustion expansion causes the gas density to decrease behind the shock front, the particle concentration is gradually increased from the initial value owing to the velocity relaxation time lag in which the drag force drives the particles. The competition of the gas-phase chemical energy release with the momentum and heat transfer to the solid particles results in a detonation velocity $D = 1{,}800\,\mathrm{m\,s^{-1}}$ that has a mild deficit of 3.2% relative to the CJ velocity of the gas detonation ($D_{\mathrm{g-CJ}} = 1{,}860\,\mathrm{m\,s^{-1}}$), but an increase of 10% with respect to the full or final equilibrium CJ velocity ($D_{\mathrm{CJ}} = 1{,}632\,\mathrm{m\,s^{-1}}$).

A steady ZND detonation structure in a dilute, reactive particle–oxidizing gas system is illustrated in Fig. 2.4 for a $\sigma_{\mathrm{p}} = 0.5\,\mathrm{kg\,m^{-3}}$, $d_{\mathrm{p}} = 1\,\mu\mathrm{m}$ aluminum–air mixture modeled by the diffusion reaction model (2.45) and (2.46). The detonation structure consists of a shock front followed by an induction and reaction zone successively and is terminated at the equilibrium sonic locus where the generalized CJ condition (2.3) in combination with (2.6) and (2.7) is satisfied. In the induction zone, while the particles are heated through convective heat transfer from the shocked gas, the drag compression continuously increases the gas pressure, temperature, and particle concentration. Significant heat release of the particles into the gas takes place after the induction, and the resultant gas expansion causes the pressure to decrease

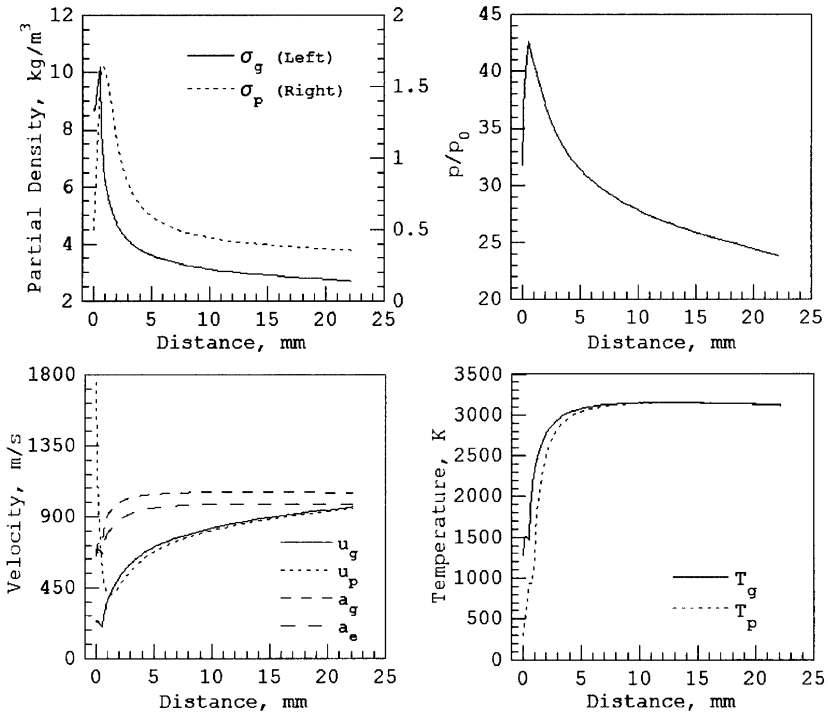

Fig. 2.4. ZND detonation structure in $\sigma_{\mathrm{p}} = 500\,\mathrm{g\,m^{-3}}$, $d_{\mathrm{p}} = 1\,\mu\mathrm{m}$ aluminum–air [55]

when the flow moves towards the sonic locus. Note that the two-phase velocity and temperature equilibrium are reached much before the equilibrium sonic locus in this example. Hence, the generalized CJ condition (2.2)–(2.4) at the frozen sound speed is not valid, as discussed before. In fact, the phase-equilibrated flow is still subsonic with respect to the frozen sonic speed a_g as the CJ equilibrium detonation solution [compatible to (2.3), (2.6), (2.7) with respect to the equilibrium sound speed a_e] is achieved. The expansion of the high-pressure gases provides the work to sustain the propagation of the shock front, which, in turn, supports the momentum and heat transfer between the two phases behind the shock front and the ignition of particles.

In general, this two-phase ZND structure has several significant differences from a ZND structure for homogeneous gas detonation. First, the shock front pressure (i.e., the von Neumann spike) in a gaseous detonation corresponds to the maximum pressure, while the maximum pressure for a reactive particle–oxidizing gas detonation wave may be found behind the shock front at a point at which the combustion expansion balances the drag compression. Second, the equivalence ratio of the particle–gas mixture behind the shock front does not remain the same as the initial value ahead of the shock front. The velocity relaxation time lag, in which the particle is accelerated towards the gas velocity before burning, results in a nonuniform equivalence ratio field behind the shock with a shift from the initial equivalence ratio of fuel particles to oxidizing gas towards a leaner value. This is clearly indicated in the partial density histories behind the shock front in Fig. 2.4 (the preshock initial values are $\sigma_g = 1.17\,\mathrm{kg\,m^{-3}}$ and $\sigma_p = 0.5\,\mathrm{kg\,m^{-3}}$). Third, the ZND structure can also be characterized by a melting phase change and an evaporation phase change (not included in this example) depending on the phase change models. Furthermore, combustion of metal particles such as aluminum may result in a large quantity of condensed metal oxide and therefore a mole decrement, thus leading to a pathological detonation when the products Hugoniot shifts to the left of the reactants Hugoniot. Finally, a high particle concentration layer can be formed downstream in the shocked flow under the appropriate conditions of a velocity relaxation time lag. Such a high particle concentration layer behind the shock was called a "ρ-layer" by Korobeinikov [60]. The late combustion of the dense ρ-layer and its influence on the detonation flow remain a subject of current research.

The generalized CJ locus determined by (2.2)–(2.4) is a mathematical saddle point, after which the subsonic flow relative to the shock front can become supersonic as it reaches the weak detonation branch of the full or final equilibrium Hugoniot curve. Two important conditions must be met for a steady weak detonation solution as follows:

1. The necessary conditions are:
   - Within the reaction zone, there is at least one phase-frozen sonic point imbedded at which the generalized CJ condition is satisfied.
   - The final equilibrium Hugoniot is not the upper bound of all partial equilibrium Hugoniot curves.

2. The uniqueness of a steady weak detonation solution depends on the flow or boundary conditions behind the generalized CJ point.

A simple illustrative example is the well-known detonation wave in a perfect gas with an irreversible exothermic reaction followed by a secondary irreversible endothermic reaction (heat releases $q_a > 0$, $q_b < 0, |q_a| > |q_b|$) [61]. It has a saddle point featured with the generalized CJ condition (2.3) imbedded in the reaction zone due to the endothermic reaction rate competing with the exothermic reaction rate. A steady solution can be obtained by integration of the ZND model from the postshock state downstream to satisfy the generalized CJ condition at which the Rayleigh line is a tangent to a partial equilibrium Hugoniot curve. This partial equilibrium Hugoniot corresponds to the highest attainable heat release of the system, $Q_{max} = q_a + q_b[1 - \exp(q_a/q_b)]$, which is larger than the heat release $Q_f = q_a + q_b$ in the final equilibrium Hugoniot. The detonation velocity D_m corresponding to the Rayleigh line tangential to the Q_{max}-Hugoniot is greater than the final equilibrium detonation velocity D_{CJ}. Therefore, the solution satisfies the necessary conditions for a weak detonation. Depending on the rear flow boundary conditions, the solution can return either to a strong detonation point along the D_m-Rayleigh line or continue the integration from the saddle point downstream, as the flow smoothly transits from subsonic to supersonic until it meets the final equilibrium Hugoniot curve. Hence, the solution is incomplete without taking into account the second condition stated above. A variety of weak detonation solutions can be obtained when the detonation wave is followed by a piston of specified constant velocity by adjusting the piston velocity [61].

For a gas–particle flow, a partial equilibrium state also includes that of mass, momentum, and energy transfer processes between the two phases. In fact, detonation in an inert particle–reactive gas system as shown in Fig. 2.3 satisfies the necessary conditions for a weak detonation. It has a saddle point imbedded in the reaction zone as depicted by the generalized CJ criterion (2.2)–(2.4). Secondly, the final equilibrium Hugoniot lies below some partial equilibrium Hugoniot curves because the final equilibrium detonation velocity ($D_{CJ} = 1{,}632\,\mathrm{m\,s^{-1}}$) is less than that shown in Fig. 2.3 ($D = 1{,}800\,\mathrm{m\,s^{-1}}$). After the gaseous sonic locus, the solid particle velocity and temperature will further equilibrate with that of the gas phase towards the final equilibrium Hugoniot as the flow becomes supersonic with respect to the leading shock front.

Detonation in a reactive particle–reactive gas system is analogous to the above example of two-irreversible-reaction gaseous detonation with the second reaction endothermic, followed by a piston of specified constant velocity. The momentum and heat loss from the gas to the particles provides a mechanism to satisfy the necessary conditions for a weak detonation, while various weak detonation solutions can be realized by the late particle energy release, in analogy to the piston, behind the saddle point. The energy release rate of particles represented by the second term in the thermicity (2.4), denoted now as $q_p' J_p$ in joules per cubic meter per second, is a characteristic parameter to

specify a possible solution. The delay time and the magnitude of $q_p{}' J_p$ can be adjusted through the particle material, size, or concentration as well as gaseous detonation parameters or product compositions.

2.2.3 Unsteady Two-Phase Fluid Dynamics Model

A steady solution can also be obtained by the long-time asymptotic solution of the one-dimensional unsteady two-phase fluid dynamics equations described in the Appendix, as the induction-to-reaction length ratio is below the value for the stability limit. A set of solutions for the detonation in a reactive particle–reactive gas system (lean acetylene–air with aluminum particles) are obtained as displayed in Fig. 2.5, serving for the quantitative description of physical

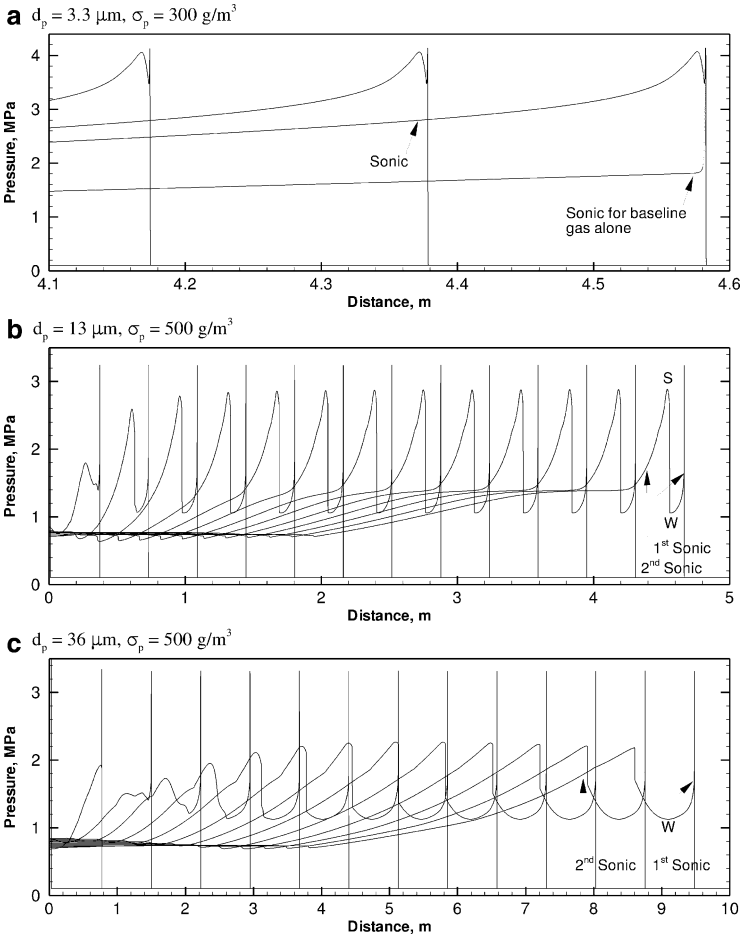

Fig. 2.5. Hybrid detonation solutions in a mixture of lean C_2H_2–air ($\varphi = 0.8$) and aluminum particles: **a** strong detonation, **b** type-I weak detonation, **c** type-II weak detonation

phenomena [32, 33]. The acetylene–air reaction is modeled by a single-step Arrhenius rate law and the aluminum reaction is modeled by the hybrid reaction model (2.49) to (2.52). The supersonic or subsonic flow terminologies used in the following discussions are with respect to the leading shock front:

1. If $q_{\mathrm{p}}' J_{\mathrm{p}}$ rises early and significantly, particle reaction can produce a compression wave in the gas reaction zone to increase the detonation velocity and pressure (Fig. 2.5a: 3.3 μm Al at $0.3\,\mathrm{kg\,m^{-3}}$). The entire subsonic reaction zone is substantially extended owing to particle combustion and a steady solution is reached when the generalized CJ condition (2.2)–(2.4) is satisfied at the gaseous frozen sonic locus. There exists a minimum in the pressure profile within the reaction zone when the net heat release reaches a local maximum at thermicity $\Phi = 0$ before the sonic locus. This solution was referred to as "single-front detonation" by Veyssiere and Khasainov [28], but is termed a "strong hybrid solution" in [32, 33] in the sense that particle combustion within the reaction zone overdrives the gas detonation. This terminology comes from the analogy with detonation in an exothermic–endothermic two-reaction gas followed by a piston moving faster than the flow velocity of the strong detonation point. However, unlike the usual overdriven detonation where the entire flow is subsonic with respect to the leading shock front, a strong hybrid detonation will not be disturbed by the supersonic rear flow behind the sonic locus. A strong hybrid detonation wave usually occurs for reactive particles suspended in a lean reactive gas mixture, where the rate of particle energy release into the gas overcomes the loss rate due to the momentum and heat transferred from gas to particles within the gas reaction zone. In a system of dense reactive particles suspended in a very rich reactive gas mixture, the strong hybrid detonation is unlikely to take place owing to the prevailing rate of momentum and heat loss that leads to a detonation velocity deficit and instability.
2. When $q_{\mathrm{p}}' J_{\mathrm{p}}$ is delayed and reduced to enable particle reaction behind the gas reaction zone, particles behave as though they are inert within the gas reaction zone and the necessary conditions for a steady weak detonation can be satisfied, where a generalized CJ point appears for the first time (Fig. 2.5b: 13-μm Al at $0.5\,\mathrm{kg\,m^{-3}}$). In the supersonic gas flow behind the first sonic point, heat release from the particles would cause a continuous decrease in gas flow velocity to subsonic levels, and an increase in gas pressure. This, however, will not match the downstream unsteady supersonic flow required by the rear boundary condition, and instead will result in thermal choking. Consequently, a second shock wave is necessary to adjust the gas flow behind the gas reaction zone from supersonic to subsonic. The flow, with the heat release from the particles, is then able to expand towards the second sonic locus, where the generalized CJ condition is satisfied a second time to match the downstream unsteady supersonic flow. Thus, a double-shock solution can be achieved that consists of the steady gas reaction zone followed by a secondary shock. The $q_{\mathrm{p}}' J_{\mathrm{p}}$-induced

second shock wave corresponds to a postshock subsonic state S and a preshock supersonic end point W of the steady gas reaction zone. If the Rayleigh line SW coincides with that for the leading front, the second shock moves with the same velocity as the leading front. This solution is referred to as the "type-I double-shock weak solution," analogous to the double-shock solution in the two-reaction gas followed by a piston velocity equal to the flow velocity of the strong detonation point.

3. When ${q_\mathrm{p}}'J_\mathrm{p}$ decreases, the velocity of the ${q_\mathrm{p}}'J_\mathrm{p}$-induced second shock wave is reduced. The shock therefore recedes from the supersonic end state W of the steady gas reaction zone to produce an ever-widening region of supersonic flow between state W and itself (Fig. 2.5c: 36-μm Al at $0.5\,\mathrm{kg\,m^{-3}}$). As ${q_\mathrm{p}}'J_\mathrm{p}$ further decreases, the strength of the secondary shock decreases and recedes more rapidly. This solution is called the "type-II double-shock weak solution," in analogy to the solution in the two-reaction gas followed by a piston with velocity between that of the strong detonation point and the weak detonation point. Unlike the weak detonation in the two-reaction gas followed by a piston, the ever-widening region of the supersonic flow is unsteady. The initial particle combustion increases the pressure and decreases the flow velocity upstream of the secondary shock. Furthermore, the particle reaction zone length between the second shock and the second sonic locus increases continuously as the shock recedes. Rigorously speaking, a steady solution does not exist after the end point W of the steady gas reaction zone.
4. As ${q_\mathrm{p}}'J_\mathrm{p}$ is further delayed and reduced, the supersonic end point W of the steady gas reaction zone is connected to the supersonic rear flow imbedded with a weak compression wave caused by the particle combustion. While the detonation front propagates steadily and satisfies the generalized CJ condition (2.2)–(2.4) at the frozen sonic locus, the particle-reacting rear flow of this type of weak solution is unsteady and subject to the rear boundary condition. The particles become chemically inert as ${q_\mathrm{p}}'J_\mathrm{p}$ is reduced to approach a null value.

The one-dimensional multiphase ZND model contains some intrinsic features in detonation instability. While reaction of particles within the fluid reaction zone stabilizes the detonation (e.g., Fig. 2.5a), the momentum and heat transferred from the fluid to the particles within the fluid reaction zone destabilize the detonation for any solid particle–reactive fluid systems. This momentum and heat transfer causes a velocity deficit with respect to the CJ detonation velocity of the pure fluid. For detonation in an inert particle–reactive fluid system, the magnitude of the velocity deficit increases with a decrease in a ratio of the velocity relaxation length scale of solid particles, L_p, to the fluid ZND detonation zone length, L_gr, that is,

$$\frac{L_\mathrm{p}}{L_\mathrm{gr}} \sim \frac{d_\mathrm{p}^n \rho_\mathrm{s}^m}{\sigma_\mathrm{p}^t L_\mathrm{gr}}, \tag{2.8}$$

where $n > 0$, $m > 0$, and $t > 0$ [55]. Thus, increasing particle concentration σ_{p}, or decreasing particle diameter d_{p} and material density ρ_{s}, will increase the detonation velocity deficit and instability. One can use numerical solutions of the unsteady two-phase fluid dynamics model to examine the validity of a steady ZND solution. For instance, for detonation in the inert particle–reactive gas system displayed in Fig. 2.3, L_{p} was 2 orders of magnitude larger than L_{gr}. Consequently, a small velocity deficit of 3.2% resulted and the long-time asymptotic unsteady solution appeared in accordance with the steady ZND solution. When $L_{\mathrm{p}}/L_{\mathrm{gr}} < 1$, rapid momentum and heat transfer within the gas reaction zone can result in a large velocity deficit, leading to failure of the detonation wave. For a range of intermediate values of $L_{\mathrm{p}}/L_{\mathrm{gr}}$, the detonation executes an unsteady oscillatory behavior and the oscillation irregularity increases as $L_{\mathrm{p}}/L_{\mathrm{gr}}$ decreases, indicating that the ZND multiphase model is unstable for a range of intermediate velocity deficits. The generalized CJ condition fails in unstable detonation waves and the detonation limits predicted by the unsteady solution appear to be more restricted than that obtained from the steady solution [55,58]. Caution must therefore be taken when using the steady solution to predict the detonation limits.

For detonation in a reactive particle–reactive gas system, Fig. 2.6 illustrates a numerical simulation for a large concentration of 10-μm aluminum particles suspended in a lean acetylene–air system [32]. In comparison with the steady double-shock detonation wave shown in Fig. 2.5b, an increase in particle concentration results in an increase in velocity deficit to 8%, thus causing the detonation wave to propagate in an unstable oscillatory mode. While the particles still burn behind the gas reaction zone, the energy release from the particle combustion is coupled with the unsteady rear flow of the

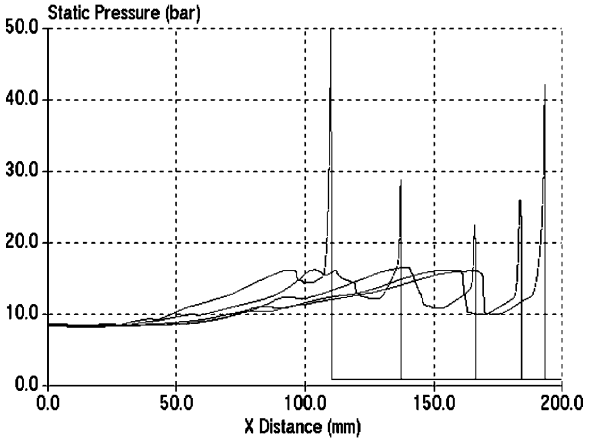

Fig. 2.6. Numerical simulation of unsteady weak hybrid detonation with a transient secondary pressure wave in a mixture of lean C_2H_2–air and 1,000 g m^{-3}, 10-μm aluminum particles [32]

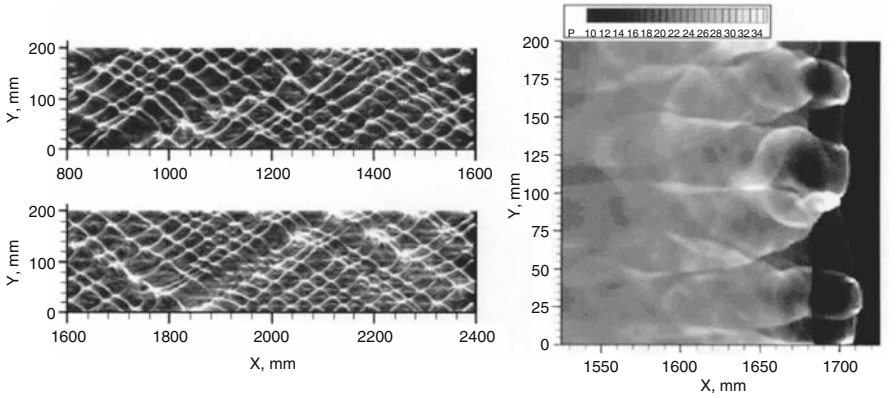

Fig. 2.7. 2D numerical cellular detonation in a mixture of lean H_2–air and $\sigma_p = 0.3\,\mathrm{kg\,m^{-3}}$, 13 μm aluminum. *Left*: Maximum pressure tracks. *Right*: Pressure distribution at 1 ms [62]

gas detonation. This leads to a transient pressure wave in the detonation flow in an oscillatory cycle with an acceleration phase followed by a deceleration phase. The acceleration phase leads to the formation of a shock wave before the deceleration phase commences. Figure 2.7 shows a cellular detonation solution in a mixture of 13-μm aluminum suspended in lean hydrogen–air using a two-dimensional two-phase fluid dynamics computation [a single-step Arrhenius rate law for gas and the diffusion reaction model (2.45), (2.46) for aluminum] [62]. The frontal transverse wave structure from the gas detonation is followed in a distance of about 20–30 mm by a nonplanar secondary shock due to aluminum combustion subjected to the transverse wave flow conditions. The detonation has a velocity deficit of 7.8% relative to the baseline gas detonation, thus leading to an unstable transverse wave structure that results in a more irregular cellular detonation than that of the baseline gas detonation.

A cellular detonation wave in a reactive particle–oxidizing gas system can also be simulated in a multidimensional instability analysis of the two-phase fluid dynamics model. Numerical studies have been conducted in an attempt to capture the nature of the cellular detonation wave in such a system using the Arrhenius reaction models [63–65] or the diffusion reaction model (2.45) and (2.46) [66]. For micrometric and nanometric aluminum–air mixtures, as to be reviewed in the next sections, experimental evidence showed strong dependence of detonation sensitivity on initial pressure and highly nonlinear behavior of detonation initiation and an abrupt DDT. This indicates the dependence of the aluminum detonation mechanism on chemical kinetics. On the other hand, the observed aluminum–air detonation manifested itself in a weak transverse wave structure as revealed by the small amplitude oscillation, which rapidly degenerates behind the shock front, and weak cell traces in the smoke foil records. This could suggest a functional dependence weaker

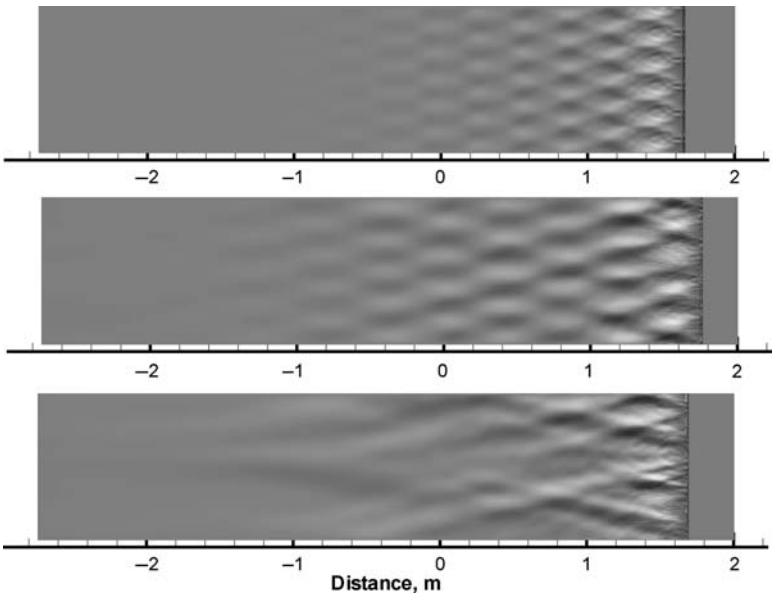

Fig. 2.8. Numerical shadow graph from the pressure data of 2D detonation simulation in a $\sigma_{\mathrm{p}} = 1{,}250\,\mathrm{g\,m^{-3}}$, 2-μm aluminum–air mixture at 2.5-atm initial pressure. *Top*: Activation energy $E = 71.1\,\mathrm{kJ\,mol^{-1}}$. *Middle*: $E = 95.5\,\mathrm{kJ\,mol^{-1}}$. *Bottom*: $E = 120\,\mathrm{kJ\,mol^{-1}}$ [67]

than the highly nonlinear Arrhenius kinetics for the later aluminum combustion. Hence, a surface kinetic oxidation and diffusion hybrid reaction model was suggested as described in (2.49) to (2.52) in the Appendix [22]. The hybrid aluminum reaction model that provides a kinetics-controlled induction and a diffusion-dominant combustion stage is successful in capturing both the kinetics-limited transient processes of detonation initiation, abrupt DDT, and detonation instability, and the diffusion-limited combustion of aluminum in the long reaction zone supporting the weak transverse wave structure [67]. Figure 2.8 presents two-dimensional cellular solutions using the hybrid reaction model in a rich 2-μm aluminum–air mixture at $\sigma_p = 1{,}250\,\mathrm{g\,m^{-3}}$ and an initial pressure of $p_0 = 2.5\,\mathrm{atm}$. As the activation energy in the aluminum induction stage increases, detonation instability indicated by the cell irregularity increases with an increase in detonation cell width from 0.18 to 0.22 to 0.28 m, respectively. For all activation energies used, the transverse waves are generally weak and rapidly degenerate behind the shock front. This is attributed to the slower diffusion-dominated combustion of the majority of aluminum mass after the kinetic induction and a considerable amount of condensed aluminum oxide without direct contribution to the gas pressure.

Finally, noting that the source term functions are modeled according to first-principles physical rules and empirical co-relations, we see that the reliability and the predictability of the two-phase continuum theory are strongly

determined by the choice of source term functions for a particular flow topology. For instance, in handling the momentum transfer in detonation of solid particles suspended in low-density gas flow, the shock interaction time in which the shock front crosses a particle is several orders of magnitude smaller than the velocity relaxation time related to the drag. Thus, a solid particle is assumed to remain stationary as the shock front crosses it [57]. In contrast, for detonation in high-density gas flow or condensed matter containing light metal particles, the shock interaction time can be comparable to the drag-induced velocity relaxation time owing to a significant increase in the initial material density ratio of fluid to particles. Mesoscale modeling showed that the post-shock velocity for aluminum particles achieved 70–80% of the shocked flow velocity of a liquid (Fig. 2.9) and the momentum transferred during the shock interaction time was a strong function of the initial fluid-to-particle material density ratio and the volume fraction of solid particles [39,68]. Hence, caution must be taken in employing appropriate source term functions with respect to the two-phase flow topology involved. Figure 2.9 also indicates that the hot spots are formed in the front of particles owing to the shock reflection and focusing effect as the shock front passes the particles. For condensed explosive mixtures containing metal particle additives, the critical charge diameter for detonation failure may decrease or increase, depending on the competing effects of the sensitization due to the formation of hot spots and desensitization from the momentum and heat transfer to the added mass.

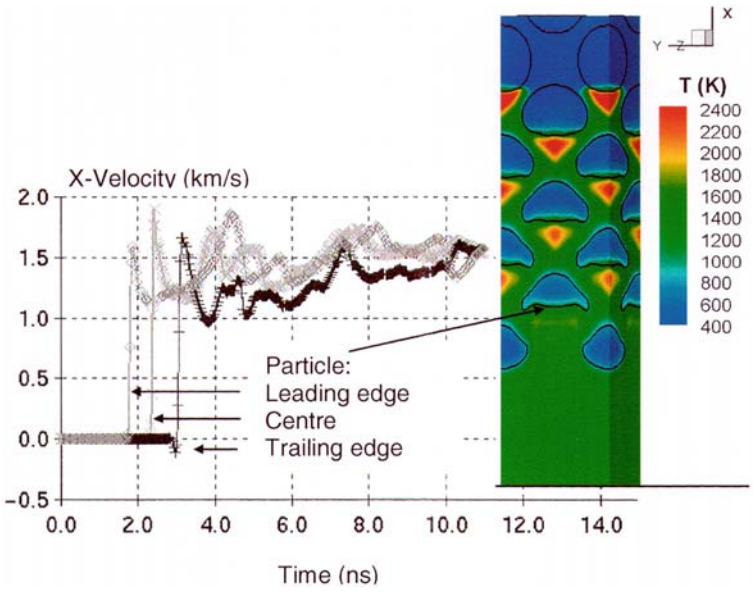

Fig. 2.9. Numerical velocity histories for the leading particle in a $1\,\mathrm{g\,cm^{-3}}$ liquid and aluminum particle system subjected to a 101.3-kbar shock [39,68]

2.3 Transition to Detonation

2.3.1 Progressive DDT

In reactive particle–oxidizing gas mixtures, two types of DDT can be observed: progressive DDT and abrupt DDT via an explosion center. The progressive DDT typically occurs in small tubes, but also for high mass concentrations or large sizes of particles in large tubes.

Figure 2.10 shows a streak photograph registering a progressive DDT process obtained by Strauss [1] in 1968 for a nearly stoichiometric flaked aluminum–oxygen mixture in a 26.4-mm-diameter, 2.7-m-long vertical glass tube. After initiation using a detonator, the flame gradually accelerates towards a spinning detonation without abrupt explosion and a backwards-propagating retonation wave. The final detonation velocity is $1{,}436\,\mathrm{m\,s^{-1}}$ with a 15% deficit relative to the equilibrium CJ value. Figure 2.11 records a progressive DDT observed by Fangrat et al. [5] for highly volatile brown coal dust–oxygen mixtures in a $50\,\mathrm{mm} \times 50\,\mathrm{mm}$ cross section, 3.2-m-long vertical steel tube with a full-length glass window, using 350 J copper wire discharge initiation. While an increase in particle concentration decreases the transition distance, the flame acceleration gradually proceeds towards a detonation without abrupt explosion and retonation. The detonation velocity was recorded to be 1,550, 1,700, and $1{,}900\,\mathrm{m\,s^{-1}}$ for particle concentrations of 0.28, 0.54, and $1.4\,\mathrm{kg\,m^{-3}}$ respectively. Figure 2.12 shows the evolution of pressure histories in a DDT process reported by Peraldi and Veyssiere [8] for a starch–oxygen mixture in a $53\,\mathrm{mm} \times 53\,\mathrm{mm}$ cross section, 4.5-m-long vertical tube using a $2H_2$–O_2 detonation driver as the initiation source. The shock wave is progressively enhanced towards a "quasi-steady" detonation wave with a relatively smooth pressure history behind the shock front without a distinct backwards-

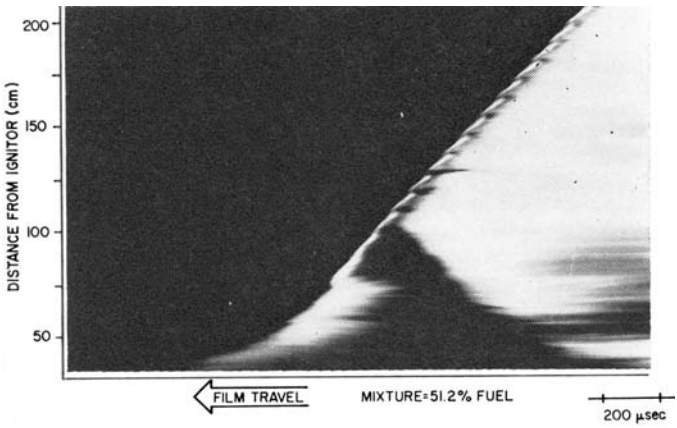

Fig. 2.10. A streak photograph of a progressive deflagration-to-detonation transition (DDT) for a flaked aluminum–oxygen mixture in a 26.4-mm-diameter tube [1]

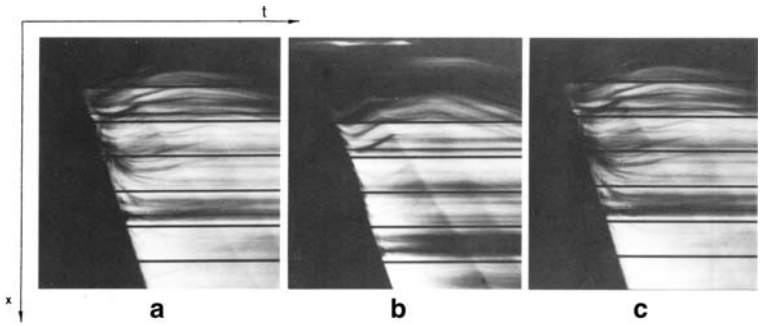

Fig. 2.11. Streak photographs of a progressive DDT for less than 71-μm Egyptian brown coal–oxygen mixtures in a 50 mm × 50 mm cross section tube. **a** $\sigma_p = 0.28\,kg\,m^{-3}$, **b** $\sigma_p = 0.54\,kg\,m^{-3}$, and **c** $\sigma_p = 1.4\,kg\,m^{-3}$ [5]

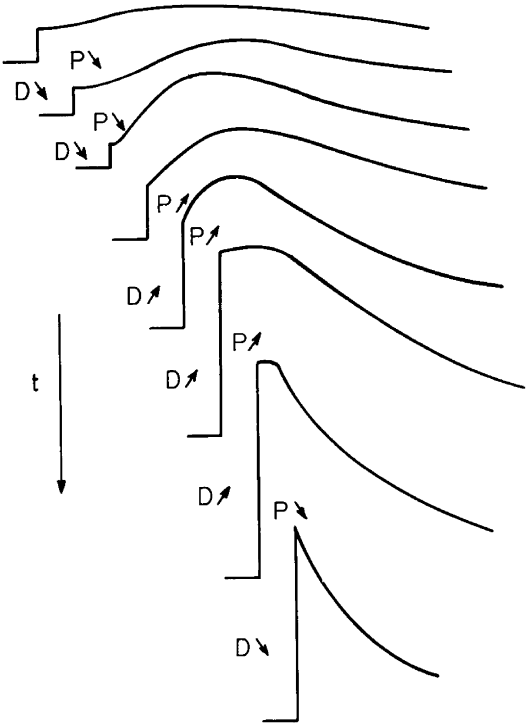

Fig. 2.12. Evolution of pressure history versus propagation distance of an accelerating shock in a $\sigma_p = 1.124\,kg\,m^{-3}$, 20-μm starch–oxygen mixture [8]

propagating retonation shock wave. In a concentration range of 1–3 $kg\,m^{-3}$, the propagation velocity reaches 1,300–1,480 $m\,s^{-1}$ with a deficit relative to the CJ value as large as 30–40%.

Thus, the progressive DDT is characterized by gradual flame acceleration without abrupt onset from an autoexplosion center that forms an overdriven detonation and retonation. The detonation wave developed is often featured with a large deficit of the detonation velocity and a relatively smooth pressure history without a distinguished, periodically oscillating transverse wave structure behind the shock front. The progressive DDT has only been observed in tubes where the tube wall provides confinement of the flame and repeated reflections of the transverse shock waves to progressively amplify the reaction.

2.3.2 Abrupt DDT

For most reactive gases, a detonation wave manifests itself by a transverse wave structure with a detonation cell size of a few millimeters in fuel–oxygen mixtures and a few centimeters in fuel–air mixtures. For reactive solid particles suspended in pure oxygen, however, experiments in tubes of a few centimeters in cross-sectional dimension described earlier found a progressive DDT or very marginal detonation without a distinct transverse wave structure. An abrupt DDT via explosion centers leading to a detonation wave with a transverse wave structure was observed in cornstarch–oxygen mixtures when using a 140-mm diameter, 17.4-m-long tube [70]. Tests using large and sufficiently long tubes are necessary to achieve a DDT in reactive particle–air mixtures.

Using a tube 600 mm in diameter by 42 m in length, Gardner et al. [15] recorded a transition with a violent onset to detonation in a coal dust–air mixture using a $30\,\mathrm{m\,s^{-1}}$ flame jet initiation. As shown in Fig. 2.13, an abrupt DDT takes place near the end of the tube where a peak pressure of 81 atm was measured. The tube, with a length–diameter ratio of 70, was still too short to observe a self-sustained detonation wave.

Complete DDT processes in air via an autoexplosion center were observed for cornstarch and flaked aluminum particles in a 300-mm-diameter, 37-m-long tube (with a tube length–diameter ratio of 123) [20]. The observed DDT process can be divided into a slow-reacting compression stage and a fast-reacting shock stage using relatively weak initiation, as shown in Figs. 2.14–2.16 for mixtures at 1-bar initial pressure. Early in the reacting compression stage, the compression wave is slowly amplified. The compression wave amplification coupled with the chemical energy released by the flame can be clearly recognized through the flame front trajectory crossing the backside of the compression waves. For the lean aluminum–air mixture shown in Fig. 2.15, the reacting compression stage becomes a multiple-compression one, in which the second compression wave is amplified at $50 < x/d < 105$ behind the precursor shock front that was developed from the first compression wave. The multiple-compression stage was also observed in lean cornstarch–oxygen mixtures [70]. As a result of the reacting compression stage, a critical shock wave forms with a Mach number between 3.1 and 3.5 (at $x/d \sim 95$ and 105 in

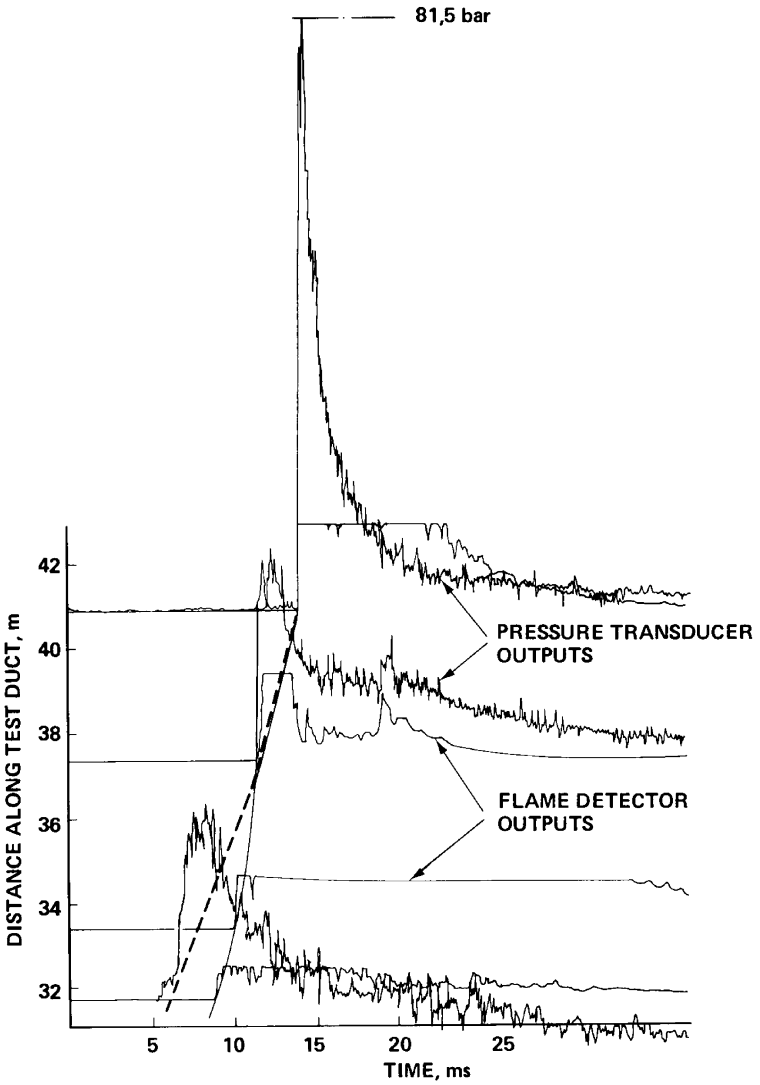

Fig. 2.13. DDT for a $\sigma_{\mathrm{p}} = 0.27\,\mathrm{kg\,m^{-3}}$, less than 75 µm (grade 250) of the US western subbituminous coal–air mixture in a 0.6-m-diameter tube [15]

Figs. 2.14, 2.15 for less sensitive mixtures and at $x/d \sim 35$ in Fig. 2.16 for more sensitive mixtures). Near the formation of the critical shock wave, the flame velocity rapidly increases, indicating that the critical shock wave would be defined not only by a Mach number but also by the temperature gradients behind the shock front. An understanding of the underlying mechanism of detailed turbulent combustion of particles in the reacting compression stage would require further research with advanced diagnostics.

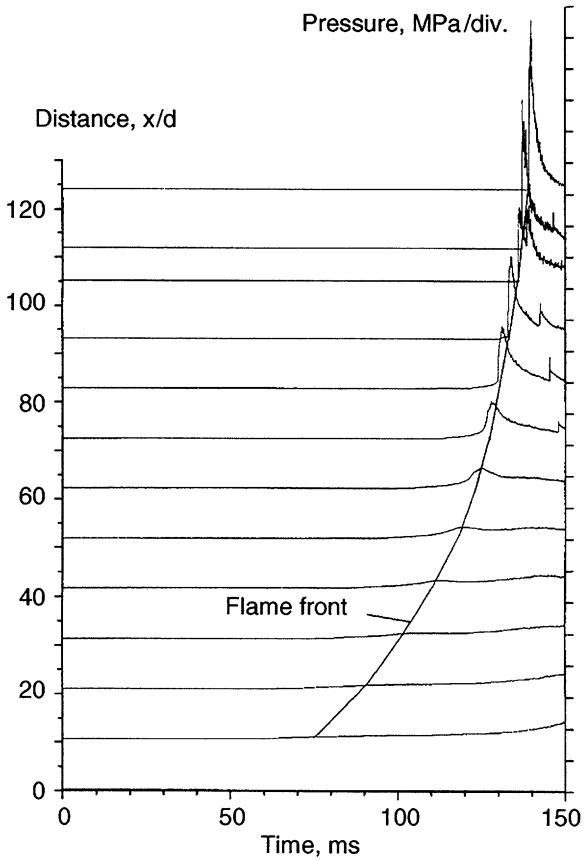

Fig. 2.14. DDT in a 400 g m^{-3}, 10-μm cornstarch–air mixture ($\phi = 1.72$) at 1-bar initial pressure using a 0.3 m inner diameter (ID) tube and four 300-J detonators [20]

The formation of the critical shock marks the beginning of the reacting shock stage in which the flame accelerates rapidly owing to close coupling with the shock amplification, as observed in a homogeneous gas DDT [71, 72]. Within a propagation distance of the reacting shock of about 20 tube diameters in Figs. 2.14 and 2.15 and less than ten tube diameters in Fig. 2.16, an abrupt onset of overdriven detonation takes place and brings the flame velocity to its maximum. Afterwards, the overdriven detonation wave begins to relax towards a self-sustained transverse wave detonation mode. If it is normalized with the characteristic detonation cell size (to be reviewed in Sect. 2.3.3), the propagation distance of the reacting shock, which begins from the formation of the critical shock and ends at the onset of the maximum overdriven detonation, amounts to about six detonation cell sizes for all three mixtures. While the onset of the overdriven detonation for less sensitive mixtures such as cornstarch–air and lean aluminum–air is clearly accompanied by a retonation

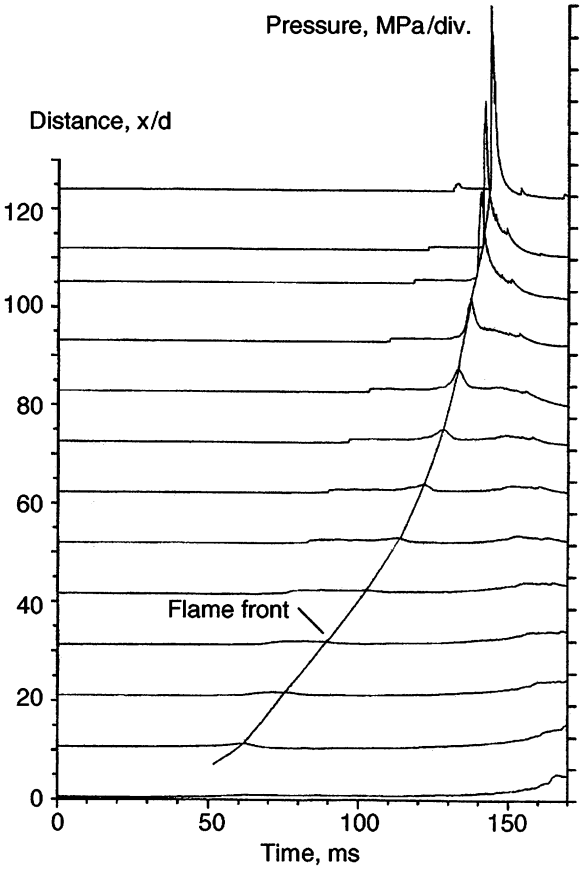

Fig. 2.15. DDT in a 200 g m^{-3}, 36 µm × 36 µm × 1 µm flaked aluminum–air mixture ($\phi = 0.645$) at 1-bar initial pressure using a 0.3-m-ID tube and a 300-J detonator [20]

wave propagating backwards (Figs. 2.14, 2.15), the retonation wave in rich aluminum–air is rather weak as shown in Fig. 2.16.

The self-sustained detonation structure is characterized in the shock wave front and the oscillation frequency recorded in multiple pressure profiles distributed on a tube circumference. Figure 2.17 displays a single-head spinning wave in the 300-mm-diameter tube for the rich cornstarch–air mixture that was used in the DDT experiment shown in Fig. 2.14. The single transverse wave head can be recognized between the profiles numbered 1 and 8. The single-head spinning mode was observed over a wide range of fuel equivalence ratios between 0.7 and 3 at 1-bar initial pressure.

Figure 2.18 shows a detonation wave with multiple transverse wave heads in the 300-mm-diameter tube for the rich flaked aluminum–air mixture with a DDT displayed in Fig. 2.16. Four transverse wave heads can be recognized on one tube circumference at traces 1, 3, 5, and 6. This, together with a

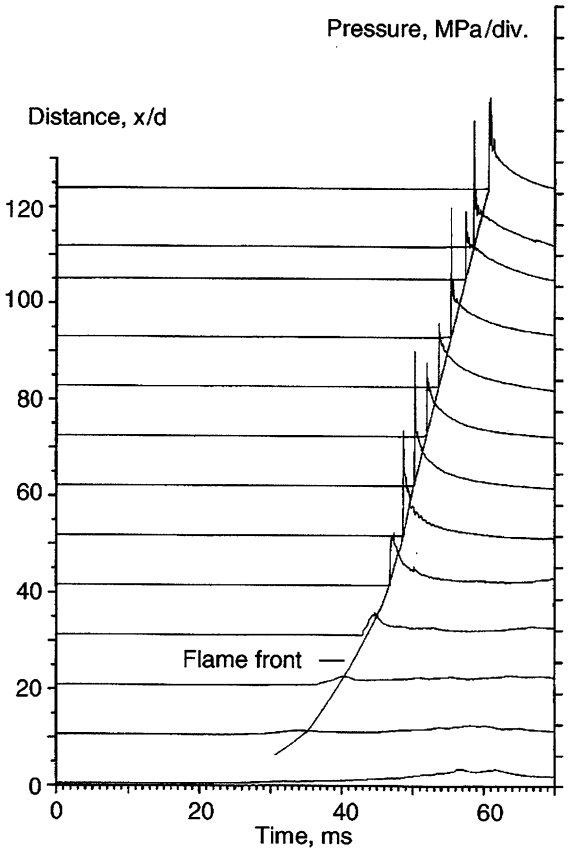

Fig. 2.16. DDT in a $500\,\mathrm{g\,m^{-3}}$, $36\,\mu\mathrm{m} \times 36\,\mu\mathrm{m} \times 1\,\mu\mathrm{m}$ flaked aluminum–air mixture ($\phi = 1.61$) at 1-bar initial pressure using a 0.3-m-ID tube and a 300-J detonator [20]

pressure oscillation period of about $200\,\mu\mathrm{s}$, indicates at least two detonation cells around the tube circumference with a mean cell size of approximately 0.47 m. The pressure oscillation behind the aluminum detonation front appears weaker than that of the single-head spinning cornstarch detonation displayed in Fig. 2.17, likely caused by the high volatile content of cornstarch particles.

The insensitivity of aluminum–air detonation was further shown through the DDT in 0.1-μm atomized aluminum particles, known as "Alex" made by an exploding wire process, suspended in air using an 80-mm diameter, 10-m-long tube (with a tube length–diameter ratio of 125) [73]. At 1-atm initial pressure using a 6-kJ detonator, a multiple-compression DDT process was observed and abrupt transition to a spinning detonation occurred near the end of the tube, where the propagation distance of the reacting shock was again confirmed to be six characteristic detonation cell sizes. As the initial pressure

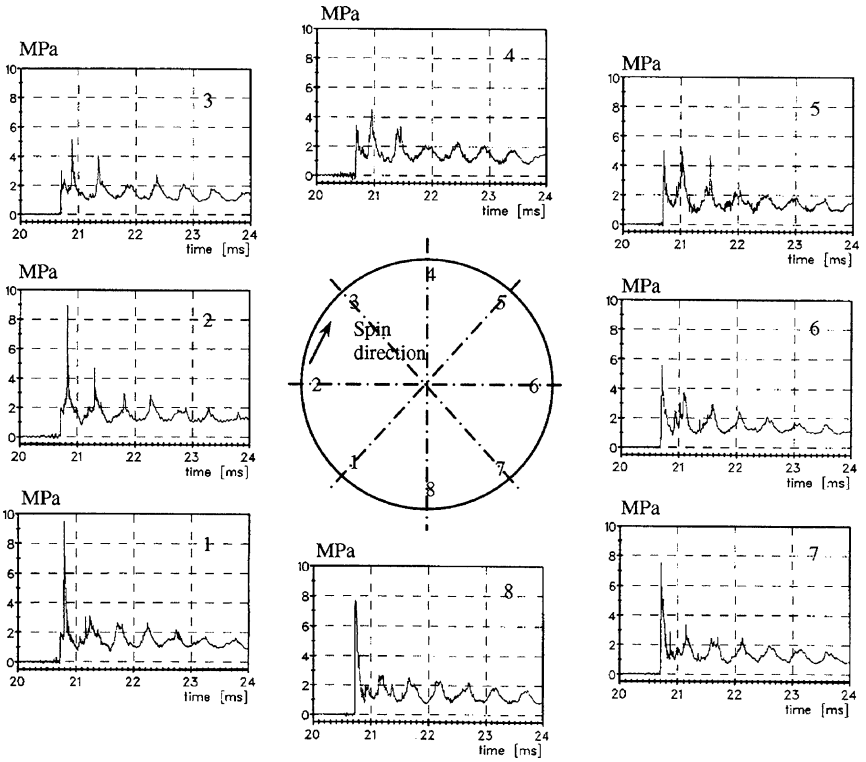

Fig. 2.17. Pressure profiles on a 0.3-m-ID tube circumference in a $400\,\mathrm{g\,m^{-3}}$, 10-μm cornstarch–air mixture ($\phi = 1.72$) at 1-bar initial pressure [20]

increased, the DDT distance was reduced to the half of the tube length and the weak primary pressure oscillation of the established spinning detonation became more distinguished with an increase in amplitude, indicating a stronger transverse wave (Fig. 2.19). A primary oscillation period of 140 μs can be determined in the pressure history at $p_0 = 2.5\,\mathrm{atm}$. When multiplied by the propagation velocity at that location, this oscillation period results in a pitch of 230 mm that is consistent with the smoke foil record. In summary, the strong dependence of detonation sensitivity on initial pressure and the highly nonlinear abrupt DDT nature in the micrometric and nanometric aluminum–air mixtures suggest that the aluminum reaction mechanism of the detonation waves depends on chemical kinetics. However, the weak transverse wave structure of the aluminum–air detonation at 1 atm indicates some weaker functional dependence than the Arrhenius kinetics and is likely associated with some slower diffusional combustion of the part of the aluminum mass at a later time. The insensitivity of aluminum–air detonation might be attributed not only to heterogeneous transport processes but also to a high-melting-point oxide layer that passivates the surface of each particle.

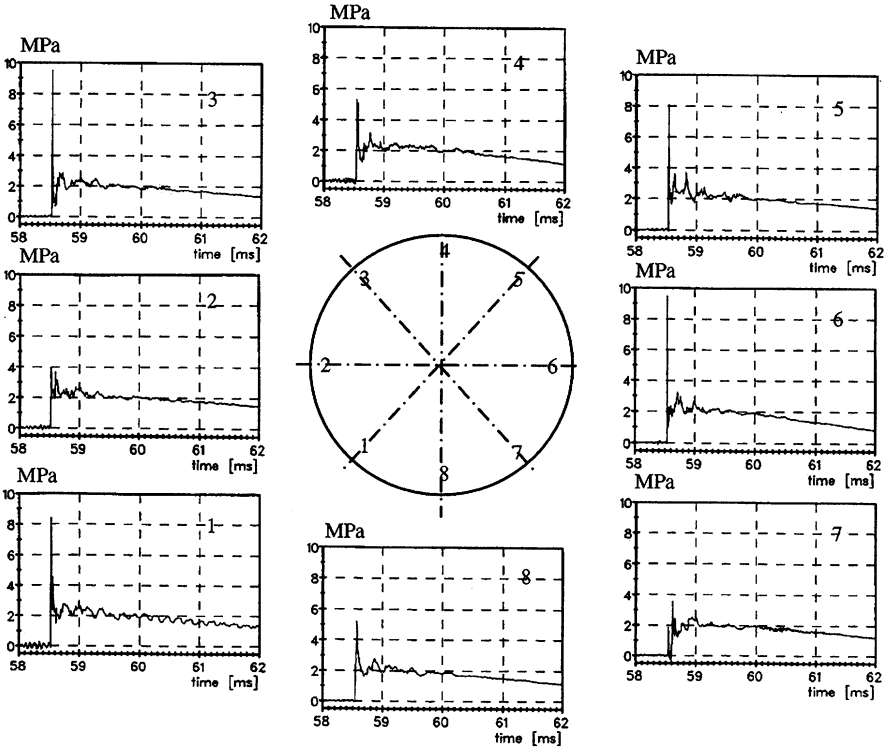

Fig. 2.18. Pressure profiles on a 0.3-m-ID tube circumference in a $500\,\mathrm{g\,m^{-3}}$, $36\,\mu\mathrm{m} \times 36\,\mu\mathrm{m} \times 1\,\mu\mathrm{m}$ flaked aluminum–air mixture ($\phi = 1.61$) at 1-bar initial pressure [20]

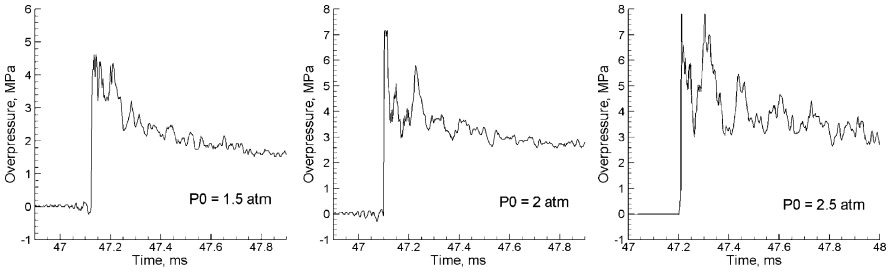

Fig. 2.19. Detonation pressure history in an 80-mm-ID tube at 8.72 m in a 0.1-μm aluminum–air mixture with particle concentrations of 600, 800, and $1{,}000\,\mathrm{g\,m^{-3}}$ at 1.5, 2, and 2.5 atm, respectively (normalized to be $400\,\mathrm{g\,m^{-3}}$ per atmosphere)

The single-head spinning detonation has been accepted as the lowest stable, self-sustained detonation mode in a tube for homogenous gas mixtures. The corresponding tube diameter is therefore referred to as the "minimum

tube diameter" $d_{\min}$, a necessary boundary condition for the transition to and propagation of a stable detonation [77]. The minimum tube diameter for detonation in solid particle–gas flow is at least 1 order of magnitude greater than the minimum tube diameter observed for most detonable gas mixtures.

2.3.3 Transition to Detonation Near the End Wall

Considering a deflagration wave propagating in a tube, the flame Mach number does not reach its critical value when the precursor shock impacts the end wall. In this case, Craven and Greig [74] suggested a DDT scenario with the onset of detonation on the reflected shock region between the flame front and the end wall. The resultant detonation then propagates into the reflected shock region and reflects on the end wall, thus resulting in a very high peak pressure. Such a DDT may interpret an earlier experimental observation of Kogako [75], in which the high pressure in a 6.8% acetylene–air mixture caused destruction of the end section of a steel tube (305 mm in diameter and 10 mm in wall thickness), with heavy fragments flying out in all directions. A Hugoniot analysis indicates that for a flame Mach number of 2.5 observed before the rupture, the peak pressure generated by the reflected detonation on the reflected shock state achieves a value 10 times that of the reflected CJ detonation in the initial mixture where $p_0 = 1$ atm [25].

The pressure generated in the Graven–Greig DDT can be further increased if a dense reactive particle suspension is introduced in a reactive gas mixture in the front of the end wall. The reflected peak pressure behind a dense particle suspension layer on the end wall is considerably higher than that for gas normal reflection on a rigid wall as predicted in Fig. 2.20, owing to wave reflections and focusing acting on the voids in the particle system. As the

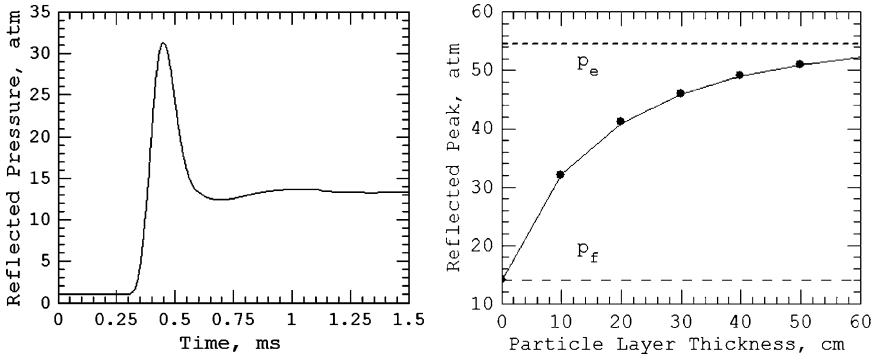

Fig. 2.20. Computed wall-reflected pressure for an inert shock (M = 1.9, $\gamma = 1.29$, and $a_g = 345\,\mathrm{m\,s^{-1}}$) running in a $10\,\mathrm{kg\,m^{-3}}$, 5-μm aluminum particle suspension layer in front of the wall. *Left*: Pressure history for the 100-mm layer thickness. *Right*: Peak pressure versus layer thickness. p_e phase-equilibrium Hugoniot pressure, p_f gaseous Hugoniot pressure [25]

particle layer thickness increases, the wall-reflected peak pressure increases towards the phase equilibrium Hugoniot value for the given particle concentration. One can expect that the DDT on the reflected shock region in a dense reactive particle–reactive gas suspension near a wall can generate a very significant pressure. Such a hybrid DDT was observed in an 80-mm-diameter tube filled with a lean acetylene–air mixture and a dense aluminum particle suspension layer ($\sigma_p = 10\,\mathrm{kg\,m^{-3}}$, 100 mm thick) located in the front of the tube end wall [25]. A DDT occurred after the wall reflection of the precursor shock and the reflected detonation produced a wall peak pressure of 700 atm (Fig. 2.21). In comparison, the DDT after the wall reflection for the same gas system without particles achieved a wall peak pressure between 260 and 300 atm. Thus, addition of a dense aluminum particle layer provides a pressure enhancement factor of more than 2. The enhancement effect results from both the higher reflected gas pressures due to multiple shock interactions with dense particles and the particle combustion.

2.3.4 Initiation of Unconfined Detonation

Very few experimental studies have been published for initiation of unconfined particle-gas detonation without the influence of tube confinement. Tulis [76] attempted to detonate 4.54 kg flaked aluminum explosively dispersed in air in a 1-m-high, 3-m-radius cylindrical cloud. The cloud was initiated near the center using 2.27 kg solid explosive; detonation was not observed and the ground pressure decayed from 1.8 to 0.9 MPa in a radius from 1.3 to 2.7 m. Veyssiere et al. [21] detonated a rich flaked aluminum–oxygen cloud (with an equivalence ratio larger than 1.6) in a vertical cylindrical polyethylene bag, 1 m high and 0.7 m in diameter, initiated at the top using 150 g TNT. The detonation observed near the bottom of the bag reached a velocity of $1{,}650\,\mathrm{m\,s^{-1}}$ and a peak pressure of 3.6–5.2 MPa. For the same arrangement, only a decaying blast wave was observed, followed by particle combustion for 20-μm starch and atomized aluminum particles.

To observe the propagation of detonation, a large-scale cloud was generated through a charge configuration arranged in an 18-m-long, 90° V-shaped steel trough line, in which a pentaerythritol tetranitrate cord ($21.3\,\mathrm{g\,m^{-1}}$, 6.1 mm in diameter) was located at the bottom vertex covered by a layer of aluminum powder [22]. Detonation of the pentaerythritol tetranitrate cord dispersed the aluminum powder in air to a 3-m-radius cross section and an 18-m-long suspension at a given dispersal time. The aluminum–air cloud was then initiated at one end using 8 kg C4 explosive located 1.5 m from the end as well as 1 m from the ground and the steel line. Figure 2.22 shows an example of high-speed photographs for a DDT in a 31.5 kg flaked aluminum–air cloud with an average particle concentration of $250\,\mathrm{g\,m^{-3}}$ (or an equivalence ratio of 0.9 based on the local air pressure of 91 kPa). From the ground pressure histories along the propagation distance shown in Fig. 2.23, the shock front velocity is $1{,}600\,\mathrm{m\,s^{-1}}$ at 4 m from the C4 location and decays to $1{,}380\,\mathrm{m\,s^{-1}}$

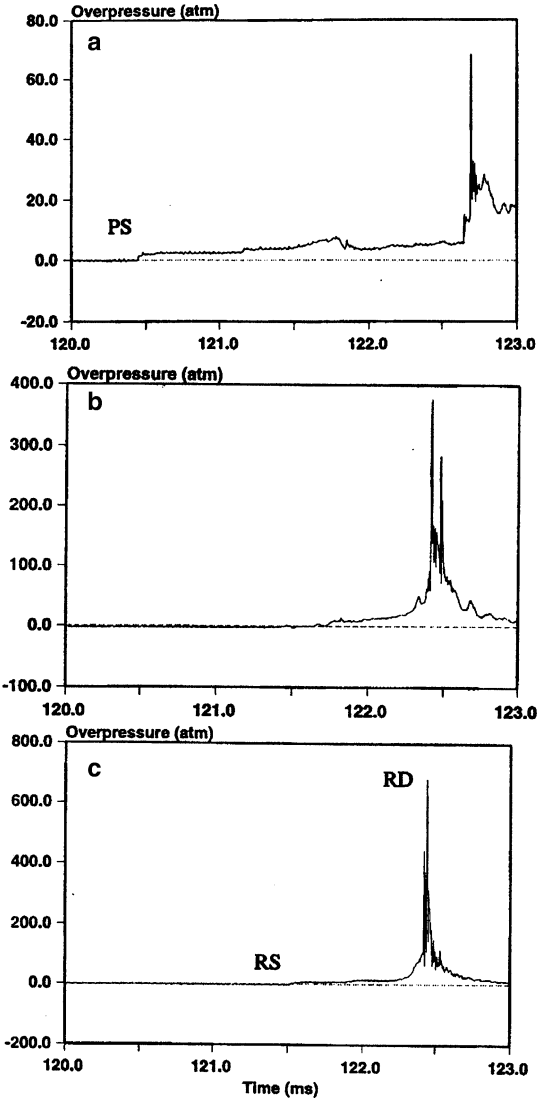

Fig. 2.21. Pressure histories for the DDT in a 6.75% C_2H_2–air mixture at 1-atm initial pressure with a 100-mm layer of 10 kg m^{-3}, 5-μm aluminum particles in front of the end wall of an 80-mm-ID tube: **a** 580 mm from the end wall; **b** 35 mm from the end wall; **c** at the end wall. *PS* precursor shock, *RS* reflected shock, *RD* reflected detonation [25]

at 7 m. At 11 m, the abrupt onset of detonation occurs with a peak pressure of 8.4 MPa. The 2-m-averaged detonation velocity reaches a maximum value of 1,533 m s^{-1} and remains at 1,460–1500 m s^{-1} in the further propagation. In the oscillating pressure history after 11 m, a transverse wave structure is distinguishable with a primary period of about 350–400 μs for the signal at

Fig. 2.22. DDT in an unconfined 3 m × 3 m × 18 m flaked aluminum–air cloud. *Top left*: Aluminum suspension. *Top right*: 8 kg C4 explosive initiation. *Bottom left* and *bottom right*: Detonation propagation [22]

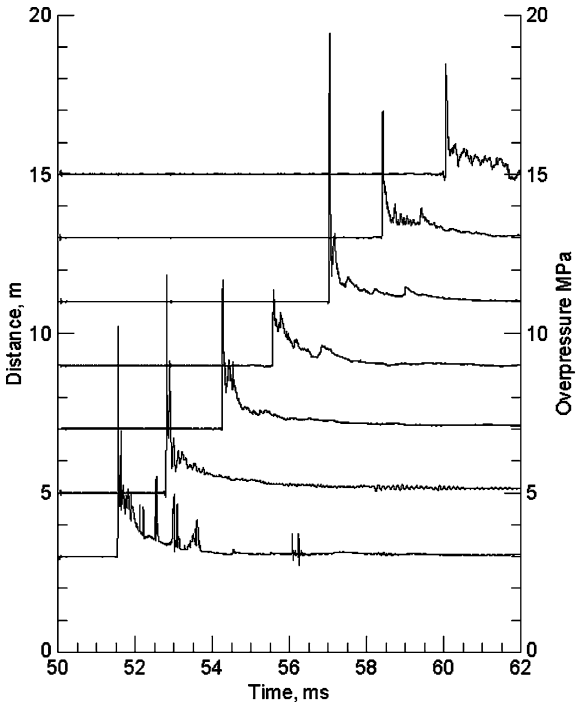

Fig. 2.23. DDT pressures in an unconfined 3 m × 3 m × 18 m flaked aluminum–air cloud using 8 kg C4 explosive initiation [22]

15 m. The smoke foil located at the ground between 13 and 15 m registers a detonation cell width of 0.52–0.6 m, consistent with the pressure oscillation period. This experiment indicates that the 8 kg C4 is near the critical charge for direct initiation of flaked aluminum–air detonation. Replacing the flaked aluminum by 47.6 kg atomized aluminum with a mean diameter of 1.6 μm by number and a mean diameter of 3.3 μm by weight (known as H-2 by Valimet),

abrupt DDT phenomena took place at 13 m with a 5.5-MPa peak pressure. However, in this case the cloud length is too short to observe a self-sustained detonation wave. A DDT was not observed when using 5 kg C4 initiation charge for H-2 aluminum particles. Note that without aluminum particles, the air blast overpressure from the 8 kg C4 explosion decays rapidly to 0.186, 0.046, and 0.023 MPa at 5, 10, and 15 m, respectively.

2.3.5 Detonation Velocity and Pressure

For the solid particle–air detonation waves with spinning structures or transverse wave structures, some experimental detonation velocities are summarized in Figs. 2.24–2.27. These experimental velocities are in agreement with the values computed from the equilibrium CJ theory within about 10% deviation (the low velocity values in Figs. 2.26, 2.27 will be discussed in Sect. 2.5). The 0.1-μm Alex aluminum particles were passivated with an oxide coating to a mass fraction of about 10%, and so its detonation performance was expected to be less energetic than that of the pure aluminum used in the calculation. Agreement with equilibrium CJ theory indicates that the transverse-wave-structured detonation velocity is mainly determined by the energetics. The CJ detonation velocities display a shift towards the lean side and the reasons are twofold: (1) a shift in postshock equivalence ratio from the initial towards a leaner value owing to a particle velocity relaxation time lag and (2) a shift in real particle concentration owing to sedimentation and adhesion of particles to the tube wall during experimental dispersal. As the mixtures become richer in cornstarch and aluminum, the calculated CJ velocity drops; however, the experimental results show a slight decrease or a

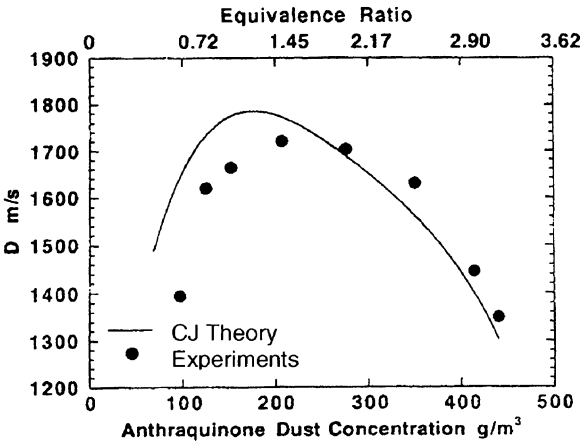

Fig. 2.24. Experimental detonation velocities in 22 μm × 6 μm × 6 μm anthraquinone particle–air mixtures at 1.15-bar initial pressure in a 0.14-m-ID tube and the equilibrium CJ calculations [18]

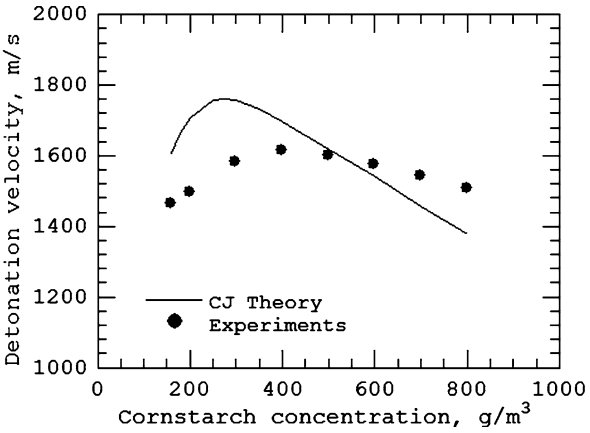

Fig. 2.25. Experimental detonation velocities in 10-µm cornstarch–air mixtures at 1-bar initial pressure in a 0.3-m-ID tube and the equilibrium CJ calculations. The stoichiometric concentration is $233\,\mathrm{g\,m^{-3}}$ [20]

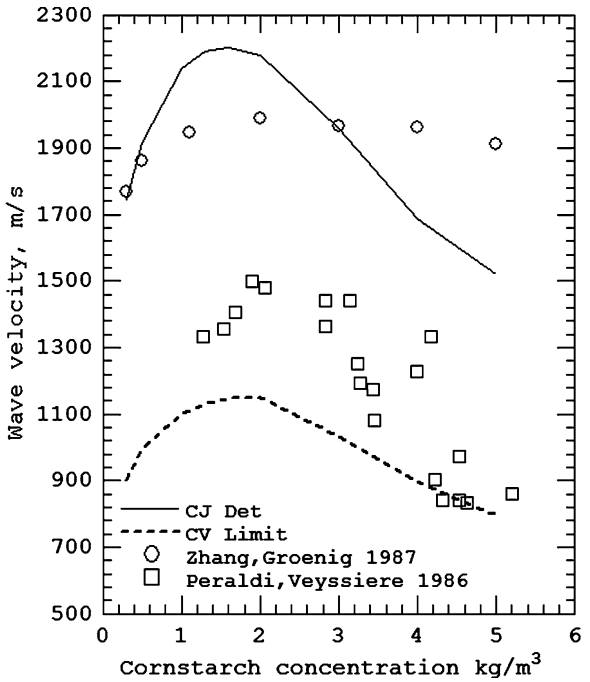

Fig. 2.26. Detonation and quasi-detonation velocities in cornstarch–oxygen mixtures at 1 bar initial pressure. (Data from Zhang and Grönig [16] used a 0.14-m-ID tube and data from Peraldi and Veyssiere [8] used a 53 mm × 53 mm tube)

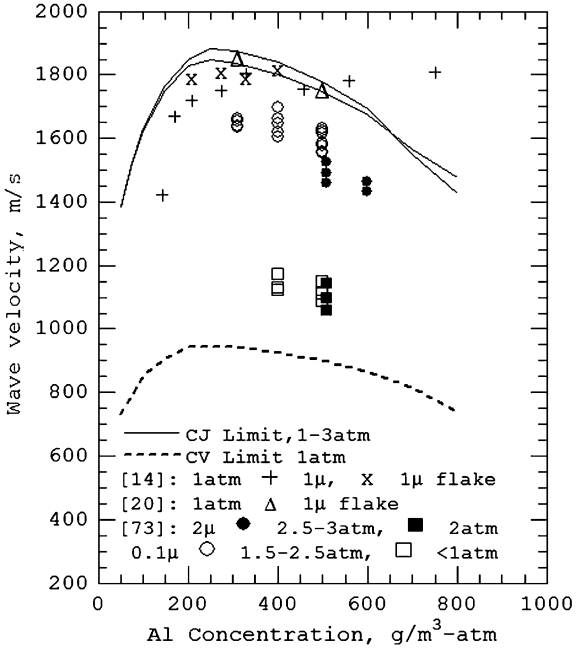

Fig. 2.27. Detonation and quasi-detonation velocities in aluminum–air mixtures. The stoichiometric particle concentration is $310\,\mathrm{g\,m^{-3}}$. (Data from Borisov et al. [14] used a 0.12-m-ID tube, data from Zhang et al. [20] used a 0.3-m-ID tube, and data from Zhang et al. [73] used an 80-mm-ID tube)

"plateau" extending from the peak values. It is probably due to the time lag of momentum and heat transfer from gaseous products to unburned particles and their agglomerates in the hot products. Hence, the equilibrium CJ theory may not be applicable to very rich concentrations of finite-sized particles.

Apart from particle sedimentation and adhesion, which cause experimental difficulties in achieving a uniformly dispersed two-phase mixture as assumed in the equilibrium CJ theory, there are two inherent reasons responsible for detonation velocity deviations, as discussed in Sect. 2.2. First, contrary to the fundamental postulate of the equilibrium CJ theory, detonations in reactive particle–gas mixtures are essentially nonideal, where momentum, heat, and chemical equilibrium between the two phases may not be achieved at the phase-frozen or gaseous sonic locus owing to the finite sizes of particles. Second, momentum and heat loss induced by lateral boundary layer effects behind the shock front increases with larger reaction zones corresponding to an increase in transverse wave spacing.

Experimental determination of the CJ detonation pressure is more difficult than that of the detonation velocity in relatively insensitive particle–gas mixtures, since the large transverse wave spacing of the detonation front provides

various pressures along the three-dimensional shock front and a number of oscillations in the pressure profiles behind the shock front (Figs. 2.17, 2.18). The detonation peak pressures are invariably higher than the equilibrium CJ values by a factor of 2 or more. Rather than attempting to interpret the CJ pressure from an oscillatory pressure record, one can average the experimental "peaks" and "valleys" over a period behind the front, and the resultant median was comparable to the CJ pressures [18].

2.4 Detonation Structure

2.4.1 Spinning and Cellular Detonation

For homogeneous gases, the single-head spinning and cellular detonation waves have been considered as the stable transverse wave detonation modes with a triple-point configuration as the basic feature [77–89]. Owing to detonation insensitivity and high detonation pressures as well as in situ particle dispersal, it has been difficult to register a detonation structure in reactive particles suspended in oxygen or air. There are, however, a few experimental studies available for single-head spinning and cellular detonation waves [16–20].

Figure 2.28 displays a single-head spinning structure at the detonation front around the 140-mm-diameter tube on the circumference in a 0.5-bar stoichiometric cornstarch–oxygen mixture. This structure was observed through the use of a large number of pressure-ion double front gauges distributed on the tube circumference at several axial cross sections within a pitch distance [16]. The corresponding pressure profiles distributed on one circumference are similar to those in Fig. 2.17. In Fig. 2.28, the frontal structure manifests itself primarily in a transverse shock wave that propagates into the induction zone behind the incident shock and produces a traveling triple-point configuration at the front. The transverse wave velocity observed on the periphery is approximately equal to the axial propagation velocity, thus resulting in a spinning track angle, $\alpha = 45°$, at the front around the tube wall.

A two-head spinning or a single-cell detonation wave was also recorded in the 140-mm-diameter tube with the same diagnostic method for a rich cornstarch–oxygen mixture (Fig. 2.29) [17]. The collision of two triple points leads to an overdriven wave followed by a transient decoupling between the shock and chemical reaction. Since the two triple-point configurations move in opposite directions on the circumference, successive collisions make the continual reignition to sustain the detonation wave possible. The triple-point trajectories form a single cell with a cell width of $\lambda \sim \pi d$. The experiments produced a transverse wave velocity of $C \approx 0.62D$ and a mean track angle of $\alpha = \tan^{-1}(C/D) \approx 32°$, where D is the mean axial propagation velocity. The single-head and the two-head detonation wave cannot exist without boundary confinement.

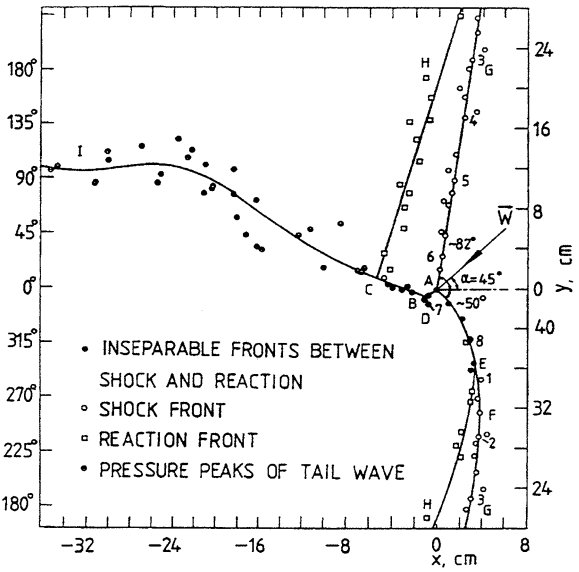

Fig. 2.28. Spinning detonation front structure on a 0.14-m-ID tube circumference in a $554\,\mathrm{g\,m^{-3}}$, 10-μm cornstarch–oxygen mixture ($\phi = 1$) at 0.5-bar initial pressure. x axial coordinate, y circumferential coordinate [16]

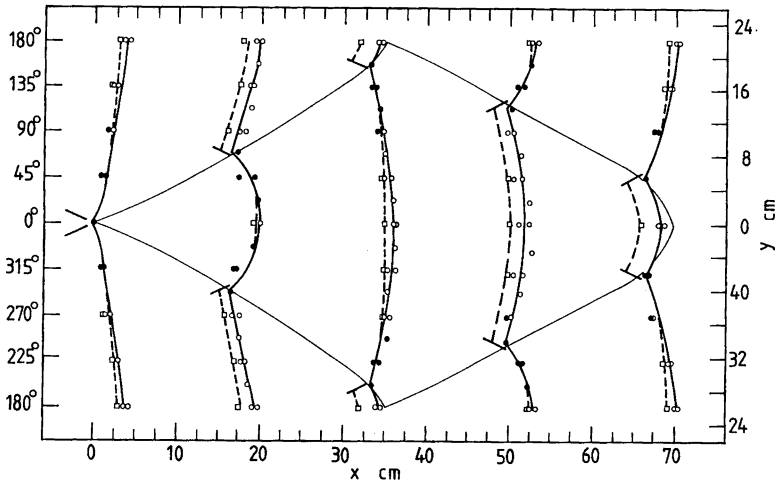

Fig. 2.29. Two-head detonation front structure on a 0.14-m-ID tube circumference in a 10-μm cornstarch–oxygen mixture ($\phi = 3.1$) at 1.15-bar initial pressure. x axial coordinate, y circumferential coordinate. *Open circles* shock front, *squares* flame front, *filled circles* irresolvable between shock and flame front [17]

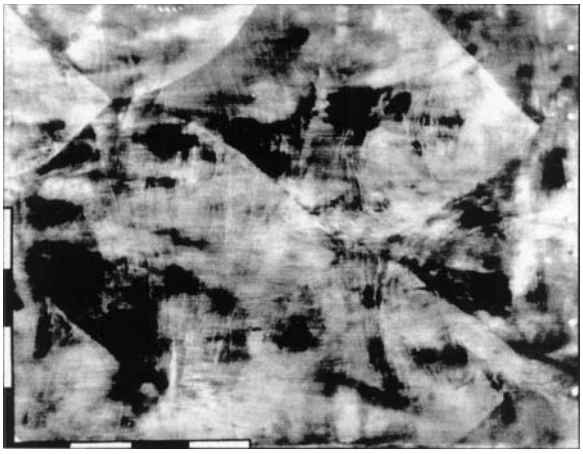

Fig. 2.30. Cellular detonation structure from a smoke foil record on a 0.3 m-ID tube circumference in a 440 g m^{-3}, 10-μm cornstarch–oxygen mixture ($\phi = 0.8$) at 0.5-bar initial pressure. The *scale bar* is 0.1 m and detonation propagates from left to right [20]

Figure 2.30 shows smoke foil records of a cellular detonation structure observed from two experiments in the 300-mm-diameter tube for a $\phi = 0.8$ cornstarch–oxygen mixture at 0.5-bar initial pressure [20]. The soot photographs display more than 1.5 cells in the 0.8-m-wide foil. The average cell width and length measured from the soot photographs are $\lambda = 0.50$ m and $L = 0.77$ m. This results in a mean track angle of the triple-point trajectory of $\alpha = \tan^{-1}(\lambda/L) \approx 33^\circ$ and an average transverse wave velocity of $C = (\tan \alpha)D \approx 0.65D$.

2.4.2 Detonation Dynamic Parameters

In the theory of gas detonation, the correlation by Zeldovich et al. [90] links the minimum tube diameter, $d_{\min}$, for propagation of a stable, self-sustained detonation wave to the cell width of the cellular detonation by

$$d_{\min} \approx \lambda/\pi. \tag{2.9}$$

This defines a characteristic cell size λ for the single-head spinning detonation since it has been considered to be the lowest stable, self-sustained detonation mode [77]. Numerous gas detonation experiments have proven that relation (2.9) is appropriate for fuel–air detonation, but it may underpredict the minimum tube diameter for fuel–oxygen mixtures [123, 124]. For the cornstarch–oxygen mixtures as reviewed in Sect. 2.4.1, the measured cell size, $\lambda = 0.50$ m at the equivalence ratio $\phi = 0.8$ (Fig. 2.30), is consistent with the characteristic cell size of the single-head spinning mode, $\lambda \sim \pi d = 0.44$ m at $\phi = 1$

Table 2.1. Dynamic parameters for detonation of solid particles in oxygen or air

Material	Equivalence ratio	One-head spin tube diameter $d_{\min}$ (m)	Detonation cell size λ (m)	Direct initiation energy E_{cr} (MJ)	Direct initiation charge M_{cr} (kg TNT)	References
10-μm cornstarch–air	1.7	0.3	0.94	293	63	[20]
10-μm cornstarch–O_2	1	0.14	0.44	60	12.8	[16]
Anthraquinone–air (6-μm strips)	1.5	0.14 at 1.16 atm	0.5	40	8.5	[95]
0.1-μm Al–air	1.6	0.08	0.25	4.8	1.0	[73]
Flaked 1-μm Al–air	1.3–1.6	0.12–0.14	0.38–0.44	24–36	5.1–7.7	[14, 20]
Flaked Al–air	0.9	Unconfined	0.55	44	8	[22]
2-μm Al–air	1.3	Unconfined	0.6	62	13	[22]
2 μm Al–air	1.6	0.08 at 2.5 atm	0.62	74	15.8	[73]
Flaked Al–O_2	1–1.6	0.0264	0.08–0.1	0.27–0.8	0.06–0.17	[1, 21]
US W. subbituminous <75μm coal–air	≥1	0.6	1.2–1.8	470–1,500	100–300	[15]
Egyptian brown <75-μm coal–O_2	≥1	0.08	0.25	7.1	1.5	[94]

The initial pressure is 1 atm if not specified. The direct initiation charge is converted on the basis of a TNT detonation energy of 4.67 kJ g^{-1} from the Cheetah equilibrium calculation [130].

(Fig. 2.28). While more experiments are required to draw a firm conclusion, this consistency suggests that relation (2.9) is applicable to the heterogeneous detonation of reactive particles in air and oxygen. This could be attributed to the fact that detonation in reactive particle–gas flow possesses a large transverse wave spacing imbedded with numerous distributed hot or flame spots induced by the particles. Therefore, the detonation is relatively insensitive to small disturbances in the boundary layer on the wall of large tubes. Relation (2.9) has been applied to the single-head spinning detonation waves to evaluate characteristic cell sizes for various mixtures. The resulting characteristic cell sizes for several types of reactive particles suspended in air or oxygen at various equivalence ratios are listed in Table 2.1. The evaluated cell sizes for the particle–air detonation waves range typically between 0.25 and 1 m at 1-atm initial pressure, thus being at least 1 order of magnitude larger than that for the detonation in most gas–air mixtures.

The long DDT distances shown in Figs. 2.14–2.15 were obtained using pyrotechnical igniters with an initiation energy of 1.2 kJ for cornstarch–air and 0.3 kJ for flaked aluminum–air. Hence, an initiation energy of 10^2–10^3 J can be considered a "weak" initiation for a reactive particle–air DDT that starts from slow deflagration during the initial stage. This fact indicates that the initiation energy for the reactive particle–air DDT is at least 3 orders of magnitude greater than that for the gaseous DDT using weak initiation.

Alternatively, as indicated in Sect. 2.3.4, direct initiation of an unconfined flaked aluminum–air detonation requires a critical charge near 8 kg, 3 orders of magnitude greater than the critical charge for direct initiation of a gaseous fuel–air detonation that can be found in [91]. The requirement of a 3 orders of magnitude higher initiation energy was also found when comparing dust explosions to gas explosions in closed vessels [4]. Considering the 1 order of magnitude larger cell size in the particle–gas detonations compared with gas detonations, one can reasonably scale the initiation energy to the cube of the characteristic detonation cell size for reactive particle–oxidizing gas mixtures, a power scaling rule well demonstrated for gaseous detonations [90–93]. Because of the lack of direct experimental data, the correlation of the critical energy, E_{cr}, for direct initiation of gaseous detonation [92]

$$E_{\mathrm{cr}} = A\rho_0 D^2 \lambda^3 \tag{2.10}$$

has been assumed to estimate the critical energy and critical charge mass for direct initiation of unconfined reactive particle–oxidizing gas detonation. Here, the values of ρ_0, D, and λ are taken from the initial mixture density, the experimental detonation velocity and the characteristic cell size, respectively. The coefficient $A = 82$ is a fitting to the initiation charge mass (8 kg C4 with a TNT mass equivalency of 1.19) for the unconfined flaked aluminum–air detonation experiment shown in Fig. 2.23. The estimates of the critical energy and charge mass obtained are listed in Table 2.1. As for a range of aluminum particle sizes, the critical initiation energy and charge mass obtained typically range between 20 and 200 MJ and 5 and 50 kg, respectively, for unconfined aluminum particle–air detonation at 1-atm initial pressure. This estimate only serves as a reference; the accurate values must be obtained from direct measurements performed in large-scale experiments, which are current subjects of research. For a number of experiments in tubes, a hydrogen–oxygen or acetylene–oxygen detonation driver was also often used to initiate the reactive particle–gas detonation directly. A method to evaluate the initiation energy for a detonation driver can be found in [70].

For organic particles with a high volatile content, detonation sensitivity is increased with increasing initial pressure p_0. In the same cornstarch–air mixtures, while the single-head spinning detonation was found in the 300-mm-diameter tube, it was observed in the 140-mm-diameter tube only when the initial pressure was raised to between 2 and 2.5 bar [70]. These results suggest that the high volatile organic particle–gas detonation approximately follows the scaling rule of gaseous detonation, in which the detonation cell size is inversely proportional to the initial pressure [96–98]:

$$\lambda \sim p_0^{-m}, \quad m = O(1). \tag{2.11}$$

Correlation (2.11), together with relation (2.9), links the minimum tube diameter d_{min} with the detonation cell size λ at an initial pressure p_0. The approximately inverse dependency of λ on p_0 arises from the approximate linear dependency of p_0 on the oxygen concentration above a certain lower initial

pressure limit. Hence, $m = O(1)$ indicates a reaction mechanism strongly dependent on the gas-phase kinetics for these organic particle–gas detonation waves.

Aluminum particles possess a high-melting-point oxide coating that must be melted or cracked open before aluminum can react. Because sound knowledge of the aluminum reaction mechanism under detonation conditions is lacking, the droplet diffusion combustion theory has been applied to aluminum particles–gas detonation problems in the literature [14, 27, 66]. The diffusion theory states that the particle burning time is proportional to a power of its initial diameter, $t_\mathrm{b} \sim d_{\mathrm{p}0}^n$ $(n = 2)$, as the temperature of a particle exceeds the oxide melting point [99]. The theory assumes infinite kinetics and is essentially independent of temperature and pressure. It applies according to the classic experimental observations for combustion of large aluminum particles in quiescent atmospheres [100]. Under conditions of 1–100 atm and 1–50-μm particles, however, it has been found that the burning rate of aluminum particles is greater and increases with the initial pressure, thus resulting in a smaller power n between 1 and 2 and a dependence on pressure [101–108]. The power $n < 2$ implies the contribution of finite gas-phase kinetics and possibly convective flow effects [99]. Since the burning aluminum mass flux in the particle radial direction is inversely proportional to the particle radius (yielding $t_\mathrm{b} \sim d_{\mathrm{p}0}^2$) in the diffusional transport and is independent of the particle radius (yielding $t_\mathrm{b} \sim d_{\mathrm{p}0}$) in the kinetic process, the diffusional transport rates approach infinity as the particle diameter approaches zero, while the kinetic process rates do not increase with decreasing particle size. Therefore, at sufficiently small particle diameters, the use of the d^2 law becomes incorrect and the particle combustion must become kinetics-dependent.

The high-momentum flow immediately behind the shock, moreover, also changes the physical properties of particles and consequently influences the ignition and reaction of particles [109–114]. In quiescent or low-speed flow, a threshold ignition temperature was observed to be above 2,100 K for 2–30-μm atomized aluminum particles at 6–11 bar, with a measured ignition delay time proportional to a power of the particle diameter, $t_\mathrm{I} \sim d_{\mathrm{p}0}^2$, following the convective heat law [115]. In shock tube experiments, however, Borisov et al. [109] reported a drop of the ignition temperature to about 1,400 K for 15–20-μm aluminum particles after a reflected shock. The shock ignition temperature would be expected to be even lower for 1–2-μm particles. A temperature of 1,000–1,400 K results in a vapor pressure of 10^{-5}–10^{-1} Pa only, thus further indicating the improbability of diffusion-limited evaporation reaction in shocked conditions. Experiments were also conducted to ignite aluminum particles by a shock wave immediately followed with a detonation products expansion flow, using a hydrogen–oxygen detonation driver connected with an air-filled driven section in which particles were initially dispersed at the end of the driver section [114]. The observed ignition delay time tended towards $t_\mathrm{I} \sim d_{\mathrm{p}0}$ for a wide aluminum particle diameter range of 2–110 μm, further suggesting possible influences of the kinetics-limited ignition.

Since aluminum–air detonation only occurs for a particle characteristic size less than a few micrometers and the particles ignite and burn under the shocked (above $40p_0$ and 1,500–2,000 K) and subsequent detonation (above $20p_0$ and 3,000–4,000 K) conditions, one would expect that finite kinetics could affect the aluminum ignition and reaction. Chemical kinetics dependence was evidenced by the abrupt aluminum–air DDT in both tubes and an unconfined atmosphere as described in Sects. 2.3.2 and 2.3.4. Experiments also showed that an increase in initial pressure significantly reduces the DDT distance for 0.1-μm aluminum particle–air mixtures in an 80-mm-diameter tube [73]. Through an increase of the aluminum particle size to about 2 μm (known as H-2 by Valimet), a transition to single-head spinning detonation was observed only when the initial pressure was increased to 2.5 atm, while at 2 atm and below no transition to detonation occurred within the tube length, as displayed in Fig. 2.31.

If the above discussions are taken into account, correlations for the ignition delay and burning time of fine aluminum particles can be proposed as $t_\mathrm{I} \sim d_{p_0}^n/p_0^m$ and $t_\mathrm{b} \sim d_{p_0}^{n'}/p_0^{m'}$, where $n, n' \leqslant 2$, $m, m' \leqslant 1$ under detonation conditions. Assuming that the minimum tube diameter for aluminum particle–gas detonation d_min or the detonation cell size λ is proportional to the particle reaction times t_I and t_b, one obtains

$$\pi\, d_\mathrm{min} \sim \lambda \sim d_{p_0}^n \,/\, p_0^m \quad \text{with } n \leqslant 2,\ m \leqslant 1. \tag{2.12}$$

Relation (2.12) is an analogy to that of gaseous detonation where the detonation cell size is scaled to the induction time assuming that the induction time

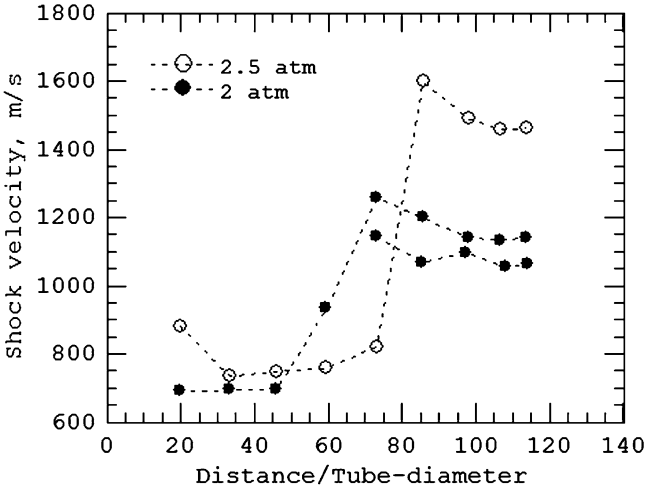

Fig. 2.31. Transition from deflagration to quasi-detonation at 2-atm initial pressure and to detonation at 2.5 atm in 500 g m^{-3} per atmosphere, 2-μm (H-2) aluminum–air mixtures ($\phi = 1.61$) using an 80-mm-ID tube [73]

amounts to most of the detonation time [90–93]. Applying this relation to the available experimental data in the literature results in $m = O(1)$ and $n = O(1)$ for the 1–2-μm aluminum–air detonation [73], thus indicating a dependence on initial pressure and gas-phase kinetics. It is noted that the analysis here is limited to a rather global and qualitative approach to elucidate the importance of finite chemical kinetics on the aluminum reaction mechanism in detonation. A combined surface kinetics-diffusion reaction model (2.49)–(2.52) was further suggested to take aluminum chemical kinetics into account, as shown in Sect. 2.2.3 and in the Appendix. The model has been successful in describing both the kinetics-limited transient processes (detonation initiation, abrupt DDT, and detonation instability) and the diffusion-limited combustion of aluminum in the long reaction zone supporting the weak transverse wave structure. More advanced solution will rely on the development of detailed kinetic and diffusional reaction schemes of aluminum particles under conditions of deflagration and detonation. The influence of high-momentum flow and high pressure immediately behind the shock on the mechanical damage and subsequent reaction of the particles must also be quantitatively determined. Recent flyer plate impact experiments simulating detonation in condensed phase matter showed that the atomized aluminum particles were subjected to severe surface damage and breakup to expose fresh bare aluminum, while aluminum flakes were completely broken into nanometric particles [116]. This helped understand why aluminum reacts much faster under high-pressure condensed detonation conditions. There have been no direct experiments simulating the aluminum particle-gas detonation conditions to recover and analyze the particle morphology subjected to a shock interaction.

2.5 Quasi-Detonation in Tubes

In homogeneous gas mixtures, it is well established that detonation waves propagate at less than the equilibrium CJ detonation velocity as the tube diameter is reduced to around the detonation cell size, owing to boundary layer effects and losses to the tube wall [117–124]. Moen et al. [123, 124] indicated that mixtures with irregular cellular structures are influenced less by the confining tube walls than regular-cell mixtures. While fuel–air detonation waves with irregular structures exhibit velocity deficits within 3% of the theoretical CJ value and fail at $d \leqslant \lambda/\pi$, detonations in fuel–oxygen and argon-diluted mixtures with fairly regular structures show larger velocity deficits above 10% and fail in a larger tube at $d \leqslant (1.3\text{–}2)\lambda/\pi$. In general, detonation failure in gaseous mixtures is associated with the disappearance of the transverse wave structure.

Unlike for homogeneous gaseous detonations, a shock-induced supersonic combustion wave can propagate quasi-steadily in tubes much smaller than the detonation cell size in a reactive particle–oxidizing gas flow [8,70,73], owing to distributed particle-induced hot or explosion spots that make the combustion

less sensitive to the disturbance originating in the boundary layer on the tube wall. The observed shock-induced combustion waves were characterized by a shock velocity much less than the equilibrium CJ detonation value, and a pressure profile behind the shock front without a fully developed, self-organized transverse wave structure. Such a shock-induced combustion wave may be referred to as "heterogeneous quasi-detonation."

Quasi-detonation can be achieved through progressive acceleration, as shown in Fig. 2.12, in rich cornstarch–oxygen mixtures in a 53 mm × 53 mm cross section tube ($d \sim 0.4\lambda/\pi$) and was also found in rich cornstarch–air mixtures in a 140-mm tube ($d \sim 0.46\lambda/\pi$) [8, 70]. Figure 2.31 shows two experiments of quasi-detonation development in an 80-mm-diameter tube filled with a 2-μm (H-2) atomized aluminum–air mixture at 2-atm initial pressure [73]. After propagating through 70 tube diameters at low velocities, the wave accelerates more progressively to a shock velocity of 1,080–1,140 m s^{-1} and propagates thereafter quasi-steadily to the tube end. The wave has a velocity deficit of nearly 40% with respect to the theoretical CJ value, and displays compression waves behind the shock front but without an inherent, periodically oscillating transverse wave structure (Fig. 2.32). In fact, this shock speed is close to the critical Mach number that could lead to a DDT. Hence, behind

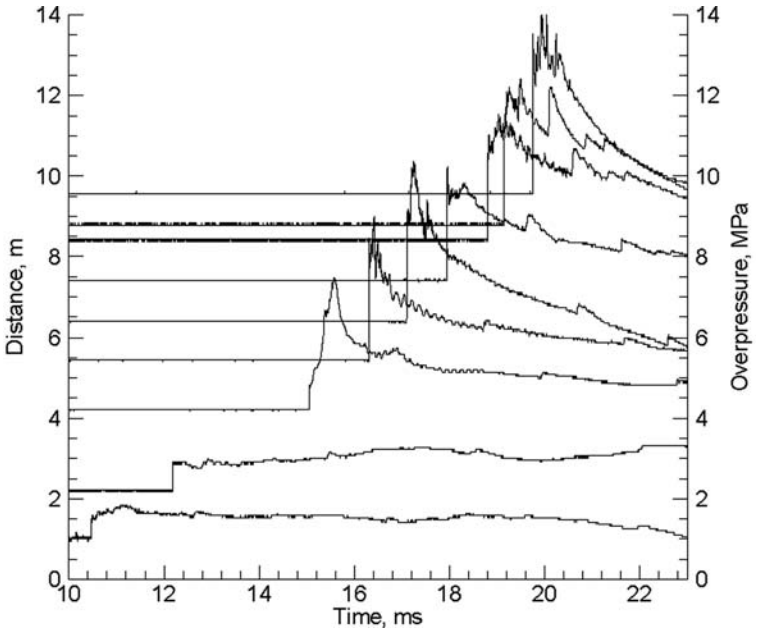

Fig. 2.32. Transition from deflagration to quasi-detonation at 2-atm initial pressure in 1000 g m^{-3}, 2-μm (H-2) aluminum–air mixtures ($\phi = 1.61$) initiated by a 1.1-g explosive detonator in an 80-mm-ID tube. The shock velocity versus distance is given in Fig. 2.31 [73]

the shock front local explosions can take place that are identified by the high compression peaks with subsequent retonation waves propagating backwards. However, the wave is not able to further accelerate to a transverse wave mode detonation because of the small tube confining the development of intrinsic transverse waves. Note that the test section length of 125 diameters may still be insufficient to conclude whether or not the quasi-detonation wave can maintain its quasi-steadiness.

A quasi-detonation wave fails when the distributed particle explosions are suppressed by the momentum and heat loss from gas to particles as well as the expansion and turbulent quenching originating in the boundary layer on the small tube wall. One may predict quasi-detonation limits using the steady two-phase ZND model or, more restrictively, using the unsteady two-phase fluid dynamics model. In the one-dimensional theory, the gas flow velocity with respect to the tube wall, v_{g}, is positive but decreases with the distance behind the shock front, particularly owing to the gas-phase momentum losses to the particles and to the tube wall. Hence, a lower limit can be proposed in which the gas flow velocity with respect to the tube wall is decreased towards zero at the phase-frozen or gaseous sonic plane [125]. Any dust quasi-detonation wave cannot propagate below this absolute limit, because the entire flow would become subsonic with respect to the shock front and the generalized CJ condition (2.2)–(2.4) would be no longer satisfied. Applying $v_{\mathrm{g}} = 0$ at the sonic plane to the same two-phase conservation equations of mass, momentum, and energy used for the ZND model as well as the generalized CJ condition (2.2)–(2.4), one obtains at the phase-frozen sonic plane:

$$\rho_{\mathrm{cr}} = \sigma_{\mathrm{g0}} + \sigma_{\mathrm{p0}}, \tag{2.13}$$

$$e_{\mathrm{cr}} = \frac{(\sigma_{\mathrm{g0}} e_{\mathrm{g0}} + \sigma_{\mathrm{p0}} e_{\mathrm{p0}})}{\sigma_{\mathrm{g0}} + \sigma_{\mathrm{p0}}} + \frac{\int_0^{x_{cr}} Q_{\mathrm{W}}\, \mathrm{d}x}{(\sigma_{\mathrm{g0}} + \sigma_{\mathrm{p0}}) D_{\mathrm{cr}}}, \tag{2.14}$$

$$D_{\mathrm{cr}} = a_{\mathrm{g,cr}}, \tag{2.15}$$

and

$$\left[- \left(q_{\mathrm{p}} + c_{\mathrm{p}} T_{\mathrm{p}} \right) J_{\mathrm{p}} - Q_{\mathrm{p}} + Q_{\mathrm{W}} \right]_{\mathrm{cr}} = 0, \tag{2.16}$$

where the variable e denotes the specific internal energy. The subscript *0* denotes the initial state in front of the shock and the subscript cr represents the critical state at the phase-frozen sonic plane. Equations (2.13)–(2.15) mean that the wave structure begins with a shock front propagating at a critical velocity D_{cr} and ends with a constant-volume combustion boundary at the phase-frozen or gaseous sonic plane. Equations (2.15) and (2.16) satisfy the generalized CJ condition (2.2)–(2.4) and the lower limit solution is therefore a steady solution. Note that for simplicity, the lower limit model (2.13)–(2.16) was obtained by further assuming that at the sonic plane the solid particle velocity with respect to the tube wall approaches zero. Thus, it may not be applicable to mixtures of large particulates.

Under the assumption of an adiabatic process and a full equilibrium critical state, the generalized CJ conditions (2.2)–(2.4) must be replaced by (2.3),

(2.6), and (2.7) and the absolute lower limit model (2.13–2.16) therefore becomes

$$\rho_{\mathrm{cr}} = \sigma_{\mathrm{g0}} + \sigma_{\mathrm{p0}}, \tag{2.13}$$

$$e_{\mathrm{cr}} = \frac{(\sigma_{\mathrm{g0}} e_{\mathrm{g0}} + \sigma_{\mathrm{p0}} e_{\mathrm{p0}})}{\sigma_{\mathrm{g0}} + \sigma_{\mathrm{p0}}}, \tag{2.17}$$

and

$$D_{\mathrm{cr}} = a_{\mathrm{e,cr}}, \tag{2.18}$$

where the subscript cr represents the critical state at the phase-equilibrium sonic plane and the variable $a_{\mathrm{e,cr}}$ is the full equilibrium sound speed. The absolute lower limit based on (2.13), (2.17), and (2.18) can therefore be calculated using an equilibrium constant-volume combustion that results in pressure p_{cr}, temperature T_{cr}, and sound speed $a_{\mathrm{e,cr}}$ equal to the critical shock velocity D_{cr}. The calculated CJ detonation velocities and quasi-detonation critical shock velocities are displayed in Figs. 2.26 and 2.27 for cornstarch–oxygen and aluminum–air mixtures, respectively. As shown in the two figures, the experimental propagation velocities of detonations and quasi-detonations in tubes of various size under different particle dispersion and initiation conditions are bounded between the equilibrium CJ detonation values and the equilibrium constant-volume explosion lower limits. A maximum velocity deficit of about 10% generally holds for the detonation with a transverse wave structure. In the case of the quasi-detonation waves, however, measured shock velocities indicate a deficit as much as beyond 45% with respect to the equilibrium CJ value, yet bounded by the constant-volume lower limit. Between these two limits, the detonation wave undergoes a transition from transverse wave modes to shock-induced quasi-detonation modes. Although the heterogeneous quasi-detonation can be grossly described by the two-phase ZND model, it is essentially unsteady.

2.6 Hybrid Detonation

2.6.1 Hybrid Detonation Modes

While fine solid particles suspended in air are not sensitive to detonation owing to a large transverse wave spacing, their combustion in gaseous detonation products may support so-called hybrid detonation and a hybrid DDT. Theoretically, Afanasieva et al. [26] used the one-dimensional similarity theory to show a spherically or cylindrically diverging "double detonation" wave in a homogenous reactive mixture (Fig. 2.33), in which the first CJ detonation wave is generated from an instantaneous energy release followed by a second shock wave supported by a late energy release. They further indicated the feasibility of such a double-shock detonation solution in a planar wave geometry only with the presence of wall friction and heat losses or when a homogeneous

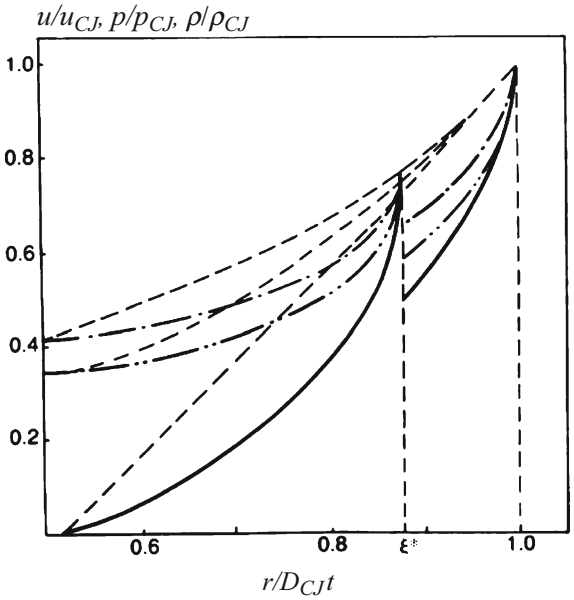

Fig. 2.33. Solution of a spherically diverging double-shock detonation wave using two successive heat releases. u/u_{CJ} *solid line*, p/p_{CJ} *double-dotted dashed line*, ρ/ρ_{CJ} *dotted dashed line*, ξ nondimensional length. [26]

mixture is replaced by a two-phase mixture. Veyssiere [24] first reported experimental evidence of the double-shock detonation in a two-phase mixture of lean hydrogen–air and aluminum particles ($\sigma_p = 55\,g\,m^{-3}$, $10\,\mu m$) in a 69-mm-diameter tube. Since then hybrid detonations have been investigated in several reactive particle–reactive gas systems [29–33].

According to the analysis in Sects. 2.2.2 and 2.2.3, the necessary conditions for a weak detonation solution can be satisfied in reactive gas–particle flow under an appropriate choice of physical and chemical properties of solid particles as well as reactive gas. A set of possible solutions can be realized by selecting the late energy release of particles to meet rear flow or boundary conditions behind the gas reaction zone. Experimentally, three most important hybrid detonation modes (as defined in Sect. 2.2.3) that enhance the impulse loading are introduced in this section over an aluminum concentration range of 25–2,000 $g\,m^{-3}$ [31–33].

Figure 2.34 displays a steady strong hybrid detonation for $\sigma_p = 500\,g\,m^{-3}$, about $2\,\mu m$ atomized aluminum particles (known as H-2 by Valimet) suspended in lean acetylene–air using an 80-mm diameter, 10-m-long tube. The strong hybrid detonation is characterized by the leading shock front followed by a compression wave in the gas detonation zone, caused by a sufficiently large heat release rate of the small particles within the gas reaction zone. This increases the pressure and decreases the detonation cell size with respect

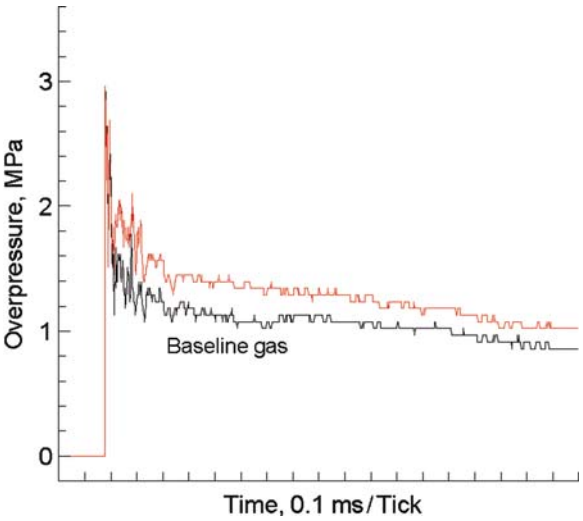

Fig. 2.34. Strong hybrid detonation characterized by the first shock followed by a pressure wave in the gas reaction zone in a mixture of $\phi = 0.8\,C_2H_2$–air and $500\,g\,m^{-3}$, 2-μm (H-2) aluminum particles recorded at $x = 9\,m$ (*upper curve*) compared with detonation in $\phi = 0.8\,C_2H_2$–air (*lower curve*) [31, 32]

to the baseline gas detonation (Figs. 2.34, 2.35) and therefore overdrives gas detonation. The detonation velocity is measured to be $1{,}800\,m\,s^{-1}$, increased by 1.5% from the value of the baseline gas detonation. The secondary compression wave can be identified behind the shock and its inclusion in the gas detonation zone can be more clearly resolved through numerical simulations such as shown in Fig. 2.5a, where the compression wave penetrates two thirds within the detonation zone of the baseline gas alone. The numerical prediction in Fig. 2.5a indicates that the rear flow pressure can be enhanced by a factor of 1.6 with respect to the baseline gas detonation when using a particle concentration of $300\,g\,m^{-3}$.

When the aluminum particle size is increased to about 10 μm (known as H-10 with a mean diameter of 6.5 μm by number and a mean diameter of 13 μm by weight), the particles behave inertly within the gas reaction zone and particle heat release takes place after the gas reaction zone. Therefore, a steady hybrid weak detonation wave results and its propagation along the tube length and comparison with the baseline gas detonation are shown in Figs. 2.36 and 2.37, respectively, from two experiments. This is the type-I double-shock weak solution characterized by a two-shock structure, where the second shock behind the gaseous frozen sonic plane has the same velocity as the leading shock (Fig. 2.38). Aluminum combustion is in a fast deflagration mode for this particle size. Owing to insignificant momentum and heat transferred to the larger particles within the gas detonation zone, the detonation velocity is almost the same as that of the baseline gas detonation and the

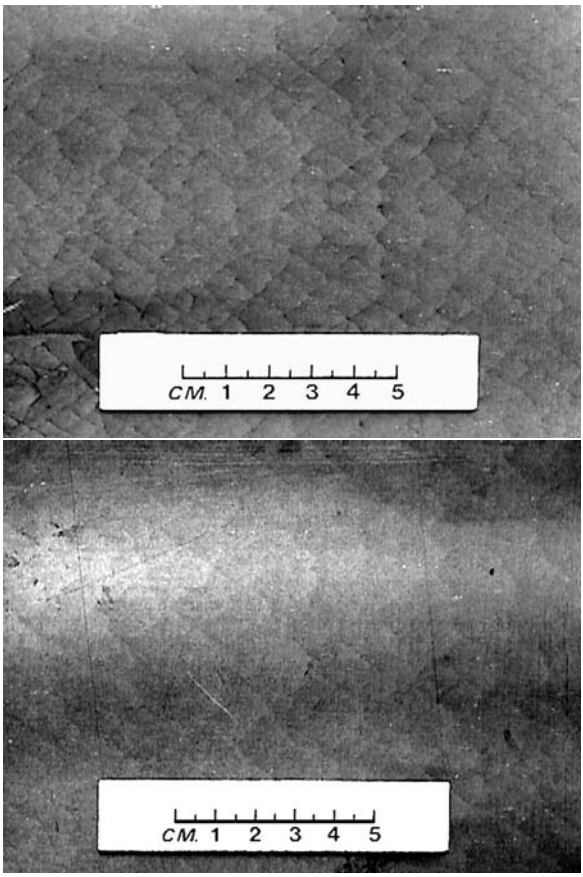

Fig. 2.35. Cellular detonation structure for the strong hybrid detonation in a mixture of $\phi = 0.8\,C_2H_2$–air and $500\,g\,m^{-3}$, 2-μm (H-2) aluminum particles with a cell size of $\lambda = 7 \pm 2\,mm$ (*upper*) compared with detonation in $\phi = 0.8\,C_2H_2$–air with $\lambda = 8 \pm 2\,mm$ (*lower*) [31, 32]

apparent detonation cell size printed on the smoke foil is mainly governed by the gas detonation (Fig. 2.39). This suggests that deflagration of the aluminum particles may only result in a planar secondary shock front subjected to the disturbance of upstream transverse detonation flow conditions.

When the aluminum particle size was increased to about 30 μm (known as H-30, with a mean diameter of 16 μm by number and a mean diameter of 36 μm by weight) to further delay and reduce the heat release rate of the particles, a type-II double-shock weak detonation was observed. This is characterized by two shock fronts, where the second front behind the gaseous sonic plane has a velocity less than the leading front, as demonstrated in Figs. 2.40–2.42. Hence, the second shock recedes from the gas reaction zone to produce an ever-widening region of supersonic flow between the end of the gas reaction

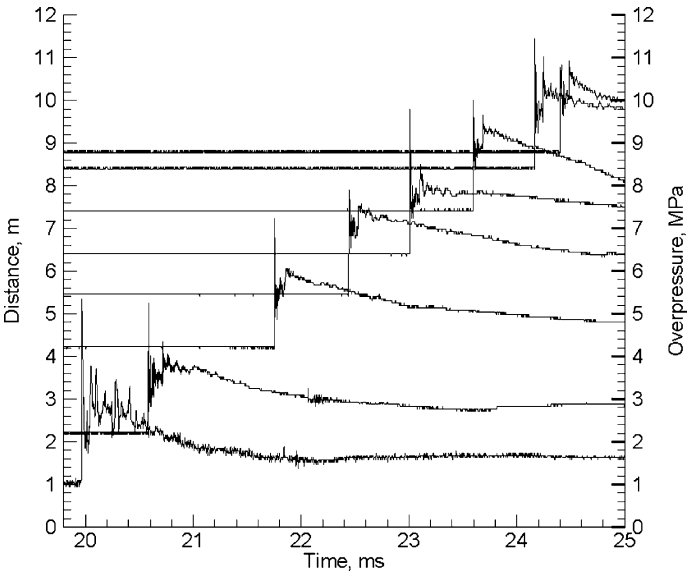

Fig. 2.36. Type-I weak hybrid detonation characterized by two shock fronts where the second shock behind the gas reaction zone has the same velocity as the first in a mixture of $\phi = 0.8\,C_2H_2$–air and $500\,g\,m^{-3}$, 10-μm (H-10) aluminum particles initiated by a 5-g explosive detonator in an 80-mm-ID tube [31, 32]

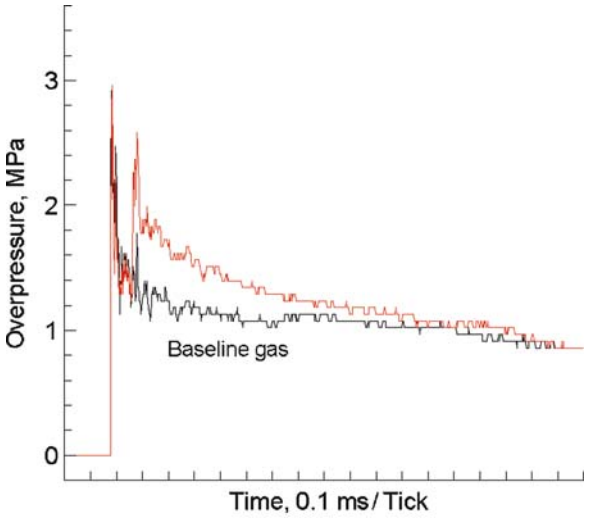

Fig. 2.37. Type-I weak hybrid detonation pressure profile in a mixture of $\phi = 0.8\,C_2H_2$–air and $500\,g\,m^{-3}$, 10-μm (H-10) aluminum particles compared with detonation in $\phi = 0.8\,C_2H_2$–air recorded at x = 8.8 m [31, 32]

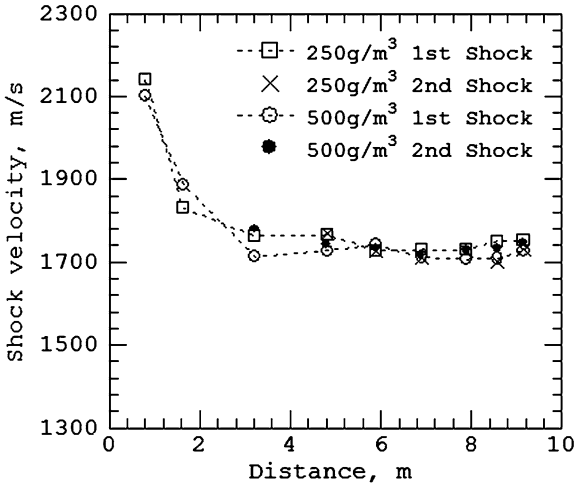

Fig. 2.38. First and second shock velocities versus propagation distance for the type-I weak hybrid detonations in mixtures of $\phi = 0.8\,C_2H_2$–air and 10-μm (H-10) aluminum particles [32]

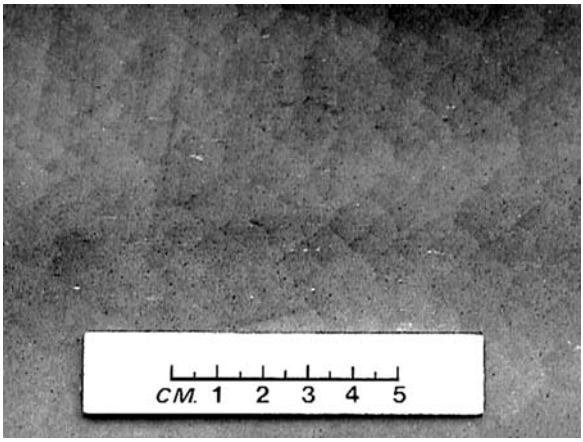

Fig. 2.39. Cellular detonation structure for the type-I weak hybrid detonation in a mixture of $\phi = 0.8\,C_2H_2$–air and $500\,\mathrm{g\,m^{-3}}$, 10-μm (H-10) aluminum particles [32]

zone and itself. While rigorously speaking the flow in this widening region in front of the second shock is unsteady, the experimental velocity of the second shock appears quasi-steady as the wave propagates from $x = 4\,\mathrm{m}$ to the end of the 10-m-long tube. Again owing to the large particles, the first shock velocity and the detonation cell size recorded on the smoke foil correspond to those of the baseline gas detonation. Figure 2.43 shows a double-shock detonation obtained by Veyssiere and Ingignoli [30] in a 69-mm-diameter tube

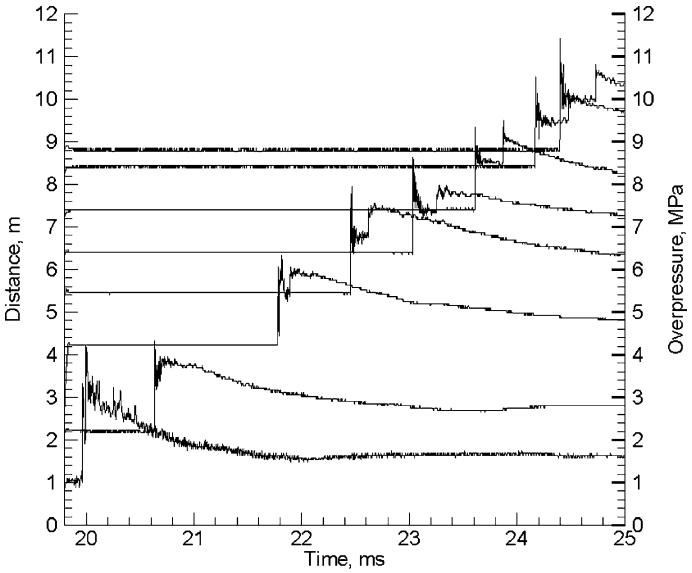

Fig. 2.40. Type-II weak hybrid detonation characterized by two shock fronts where the second shock behind the gas reaction zone has a velocity less than the first in a mixture of $\phi = 0.8\,C_2H_2$–air and $1{,}000\,g\,m^{-3}$, 30-μm (H-30) aluminum particles initiated by a 5-g explosive detonator in an 80-mm-ID tube [32]

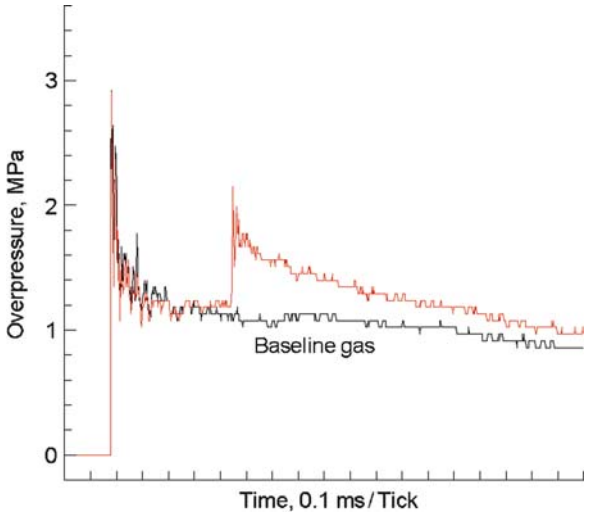

Fig. 2.41. Type-II weak hybrid detonation pressure profile in a mixture of $\phi = 0.8\,C_2H_2$–air and $500\,g\,m^{-3}$, 30-μm (H-30) aluminum particles compared with detonation in $\phi = 0.8C_2H_2$–air recorded at x = 8.8 m [32]

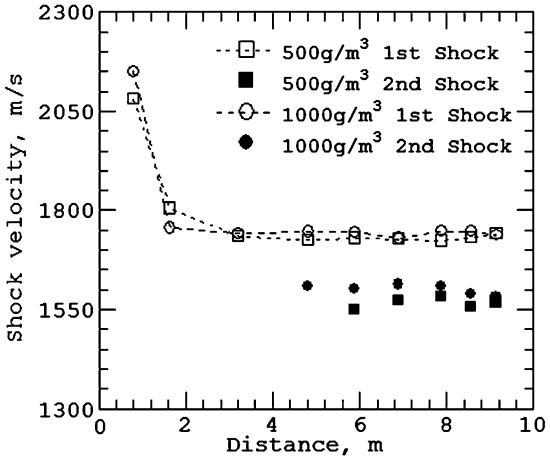

Fig. 2.42. First and second shock velocities versus propagation distance for the type-II weak hybrid detonation in mixtures of $\phi = 0.8\,C_2H_2$–air and 30-μm (H-30) aluminum particles [32]

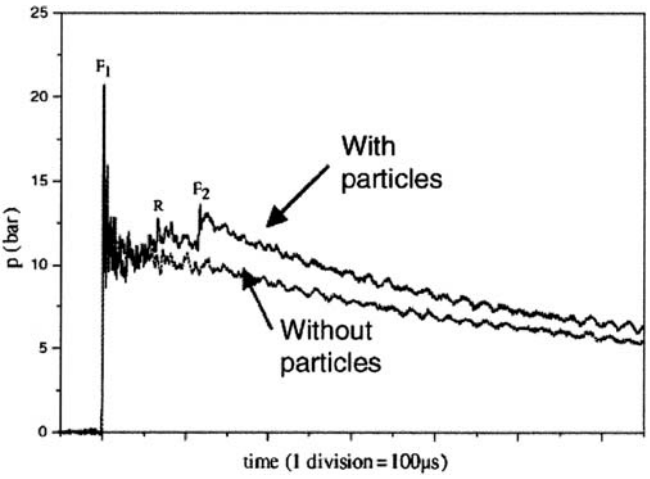

Fig. 2.43. Double-shock detonation in a mixture of $\phi = 0.87\,H_2$–air and $60\,g\,m^{-3}$, 13-μm aluminum particles, compared with detonation in $\phi = 0.87\,H_2$–air using a 69-mm-ID tube [30]

for $\sigma_p = 60\,g\,m^{-3}$, 13-μm atomized aluminum suspended in lean hydrogen–air. Between the two shock fronts, a compression wave appears in front of the second shock. The experimental hybrid detonation modes displayed above justify the theory discussed in Sect. 2.2. The double-shock hybrid detonation waves have also been observed recently in condensed-phase explosives with aluminum particles [126].

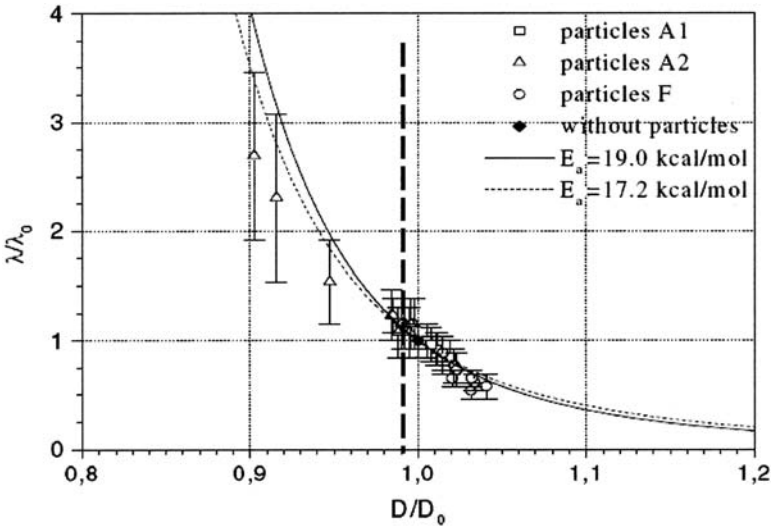

Fig. 2.44. Variation of detonation cell width with detonation velocity in hybrid mixtures of H_2–air and aluminum particles [30]

From the studies of the hybrid detonation for various aluminum particles (flaked, 3.5 and 13 µm atomized in a concentration range of 25–450 g m^{-3}) suspended in hydrogen–air mixtures (with equivalence ratios of ($\phi = 0.87$, 1.06, and 1.32), Veyssiere and Ingignoli [30] correlated the experimental cell size with the detonation velocity according to the Desbordes relation obtained from gaseous overdriven detonation data:

$$\frac{\lambda}{\lambda_{\mathrm{gCJ}}} = \frac{D}{D_{\mathrm{gCJ}}} \mathrm{e}^{E_{\mathrm{g}}[(D_{\mathrm{gCJ}}/D)^2 - 1]/(RT_{\mathrm{vN}})}, \tag{2.19}$$

where parameters E and R are the activation energy and universal gas constant. The subscript gCJ refers to the baseline gas CJ detonation, and vN refers to the von Neumann shock state. A comparison of relation (2.19) with the experimental data is shown in Fig. 2.44.

2.6.2 Influencing Factors

Apart from the effects of particle size and concentration discussed already, the influence of the gaseous detonation parameters and the composition of the products on the hybrid detonation was further investigated for aluminum particles suspended in various fuel–air mixtures with 4–38-mm detonation cell sizes for an initial pressure range of 1–2.5 atm [31–33]. Table 2.2 summarizes the gas detonation properties and product compositions used in the experiments. H_2–air ($\phi = 1.5$), 0.97CO–air + 0.03C_2H_2, and C_2H_2–air ($\phi = 2$)

Table 2.2. Gas detonation properties and product compositions used in hybrid detonation tests

Properties	C_2H_2–air ($\phi = 0.8$)	C_2H_4–air ($\phi = 0.9$)	H_2–air ($\phi = 1$)	H_2–air ($\phi = 1.5$)	0.97CO–air $+0.03C_2H_2$	C_2H_2–air ($\phi = 2$)
D_{CJ} ($\mathrm{m\,s^{-1}}$)	1,765	1,792	1,979	2,087	1,762	2,029
P_{CJ}/p_0	17.56	17.58	15.60	15.20	16.91	21.64
T_{CJ} (K)	2,940	2,860	2,970	2,902	3,003	3,240
Cell size (mm)	8	38	15	15	38	6
O_2 (mol%)	4.127	2.414	1.018	2.529×10^{-2}	6.878×10^{-1}	1.243×10^{-2}
H_2O (mol%)	5.479	10.53	29.496	28.384	2.491	4.105
CO (mol%)	2.989	2.604	0	0	18.307	23.961
CO_2 (mol%)	9.729	9.011	0	0	18.911	1.686
O (mol%)	4.409×10^{-1}	2.474×10^{-1}	2.579×10^{-1}	3.232×10^{-1}	2.284×10^{-1}	5.792×10^{-1}
OH (mol%)	1.136	1.133	2.043	6.874×10^{-1}	5.672×10^{-1}	4.043×10^{-1}
HO_2 (mol%)	9.791×10^{-4}	7.660×10^{-4}	8.175×10^{-4}	4.363×10^{-1}	1.924×10^{-4}	1.963×10^{-5}
NO (mol%)	1.982	1.344		1.276×10^{-1}	7.710×10^{-1}	1.382×10^{-1}
H (mol %)	1.507×-10^{-1}	1.556×10^{-1}	6.266×10^{-1}	1.128	2.217×10^{-1}	1.848
H_2 (mol%)	2.357×10^{-1}	4.367×10^{-1}	3.004	14.630	3.319×10^{-1}	7.593
N_2 (mol%)	73.728	72.117	63.554	54.985	67.482	60.192
Notes				H_2O dominant	CO_2 present	CO dominant
Double-shock detonation [31, 33]	Yes	Yes	Yes	Yes	Yes	Fail

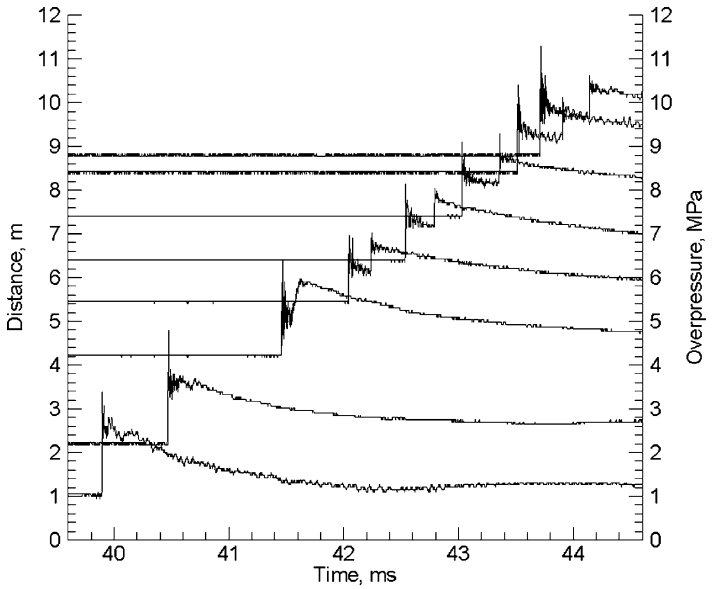

Fig. 2.45. Type-II weak hybrid detonation in a mixture of $\phi = 1.5H_2$–air and $500\,\mathrm{g\,m^{-3}}$, 30-μm (H-30) aluminum particles initiated by a 5-g explosive detonator in an 80-mm-ID tube [33]

were specifically chosen to exclude the oxygen to determine the dependence of the hybrid detonation on water vapor, carbon dioxide, or carbon monoxide, respectively. It was found that the double-shock detonation waves can propagate in detonation products with the presence of oxygen (Fig. 2.40), water vapor, or carbon dioxide using the same initiation source (Figs. 2.45, 2.46). However, as displayed in Fig. 2.47, propagation of the secondary shock fails in detonation products dominated by carbon monoxide even initiated by an acetylene–oxygen detonation driver, a stronger initiation source than used in the other mixtures [33]. The observed secondary shock was the weakest for the C_2H_4–air mixture among the double-shock detonations observed in all the fuel–air mixtures reported in Table 2.2, possibly because of its low detonation temperature.

Owing to the detonation insensitivity of micrometric grades of aluminum particles, the gaseous fuel–air detonation alone may not be sufficient to initiate and accelerate combustion of relatively large aluminum particles quickly enough to form a secondary shock in the gas detonation products flow. It was experimentally found that the C_2H_2–air detonation was initiated directly with a 0.2-g explosive charge mass and propagated steadily, but it cannot initiate the about 30 μm aluminum particles (H-30) suspended in the detonation wave to form the secondary shock until 5 g explosive charge or a stoichiometric C_2H_2–O_2 detonation driver is used for initiation [31]. These results clearly indicate that the expanding fuel–air detonation products alone are insufficient

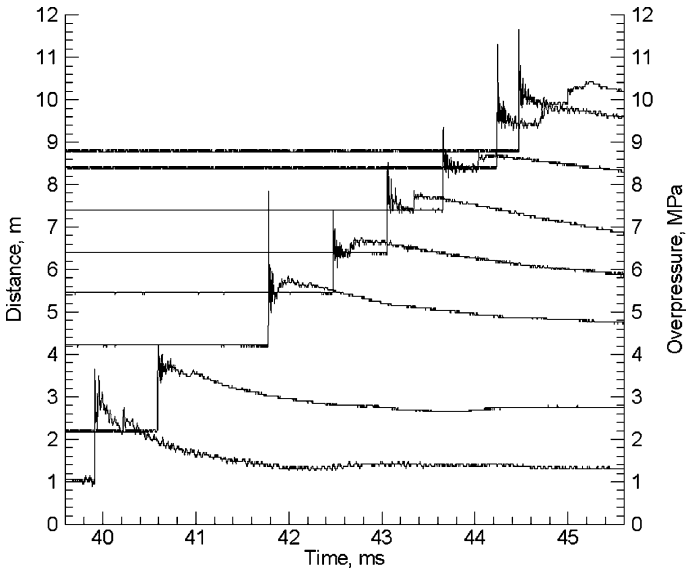

Fig. 2.46. Type-II weak hybrid detonation in a mixture of $0.97CO–air + 0.03C_2H_2$ and $500\,g\,m^{-3}$, 30-μm (H-30) aluminum particles initiated by a 5-g explosive detonator in an 80-mm-ID tube [33]

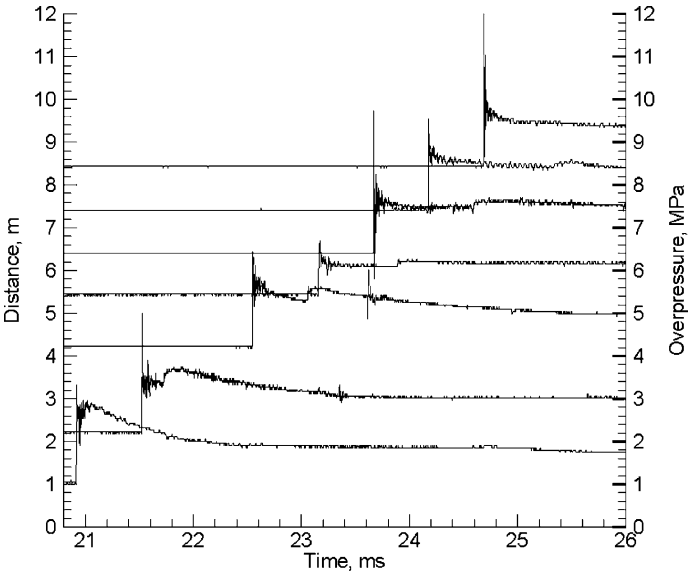

Fig. 2.47. Type-II weak hybrid detonation in a mixture of $\phi = 2C_2H_2$–air and $500\,g\,m^{-3}$, 30-μm (H-30) aluminum particles initiated by a $C_2H_2 + 2.5O_2$ detonation driver in an 80-mm-ID tube [33]

and additional initiation charges (energy power and high temperature) are required to initiate and sustain fast combustion of large aluminum particles to form the secondary shock leading to a double-shock weak detonation.

An increase in initial pressure results in an increase in the heat release rate of particles as discussed in Sect. 2.4.2 and therefore facilitates a hybrid detonation wave with large particles. Experiments showed a stronger two-shock detonation as the initial pressure increases from 1 to 2.5 atm [32].

2.7 Concluding Remarks

The recent efforts in pursuing experiments have led to progress in the understanding of the fundamental mechanisms of detonation waves in dilute solid particle–gas flows. It appears that detonations in fine organic or metallic particles suspended in an oxidizing gas can be divided into heterogeneous detonation waves and quasi-detonation waves. The macroscopic propagation mechanisms for the heterogeneous detonation waves are similar to those for homogeneous gas mixtures, that is, the transverse waves in the single-head spinning or cellular structure provide the coupling between the shock and the reaction. The difference is that the characteristic scale of the detonation cell size for particle–gas mixtures is at least 1 order of magnitude larger than that typically encountered in gas mixtures, owing to the additional time scales introduced by the physical processes of mass, momentum, and heat transfer between the particles and the gas. The time scale of particle reaction is basic and leads to the main time scale for the mass transfer and therefore for the energy release of particles.

The heterogeneous quasi-detonation waves that propagate in tubes much smaller than the characteristic detonation cell size are essentially shock-induced supersonic combustion waves without a fully developed transverse wave structure. The quasi-detonation waves propagate at a shock velocity below the transverse wave mode detonations but above a lower limit characterized by the constant-volume combustion at the sonic plane. While the quasi-detonation wave is unique for reactive particle–gas mixtures, presumably owing to the distributed hot spots or local explosions induced by particles, more investigations are required to understand its propagation mechanisms.

Hybrid detonation waves occur in reactive particles suspended in a detonable gas. A variety of hybrid detonation modes can exist and the solution is a function of the gas reaction time scales and the additional time scales of the mass, momentum, and heat transfer between the particles and the gas. The rate of particle energy release, including its delay time and magnitude, represents a characteristic parameter to specify a possible solution. Among various modes, a strong hybrid detonation wave and two types of double-shock weak detonation wave are most important in practice owing to their enhancement of the gas detonation impulse. The strong hybrid detonation is characterized by the leading shock front followed by a compression wave

resulting from particle combustion in the gas detonation zone, thus overdriving the gas detonation. The two types of double-shock weak detonation wave are featured by a two-shock structure where the second shock front caused by the particle combustion behind the gas reaction zone has a propagation velocity either the same as or less than that of the leading shock front, thus enhancing the impulse loading of the gas detonation. While the strong hybrid detonation reduces the cell size of the baseline gas detonation, the cell sizes in the hybrid weak detonation waves are mainly governed by the gas detonation and provide little information about the sensitivity of aluminum ignition and combustion, which often requires a strong initiation. The variety of hybrid detonation modes and their propagation mechanisms are still the subject of current research efforts.

While the fundamental studies of detonation in solid particle–gas flow have made significant progress, many problems remain to be resolved. The detonation velocity and pressure are experimentally available only for a few solid particle–gas mixtures. More detonation dynamic parameters, including the ordinary cell size and the critical initiation energy, will need to be directly measured. Although the macroscopic mechanisms for the DDT, detonation onset, and propagation seem similar to those for the homogeneous gas detonation, the mechanisms of the heterogeneous detonation and quasi-detonation cannot be fully established without mesoscale studies on the shock and gas flow interactions with the combustion dynamics of distributed particles as well as the influence of the boundary layer. While the heat release rate of particles under detonation conditions is a key parameter in controlling the detonation phenomena in gas–particle flow, there is a lack of direct experimental measurements for a quantitative description of the reaction mechanism and heat release rate even for the popular aluminum particles under shock and detonation conditions. The reliability and predictability of two-phase continuum detonation theory and numerical modeling are currently challenged by the uncertainty of ignition and reaction mechanisms of solid particles under shock and detonation conditions and, for dense solid particle–gas flow, the interphase interaction functions and the equations of state for solid particle flow. Experimental determination and mesoscale modeling would be two critical approaches for resolving these difficult issues.

Appendix

A Two-Phase Fluid Dynamics Equations

A control volume is considered that contains a large number of solid particles immersed in a fluid, but has a small dimension with respect to the macroscopic two-phase flow. The fluid and solid particles are treated as two separate flows which are coupled through their interactions associated with the exchange of mass, momentum, and energy between the two phases. For the supersonic

detonation flow involved, the viscosity and conductivity in the fluid as well as particle gravities are not considered. From the control volume analysis, the one-dimensional conservation equations can be derived as listed below in the laboratory coordinate frame.
Solid phase:

$$\text{Mass}: \ \frac{\partial \sigma_{\mathrm{p}}}{\partial t} + \frac{\partial}{\partial x}\left(\sigma_{\mathrm{p}} u_{\mathrm{p}}\right) = J_{\mathrm{p}}. \tag{2.20}$$

$$\text{Momentum}: \ \frac{\partial}{\partial t}\left(\sigma_{\mathrm{p}} u_{\mathrm{p}}\right) + \frac{\partial}{\partial x}\left(\sigma_{\mathrm{p}} u_{\mathrm{p}}^2 + p_{\mathrm{p}}\right) = u_{\mathrm{p}} J_{\mathrm{p}} + f_{\mathrm{p}}. \tag{2.21}$$

Energy:

$$\frac{\partial}{\partial t}\left[\sigma_{\mathrm{p}}(e_{\mathrm{p}} + u_{\mathrm{p}}^2/2)\right] + \frac{\partial}{\partial x}\left[\sigma_{\mathrm{p}} u_{\mathrm{p}}(e_{\mathrm{p}} + u_{\mathrm{p}}^2/2 + p_{\mathrm{p}}/\sigma_{\mathrm{p}})\right] = (e_{\mathrm{p}} + u_{\mathrm{p}}^2/2) J_{\mathrm{p}} + u_{\mathrm{p}} f_{\mathrm{p}} + Q_{\mathrm{p}}. \tag{2.22}$$

$$\text{Number density}: \ \frac{\partial n_{\mathrm{p}}}{\partial t} + \frac{\partial}{\partial x}\left(n_{\mathrm{p}} u_{\mathrm{p}}\right) = \Psi_{\mathrm{p}}. \tag{2.23}$$

Fluid phase:

$$\text{Mass}: \ \frac{\partial \phi_{\mathrm{g}} \rho_{\mathrm{g}}}{\partial t} + \frac{\partial}{\partial x}\left(\phi_{\mathrm{g}} \rho_{\mathrm{g}} u_{\mathrm{g}}\right) = -J_{\mathrm{p}}. \tag{2.24}$$

$$\text{Momentum}: \ \frac{\partial}{\partial}(\phi_{\mathrm{g}} \rho_{\mathrm{g}} u_{\mathrm{g}}) + \frac{\partial}{\partial x}\left(\phi_{\mathrm{g}} \rho_{\mathrm{g}} u_{\mathrm{g}}^2 + \phi_{\mathrm{g}} p_{\mathrm{g}}\right) = -u_{\mathrm{p}} J_{\mathrm{p}} - f_{\mathrm{p}}. \tag{2.25}$$

Energy:

$$\frac{\partial}{\partial t}\left[\phi_{\mathrm{g}} \rho_{\mathrm{g}}(e_{\mathrm{g}} + u_{\mathrm{g}}^2/2)\right] + \frac{\partial}{\partial x}\left[\phi_{\mathrm{g}} \rho_{\mathrm{g}} u_{\mathrm{g}}\left(e_{\mathrm{g}} + u_{\mathrm{g}}^2/2 + p_{\mathrm{g}}/\rho_{\mathrm{g}}\right)\right] = -(e_{\mathrm{p}} + u_{\mathrm{p}}^2/2) J_{\mathrm{p}} - u_{\mathrm{p}} f_{\mathrm{p}} - Q_{\mathrm{p}}, \tag{2.26}$$

$$\text{Species}: \ \frac{\partial}{\partial t}(\phi_{\mathrm{g}} \rho_{\mathrm{g}} Y_j) + \frac{\mathrm{d}}{\mathrm{d}x}\left(\phi_{\mathrm{g}} \rho_{\mathrm{g}} u_{\mathrm{g}} Y_j\right) = w_j, \qquad j = 1, \ldots, \ M, \tag{2.27}$$

where variables u, ρ, σ, e, and Y are the flow velocity, material density, partial density (or mass concentration), specific internal energy including chemical energy, and mass fraction of the gas species, respectively. The subscripts p and g refer to the solid particle and fluid phase, respectively.

The volume fractions of each phase are constrained by

$$\phi_{\mathrm{g}} + \phi_{\mathrm{p}} = 1. \tag{2.28}$$

The partial density or mass concentration of the particle flow is related to the particle material density by

$$\sigma_{\mathrm{p}} = \phi_{\mathrm{p}} \rho_{\mathrm{s}}. \tag{2.29}$$

The number density (particle number per volume) for spherical solid particles is defined by

$$n_{\mathrm{p}} = \frac{6\phi_{\mathrm{p}}}{\pi d_{\mathrm{p}}^3} = \frac{6\sigma_{\mathrm{p}}}{\pi \rho_{\mathrm{s}} d_{\mathrm{p}}^3}, \tag{2.30}$$

where d_{p} is the particle diameter. The variable p_{g} is the pressure of the gas flow occupying the partial volume ϕ_{g}, while p_{p} is the pressure of the particle flow in the control volume without interstitial gas and it is different from the material pressure inside the particle. The definition of the pressure of particle flow will be discussed in the next section. The mixture density ρ and pressure p are the sum of the partial density and the pressure, respectively:

$$\rho = \sigma_{\mathrm{g}} + \sigma_{\mathrm{p}} = \phi_{\mathrm{g}}\rho_{\mathrm{g}} + \sigma_{\mathrm{p}}, \quad p = \phi_{\mathrm{g}} p_{\mathrm{g}} + p_{\mathrm{p}}. \tag{2.31}$$

The source terms J_{p}, f_{p},Q_{p}, and Ψ_{p} are the rates of interphase transfer functions representing the exchange for mass, momentum, energy, and the solid particle number between the phases. Evaporation and combustion of solid particles are included in the rate of mass transfer J_{p}, which adopts a negative value when particle depletion occurs. The force f_{p} and the rate of energy transfer Q_{p} have the same sign as the phase velocity difference $u_{\mathrm{g}} - u_{\mathrm{p}}$ and the phase temperature difference T_{g}–T_{p}, respectively. Solid particle agglomeration or fragmentation can be controlled through the rate of particle number change Ψ_{p}. If the reaction zone is large, the loss due to the tube wall or other lateral boundary conditions can also be included by the source terms for the rate of the momentum and heat exchange with the lateral boundaries. The source terms will be described later and various forms of transfer functions can be found in [10–12,27,28,50–56]. Since the source terms are modeled according to physical rules and empirical co-relations, the predictability of the two-phase fluid dynamics theory strongly depends on the choice of source term models for a particular flow topology [54].

The conservative form of the two-phase fluid dynamics (2.20)–(2.27) is convenient in numerical implementation of the Eulerian approaches. For problems involving multiple particle sizes or particles with a size distribution, the conservation equations for the particle flow can be rewritten in the Lagrangian derivative form that can be straightforwardly resolved in the group Lagrangian approaches. For a steady shock or detonation problem, (2.20)–(2.27) are often rewritten in a shock-attached coordinate system [$x' = x_{\mathrm{D}}(t) - x, \quad t' = t$, where $x_{\mathrm{D}}(t)$ is the trajectory of the shock front]. The steady conservation equations in the shock-attached coordinate system remain the same form as (2.20)–(2.27) in which the $\partial/\partial t$ derivative terms are removed.

B Equations of State

Depending on the volume fraction occupied by the particle phase, a particular gas–particle flow topology can be classified as a dilute particle–gas flow

($\phi_\mathrm{p} < 0.01$), a dense particle–gas flow ($0.01 \leqslant \phi_\mathrm{p} < \phi_\mathrm{p,pack}$), or a granular flow ($\phi_\mathrm{p} \geq \phi_\mathrm{p,pack}$), where $\phi_\mathrm{p,pack}$ refers to the volume fraction of a packed particle system. While the conservation relations (2.20)–(2.27) are valid for any continuum two-phase flow, the equations of state for continuum fluid and discrete particles must be specified to provide closure for the solution of a specific gas–particle flow.

Equations of state for gases (e.g., ideal equation of state) can be found in textbooks. For many dense gases, liquids, and solids under high-pressure shock compression, the Grüneisen equation is applied in the form

$$p = p_\mathrm{H} + \frac{\Gamma_\mathrm{s}}{v}(e - e_\mathrm{H}). \tag{2.32}$$

The subscript H denotes the shock Hugoniot state determined by the Hugoniot relations

$$p_\mathrm{H} = \frac{c^2(v_0 - v)}{\left[v_0 - S(v_0 - v)\right]^2}, \tag{2.33}$$

$$e_\mathrm{H} = \frac{1}{2}\left[\frac{c(v_0 - v)}{v_0 - S(v_0 - v)}\right]^2, \tag{2.34}$$

with the specific volume $v = 1/\rho$ and the Grüneisen coefficient $\Gamma_\mathrm{s} = 2\mathrm{S} - 1$. Γ_s is also related to the ratio of the specific heats by $\gamma = \Gamma_\mathrm{s} + 1$. Parameters c and S are from the linear relationship of shock velocity with the flow velocity: $D = c + Su$ and can be found in the handbook of Marsh [127]. Similarly to (2.32), an equation of state for temperature can be written, from which the Hugoniot temperature can also be obtained [128].

The Jones–Wilkins–Lee equation of state is often used to model the detonation product gases and their subsequent adiabatic expansion in an explosion [129]. The constants in the Jones–Wilkins–Lee equation of state used to be the best fits to experimental measurements and hydrodynamic calculations. Now they can also be easily calculated for various energetic materials using an equilibrium code such as Cheetah [130]. Many sophisticated and specific equations of state for real gases, liquids, and solids can be found in the literature suitable for numerical solutions.

The following discussion is focused on the discrete particle flow without interstitial gas. In the limit of a dilute particle flow in which the particles are far apart from each other, the interactions between the particles are negligible. Hence, in analogy to a dilute gas molecule system, the pressure of the particle flow can be neglected: $p_\mathrm{p} = 0$ [57]. Consequently, the sound speed of the particle flow is negligible. If the shock or detonation pressure is much lower than the particle material strength, the particle material can be considered to be incompressible: $\rho_\mathrm{s} = \text{constant}$.

At the other extreme limit of a granular flow where the particles are closely packed, the competition between the stresses within the particle and the external forces, exerted by the neighboring particles and the gas in voids, forms

the main mechanism for the compaction, compression, and deformation of the particles. Applying the second law of thermodynamics (entropy inequality), Baer and Nunziato [52] obtained a dynamic compaction equation controlled by the mechanical nonequilibrium between the pressure inside the solid particles, p_s, and the pressure in the gas plus the pressure due to contact forces between the particles, β_s:

$$\frac{\mathrm{d}\phi_\mathrm{p}}{\mathrm{d}t} = \frac{\partial \phi_\mathrm{p}}{\partial t} + u_\mathrm{p}\frac{\partial \phi_\mathrm{p}}{\partial x} = \Pi_\mathrm{p} + \frac{J_\mathrm{p}}{\rho_\mathrm{s}} = \frac{\phi_\mathrm{p}\phi_\mathrm{g}}{\mu_\mathrm{c}}\left[p_\mathrm{s} - (p_\mathrm{g} + \beta_\mathrm{s})\right] + \frac{J_\mathrm{p}}{\rho_\mathrm{s}}. \tag{2.35}$$

This equation describes the evolution of the solid volume fraction due to the change of packing configuration, where the coefficient μ_c is interpreted as the compaction viscosity. Owing to large solid volume fractions, the pressure and sound speed of the granular flow are close to those in the solid itself. Hence, the volume-averaging assumption (2.29) can be extended to the pressure of the discrete particle flow p_p [52, 53]:

$$p_\mathrm{p} = \phi_\mathrm{p} p_\mathrm{s}. \tag{2.36}$$

Between the above two limits of particle flows, there exists a regime where the high-speed particles mostly interact through inelastic collisions and the definitions of the pressure and sound speed of the particle flow have not been well established. Difficulties are encountered when the volume-averaging assumption (2.36) is extended to dense and dilute particle flows. From (2.29) and (2.36), although the pressure of the particle flow approaches zero as the solid volume fraction approaches zero, the resultant phase-frozen sound speed of the particle flow always equals the sound speed of the solid regardless of how small the solid volume fraction becomes. This conclusion contradicts the common fact that the sound speed of the solid flow diminishes rapidly as the solid volume fraction approaches zero. Clearly, the sound speed in a discrete particle flow is different from that of the solid owing to the spaces between the particles. Though the partial pressure rule (2.36) has often been used in the classical theory of gas mixtures, distribution of the solid pressure into a large space following (2.36) may be physically unrealizable.

The analogy between the random motion of granular particles and the thermal motion of gas molecules inspired researchers to apply the gas kinetic theory to the granular and dense particle flow [131, 132]. This theory was recently applied to a planar shock wave sweeping over a bulk dust layer to lift the dust behind the shock [133]. Using the kinetic theory, one defines a concept of "granular temperature" in terms of velocity fluctuation around the mean particle flow velocity. Consequently, the pressure of the particle flow and the squared sound speed are proportional to the granular temperature. However, the transport equation for granular temperature indicates that the rate of the granular temperature change and therefore the sound speed would increase towards infinity as the solid volume fraction approaches zero. Some studies attempted to include the gas drag to explain this contradiction between the

theory prediction and the experimental fact [134]. Although a macroscopic particle system and a molecular system are analogous in many ways, the two systems have fundamental differences. At the root of the unique status of dense high-speed particle flow is the existence of a large number of path-dependent inelastic particle collisions. A careful study of these fundamental differences is necessary and may lead to a new analysis of dissipative statistical mechanics. As the available computational power increases, the dissipative statistical mechanical analysis will be made easier through direct simulations of a large number of particles at the "microscopic" particle scale.

A correct definition of the sound speed in the dense particle flow is crucial for describing compressible phenomena of the flow. Owing to the lack of a sound theoretical basis, the pressure and the sound speed for the transition regime of dense particle flow were estimated using a heuristic interpolation method [54]. This is realized by applying a weighting function to the solid volume fraction between the solid limit and the dilute particle flow limit. This approximation was expected to give reasonable results for problems in which the transition regime from a granular flow to a dilute solid flow occurs in a relatively short time, such as rapid dispersal of solid particles from detonation of a condensed explosive. The heuristic model is assumed to have the form

$$p_{\mathrm{p}} = P(\rho_{\mathrm{s}}, e_{\mathrm{p}}, \phi_{\mathrm{p}}), \tag{2.37}$$

which satisfies

$$\begin{aligned} &P(\rho_{\mathrm{s}}, e_{\mathrm{p}}, \phi_{\mathrm{p}}) \to p_{\mathrm{s}}(\rho_{\mathrm{s}}, e_{\mathrm{p}}), \text{ as } \phi_{\mathrm{p}} \to 1, \\ &P(\rho_{\mathrm{s}}, e_{\mathrm{p}}, \phi_{\mathrm{p}})/\sigma_{\mathrm{p}} \to 0, \text{ as } \phi_{\mathrm{p}} \to 0 \ \&\ \rho_{\mathrm{s}} \ \to \rho_{\mathrm{s0}}, \end{aligned} \tag{2.38}$$

with σ_{p} obeying (2.29). The variable e_{p} is the specific internal energy defined as the internal energy per mass of the discrete particle flow, and therefore equals the specific internal energy of the solid, e_{s}. Defining the phase-frozen sound speed of a particle flow by

$$a_{\mathrm{p}}^2 = \left(\frac{\partial p_{\mathrm{p}}}{\partial \sigma_{\mathrm{p}}}\right)_{s_{\mathrm{p}},\phi_{\mathrm{p}}} = \frac{1}{\phi_{\mathrm{p}}}\left(\frac{\partial p_{\mathrm{p}}}{\partial \rho_{\mathrm{s}}}\right)_{e_{\mathrm{p}},\phi_{\mathrm{p}}} + \frac{p_{\mathrm{p}}}{\phi_{\mathrm{p}}^2 \rho_{\mathrm{s}}^2}\left(\frac{\partial p_{\mathrm{p}}}{\partial e_{\mathrm{p}}}\right)_{\sigma_{\mathrm{p}},\phi_{\mathrm{p}}}, \tag{2.39}$$

where s_{p} denotes the specific entropy of the particle flow, the heuristic equations of state (2.37)–(2.39) yield

$$a_{\mathrm{p}} \to a_{\mathrm{s}} \text{ as } \phi_{\mathrm{p}} \to 1 \text{ and } a_{\mathrm{p}} \to 0 \text{ as } \phi_{\mathrm{p}} \to 0. \tag{2.40}$$

As an example, applying (2.37)–(2.40) to the Grüneisen equation of state (2.32), one can formally write a heuristic equation of state for a dense particle flow as

$$p_{\mathrm{p}} = g_1(\phi_{\mathrm{p}}) p_{\mathrm{H}}(\rho_{\mathrm{s}}) + g_2(\phi_{\mathrm{p}}) \Gamma_{\mathrm{s}} \rho_{\mathrm{s}} [e_{\mathrm{s}} - e_{\mathrm{H}}(\rho_{\mathrm{s}})], \tag{2.41}$$

with

$$g_1(\phi_{\mathrm{p}}) = O(\phi_{\mathrm{p}}^m),\ g_2(\phi_{\mathrm{p}}) = O(\phi_{\mathrm{p}}^n) \text{ with } m \geq 1 \text{ and } n > 1. \tag{2.42}$$

Here, p_{H} equals the value on the solid Hugoniot when $\rho_{\mathrm{s}}/\rho_{\mathrm{s0}} \geq 0$ and is assumed to be zero when $\rho_{\mathrm{s}}/\rho_{\mathrm{s0}} < 0$.

The particle temperature is computed from the internal energy:

$$T_{\mathrm{p}} = \begin{cases} e_{\mathrm{p}}/c_{\mathrm{pv}} & \text{for } e_{\mathrm{p}} < c_{\mathrm{pv}}T_{\mathrm{pm}} \\ T_{\mathrm{pm}} & \text{for } c_{\mathrm{pv}}T_{\mathrm{pm}} < e_{\mathrm{p}} < c_{\mathrm{pv}}T_{\mathrm{pm}} + L_{\mathrm{m}} \\ (e_{\mathrm{p}} - L_{\mathrm{m}})/c_{\mathrm{pv}} & \text{for } c_{\mathrm{pv}}T_{\mathrm{pm}} + L_{\mathrm{m}} < e_{\mathrm{p}} < c_{\mathrm{pv}}T_{\mathrm{pb}} + L_{\mathrm{m}} \end{cases}, \tag{2.43}$$

where the boiling point can be obtained from [135]

$$T_{\mathrm{pb}} = \frac{L_{\mathrm{v}} - 2W_{\mathrm{p}}p_{\mathrm{g}}/\rho_{\mathrm{p}}}{R\,\ln(p^*/p_{\mathrm{g}})}. \tag{2.44}$$

Here, p^* is a constant, c_{pv} denotes the specific heat at constant volume for the particle, and L_{m} and L_{v} are the latent heat of melting and vaporization of the particle material respectively. The internal energy in (2.43) does not include chemical energy. Equation (2.44) includes the correction due to high surrounding gas pressure such as in the detonation products of condensed explosives. As $W_{\mathrm{p}}p_{\mathrm{g}}/\rho_{\mathrm{p}}L_{\mathrm{v}} \ll 1$, the second term in the numerator on the right-hand side is negligible and (2.44) is reduced to the Clausius–Clapeyron equation. For example, the boiling point for aluminum at 7×10^8 Pa is 7,315 K from (2.44) and 9,072 K from the Clausius–Clapeyron relation. A similar correction term due to high gas pressure can be introduced in the equation for the melting point T_{pm}.

C Interphase Transfers

C.1 Mass Transfer

Neglecting the influence of direct interactions between particles, the rate of mass transfer, J_{p} in kilograms per cubic meter per second, due to particle combustion in a diffusion-limited reaction model is expressed as [27, 136]

$$J_{\mathrm{p}} = n_{\mathrm{p}}\frac{\mathrm{d}m_{\mathrm{p}}}{\mathrm{d}t} = n_{\mathrm{p}}\pi d_{\mathrm{p}}^2\rho_{\mathrm{s}}\frac{\mathrm{d}r_{\mathrm{p}}}{\mathrm{d}t} = \frac{3\sigma_{\mathrm{p}}}{t_{\mathrm{b}}}\left(1 + 0.276\,Re^{1/2}Pr^{1/3}\right), \text{ if } T_{\mathrm{p}} \geq T_{\mathrm{ign}}, \tag{2.45}$$

otherwise $J_{\mathrm{p}} = 0$. In (2.45), the particle burning time is

$$t_{\mathrm{b}} = Kd_{\mathrm{p0}}^n/Y_{\mathrm{oxi}}^{\alpha}. \tag{2.46}$$

Here, m_{p}, and r_{p} are the particle mass and radius, respectively. The parameters K, d_{p0}, Y_{oxi}, and T_{ign} are the rate coefficient, initial particle diameter, mass fraction of oxidizing gases, and particle ignition temperature respectively. $n = 2$ has often been used, which essentially assumes infinite chemical kinetics. In fact, a diffusion-limited d^2 law for the particle burning time can be derived from the liquid droplet combustion theory in a quiescent flow [99]. The model is independent of temperature and pressure and assumes a particle

ignition temperature above which particles react. $n < 2$ implies the effect of finite gas-phase kinetics and possibly convective flow effects [99]. The term including the Reynolds number Re and the gas-phase Prandtl number Pr was therefore introduced in (2.45) presumably to consider the convective flow effect, where the Reynolds number is defined by the velocity difference between the two phases:

$$Re = \rho_{\mathrm{g}} d_{\mathrm{p}} \left| u_{\mathrm{g}} - u_{\mathrm{p}} \right| / \mu_{\mathrm{g}}, \tag{2.47}$$

with a gas-phase dynamic viscosity $\mu_{\mathrm{g}} = \mu_{\mathrm{g}}(T_{\mathrm{g}})$.

For aluminum combustion, $n = 1.75$, $k = 7.3 \times 10^{-6}\,\mu\mathrm{m}^{1.75}\ \mathrm{s}^{-1}$ (with d_{p0} in micrometers), and $\alpha = 0.9$ have been used in rocket motor propulsion applications where T_{ign} is near the aluminum oxide melting point in quiescent flow conditions [136]. To model the propagation of detonation in aluminum–gas mixtures, $n = 2$, $k = 4 \times 10^{-6}\,\mu\mathrm{m}^2\ \mathrm{s}^{-1}$ (with d_{p0} in micrometers), and $\alpha = 0.9$ has been suggested where T_{ign} has a value near the melting point of aluminum (933–1,350 K) considering possible oxide coating breakup under shock conditions [14, 27].

For kinetics-limited reaction of solid particles, a surface heterogeneous reaction model can be expressed by

$$J_{\mathrm{p}} = -n_{\mathrm{p}} \pi d_{\mathrm{p}}^2 p_{\mathrm{oxi}}^m k_0 \mathrm{e}^{-E/RT_{\mathrm{p}}} = -\frac{6\sigma_{\mathrm{p}} p_{\mathrm{oxi}}^m}{\rho_{\mathrm{s}} d_{\mathrm{p}}} k_0 \mathrm{e}^{-E/RT_{\mathrm{p}}}, \tag{2.48}$$

where p_{oxi}, k_0, E, and R are the partial pressure of oxidizing gas, the rate coefficient, the activation energy, and the universal gas constant. This model is suitable for solid particles for which the shock ignition delay follows a logarithmically linear relation with $1/T_{\mathrm{p}}$. Sichel et al. [111] used this model in studying the temperature distribution inside a particle during the shock ignition.

For many solid particles under shocked flow conditions, both surface chemical kinetics and diffusion reaction can take place. Field and Elperin et al. [137] applied a hybrid reaction model combining the surface oxidation and diffusion reaction to carbon particle reaction in oxygen behind a shock wave. As evidenced from the experiments reviewed in Sects. 2.3 and 2.4, micrometric and nanometric aluminum–air detonation strongly depends on the initial pressure; violent abrupt DDT suggests a highly nonlinear dependence on temperature via chemical kinetics. On the other hand, the aluminum–air detonation waves exhibit a weak transverse wave structure with a large transverse wave spacing, thus indicating slower energy release rates in the later phase of aluminum combustion that supports the detonation propagation. Hence, a kinetics–diffusion hybrid aluminum reaction model is proposed in the form [22]

$$J_{\mathrm{p}} = -n_{\mathrm{p}} \pi d_{\mathrm{p}}^2 k_{\mathrm{p}} = -n_{\mathrm{p}} \pi d_{\mathrm{p}}^2 \frac{\upsilon_{\mathrm{p}} W_{\mathrm{p}}}{\upsilon_{\mathrm{oxi}} W_{\mathrm{oxi}}} k = -\frac{6\sigma_{\mathrm{p}}}{\rho_{\mathrm{s}} d_{\mathrm{p}}} \frac{\upsilon_{\mathrm{p}} W_{\mathrm{p}}}{\upsilon_{\mathrm{oxi}} W_{\mathrm{oxi}}} k, \tag{2.49}$$

with

$$k = \frac{k_\mathrm{d} k_\mathrm{s}}{k_\mathrm{d} + k_\mathrm{s}} C_\mathrm{oxi}, \tag{2.50}$$

$$k_\mathrm{d} = \frac{\nu_\mathrm{oxi} W_\mathrm{oxi}}{\nu_\mathrm{p} W_\mathrm{p}} \frac{\rho_\mathrm{s} d_\mathrm{p}}{2 C_\mathrm{total} K d_\mathrm{p0}^2} (1 + 0.276\, Re^{1/2} Pr^{1/3}), \tag{2.51}$$

and

$$k_\mathrm{s} = k_0 \mathrm{e}^{-E/RT_\mathrm{ps}}, \quad \text{with } T_\mathrm{ps} = (T + T_\mathrm{p})/2, \tag{2.52}$$

where T_ps is the particle surface temperature. k_p and k are the mass depletion rates (equaling the mass flux) of the particle and the oxidizing gas at the particle surface in the particle radial direction, respectively. k_d and k_s are the rate coefficients for diffusion and surface reaction, respectively. W, ν, C_oxi, and C_total denote the molecular weight, stoichiometric coefficient, oxidizing gas molar concentration and total gas molar concentration, respectively. The model (2.49)–(2.52) becomes surface-kinetics-limited (i.e., $k \to k_\mathrm{s}$) when $k_\mathrm{s}/k_\mathrm{d} \ll 1$, and approaches the diffusion-limited reaction model (2.45) and (2.46) but without an ignition temperature assumption as $k \to k_\mathrm{d}$ if $k_\mathrm{s}/k_\mathrm{d} \gg 1$.

The hybrid reaction model (2.49)–(2.52) depends on temperature and pressure (via oxidizing gas concentration) and does not need a presumed particle ignition temperature. Hence, the model is capable of describing transient combustion of particles such as an abrupt DDT via a local explosion center in an aluminum–air mixture as shown in Fig. 2.48. In this numerical computation, $K = 4 \times 10^6\,\mathrm{s\ m^{-2}}$, $k_0 = 1.2 \times 10^6\,\mathrm{kg\text{-}m\,(mol\text{-}s)^{(-1)}}$, and $E = 71.1\,\mathrm{kJ\ mol^{-1}}$

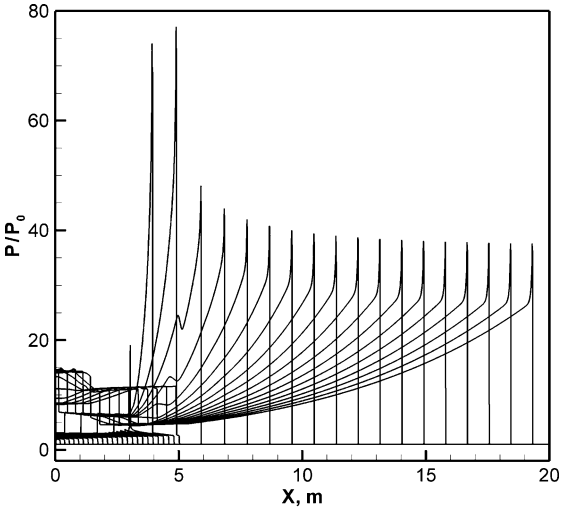

Fig. 2.48. Numerical DDT pressures in a 2-μm aluminum–air mixture at $\sigma_\mathrm{p} = 1250\,\mathrm{g\,m^{-3}}$ and $p_0 = 2.5\,\mathrm{atm}$ [22]

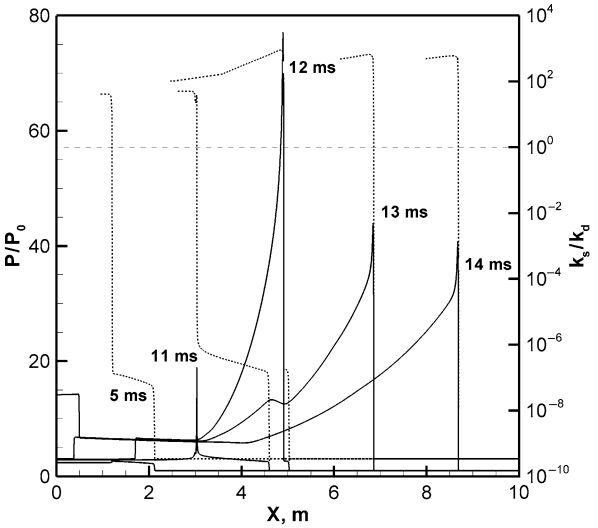

Fig. 2.49. Early process in Fig. 2.48. *Solid line* p/p_0, *dashed line* k_s/k_d [22]

were employed [22], using a 6.13 kJ m^{-2} hot spot zone (1 mm long with $p = 8.56p_0$, $T = 2{,}567$ K, and $T_p = 300$ K) for initiation at the beginning of a 2-μm aluminum–air mixture at $\sigma_p = 1{,}250$ g m^{-3} and an initial pressure of $p_0 = 2.5$ atm (the same initial conditions as for the 2.5-atm experiment displayed in Fig. 2.31). During the early DDT process, $k_s/k_d < 1$ holds behind the shock front in an induction stage that leads to local explosion, thus indicating a kinetics-limited reaction (Fig. 2.49). As the local explosion develops, the particle temperature rapidly increases and therefore results in a rapid increase in k_s/k_d. Once the detonation forms, $k_s/k_d > 1$ holds after a very short kinetics induction time behind the shock, thus showing a diffusion-limited reaction for most of the aluminum mass. The phenomena are in agreement with the experimental observation and therefore the hybrid model properly describes the detonation initiation and the abrupt DDT. Under the same initial conditions and hot spot zone, the abrupt DDT via an autoexplosion center cannot be obtained using the diffusion-limited model (2.45) and (2.46).

Noticing that all the models above are based on a single particle reaction rate multiplied by the particle number, the influence of neighboring particles on the reaction rate remains a research subject, particularly in a dense particle cloud.

C.2 Momentum Transfer

Forces exerted on the solid particles in a dilute particle–gas flow include drag, forces due to the gas pressure gradient and added gas mass on the particle surface, as well as the Basset history force [57, 138]. In the shock and detonation flow conditions, the drag is dominant; the other forces contribute less and can

be incorporated into an effective drag coefficient. Neglecting the influence of direct interactions between particles and compression within a particle, one can express the drag, f_p in newtons per cubic meter, formally by

$$f_\mathrm{p} = n_\mathrm{p} \frac{\pi d_\mathrm{p}^2}{4} C_\mathrm{d} \rho_\mathrm{g} (u_\mathrm{g} - u_\mathrm{p}) \left| u_\mathrm{g} - u_\mathrm{p} \right| / 2. \tag{2.53}$$

The drag coefficient $C_\mathrm{D} = C_\mathrm{D}(Re)$ for a spherical particle has been expressed in a standard drag curve based on incompressible flow experiments ($M \ll 1$), and equation fits of the standard drag curve can be found in textbooks [138]. The single particle drag coefficient has been extended to $C_\mathrm{D} = C_\mathrm{D}(Re, M)$ including the effect of flow compressibility in a range of relative flow Mach number [139, 140]. Effective drag coefficients of gas–particle flow have also been measured under unsteady or shocked flow conditions [57,141,142]. As an example, the following drag model has been applied to both dilute and dense particle–gas flow for $Re < 10^5$ [143]:

$$\begin{aligned}
C_\mathrm{d1} &= \frac{24}{Re} + \frac{4.4}{Re^{0.5}} + 0.42, \text{ if } \phi_\mathrm{p} \leqslant 0.08, \\
C_\mathrm{d2} &= \frac{4}{3\phi_\mathrm{g}} \left(1.75 + \frac{150\phi_p}{\phi_\mathrm{g}\, Re} \right), \text{ if } \phi_\mathrm{p} \geq 0.45, \\
C_\mathrm{d3} &= [(0.92\phi_\mathrm{p} - 0.08\phi_\mathrm{g})C_\mathrm{d2} + (0.45\phi_\mathrm{g} - 0.55\phi_\mathrm{p})C_\mathrm{d1}]/0.37, \text{ if } 0.08 < \phi_\mathrm{p} < 0.45,
\end{aligned} \tag{2.54}$$

where the term $24/Re$ is the Stokes model for $Re \ll 1$.

For a granular flow, Baer and Nuziato [52] introduced a compaction-related term, $p_\mathrm{g} \partial \phi_\mathrm{p} / \partial x$, that can be added in (2.53) for the rate of momentum transfer.

In handling the momentum transfer in detonation of solid particles suspended in low-density gas flow, the shock interaction time in which the shock front crosses a particle is several orders of magnitude smaller than the velocity relaxation time related to the drag. Thus, a solid particle is assumed to remain stationary as the shock front crosses it [57]. In contrast, for shock and detonation in high-density gas or condensed matter containing light solid particles, the shock interaction time can be comparable to the drag-induced velocity relaxation time owing to a significant increase in the initial material density ratio of fluid to solid particles. Thus, the stationary-particle assumption during the shock interaction time is no longer valid as $\rho_\mathrm{g}/\rho_\mathrm{s} \to 0.1 - 1$. Under strong shock conditions, the shock compression becomes an important force to accelerate a solid particle during the shock interaction time [39].

If a shock interaction time is defined to be $\tau_\mathrm{s} = D/d_\mathrm{p}$, where D is the shock velocity, the velocity transmission factor of a particle after a shock front crossing it can be expressed as

$$\alpha = \frac{u_\mathrm{p}(\tau_\mathrm{s})}{u_\mathrm{g}}, \tag{2.55}$$

where u_g and u_p are the postshock gas velocity and the mass-averaged particle velocity, respectively. The momentum transfer rate or the force acting on the solid-phase control volume containing n_p particles during the shock interaction process can then be written as

$$f_p = n_p m_p \frac{du_p}{dt} \approx n_p m_p \frac{u_p(\tau_s) - u_p(0)}{\tau_s} = n_p m_p \frac{\alpha u_g - u_p(0)}{\tau_s}. \tag{2.56}$$

Thus, the momentum transfer rate during the shock interaction process can be determined by the velocity transmission factor. The function of the velocity transmission factor can be obtained from mesoscale simulations [39, 68, 69].

C.3 Heat Transfer

Neglecting the influence of direct interactions between particles and compression within a particle, one can write the rate of heat transfer, Q_p in joules per cubic meter per second, due to convection as

$$Q_p = n_p \pi d_p^2 h(T_g - T_p) = n_p \pi d_p Nu \lambda_g (T_g - T_p), \tag{2.57}$$

where parameters h and λ_g are the coefficient of convection heat transfer to particles and the gas-phase thermal conductivity, respectively. The Nusselt number, $Nu = hd_p/\lambda_g$, is defined as the ratio of the convective heat transfer to the particle to the conductive heat transfer in the gas. Curve fits of the Nusselt number $Nu = Nu(Re, Pr)$ for a spherical particle in incompressible flow ($M \ll 1$) and its extension $Nu = Nu(Re, Pr, M)$ for compressible flow can be found in textbooks [57]. Fox et al. [144] suggested a model for $0 < M < 6$ and $Re < 10^4$:

$$Nu = \frac{2\exp(-M)}{1 + 17M/Re} + 0.459\, Re^{0.55} Pr^{0.33} \frac{1 + 0.5\exp(-17M/Re)}{1.5}. \tag{2.58}$$

This model was fitted to experimental data for continuum flow and partial transition flow ($M/Re < 0.5$). It becomes a model for incompressible flow when M approaches zero, and matches compressible subsonic results and supersonic measurements in rarefied gas flow.

In general, the heat conduction inside the particle must also be considered [12]. However, when the Biot number is small (the ratio of convective heat transfer to the particle to conductive heat transfer within the particle, $Bi = hd_p/6\lambda_p < 0.1$), a uniform temperature within the particle is quickly established and can therefore be assumed to simplify the problem. The rate of convective heat transfer in the detonation flow reaches a maximum value immediately behind the shock front where the temperature difference and the relative flow velocity are maximum. At this point, large particles can have a Biot number on the order of 0.1–1. As the particle is accelerated by the flow, the relative velocity and the rate of convective heat transfer drop significantly, thereby resulting in a small Biot number for most of the processes behind a shock.

The radiative heat transfer, $n_{\mathrm{p}}\pi d_{\mathrm{p}}^2\varepsilon\sigma(T_{\mathrm{g}}^4 - T_{\mathrm{p}}^4)$, can be added to the heat transfer (2.57). Under detonation conditions, however, the radiation heat transfer is small compared with the convective heat transferred to the particle and can often be neglected. In the granular flow model of Baer and Nuziato [52], an additional term $(-p_{\mathrm{p}}\Pi_{\mathrm{p}})$ was introduced in the heat transfer (2.57) to account for the heat loss due to irreversible dissipative compaction.

Similar to the rate of momentum transfer during the shock interaction process in dense gases or condensed matter containing solid particles, a temperature transmission factor of a particle after a shock front crossing it is introduced as [68]

$$\beta = \frac{T_{\mathrm{p}}(\tau_{\mathrm{s}})}{T_{\mathrm{g}}}, \tag{2.59}$$

where T_{g} and T_{p} are the postshock gas temperature and the mass-averaged particle temperature, respectively. The rate of heat transferred to the solid-phase control volume containing n_{p} particles during the shock interaction process can then be written as

$$q_{\mathrm{p}} = n_{\mathrm{p}}c_{\mathrm{p}}\frac{\mathrm{d}T_{\mathrm{p}}}{\mathrm{d}t} \approx n_{\mathrm{p}}c_{\mathrm{p}}\frac{T_{\mathrm{p}}(\tau_{\mathrm{s}}) - T_{\mathrm{p}}(0)}{\tau_{\mathrm{s}}} = n_{\mathrm{p}}c_{\mathrm{p}}\frac{\beta T_{\mathrm{g}} - T_{\mathrm{p}}(0)}{\tau_{\mathrm{s}}}, \tag{2.60}$$

where c_{p} is the specific heat capacity for the particle. Thus, the heat transfer rate during the shock interaction process can be determined by the temperature transmission factor. The function of the temperature transmission factor can be obtained from mesoscale simulations [68, 69].

C.4 Particle Number Change

Solid particle fragmentation was observed upon high-velocity impact on a hard wall [145]. A fragmentation process can be modeled by introducing an exchange source term for the particle number density based on the following assumptions:

1. A particle–wall interaction is divided into two steps: instantaneous fragmentation and nonsliding wall reflection.
2. The fragment sizes d_{frag} are grouped by n particle sizes:

$$d_{\mathrm{p}} = d_{n-1}, \quad \text{if } d_{n-1} \geq d_{\mathrm{frag}} > d_n \text{ for } n = 2, \ldots n, \tag{2.61}$$

   where $d_{n-1} > d_n$, with d_1 the original particle size.
3. The mass, momentum, and energy of the solid particle flow are conserved during the fragmentation process. Thus, fragmented particles have the same material density, velocity, and temperature as the original particles.

Under the above assumptions, the rate of particle number change due to high-velocity impact fragmentation on a wall can be expressed (e.g., $n = 2$) by

$$\Psi_{\mathrm{p1}} = \begin{cases} -n_{\mathrm{p1}}(x,t)\,\delta(t-t_{\mathrm{wall}}), & \text{for } x = x_{\mathrm{wall}}, d_{\mathrm{frag}} \leqslant d_2 \\ 0, & \text{otherwise} \end{cases}, \tag{2.62}$$

$$\Psi_{\mathrm{p2}} = -\left(d_1/d_2\right)^3 \Psi_{\mathrm{p1}}, \tag{2.63}$$

where t_{wall} is the time at which the particles arrive at the wall, x_{wall}. The corresponding rate of mass transfer between the particles with different sizes is

$$J_{\mathrm{p1}} = -J_{\mathrm{p2}} = \begin{cases} -\sigma_{\mathrm{p1}}(x,t)\,\delta(t-t_{\mathrm{wall}}), & \text{for } x = x_{\mathrm{wall}},\ d_{\mathrm{frag}} \leqslant d_2 \\ 0, & \text{otherwise} \end{cases}. \tag{2.64}$$

The above formulation can be straightforwardly extended to $n > 2$. Numerical implementation in the Eulerian approaches requires n sets of conservation equations for n particle sizes. Hence, the calculation becomes more efficient in the group Lagrangian approach when n becomes large.

The fragmentation size can be obtained using a model proposed by Grady [146, 147], based on the assumption that a moving spherical particle is subjected to an internal fracturing force due to the kinetic energy associated with outward expansion motion and the particle surface tension resistance:

$$d_{\mathrm{frag}} = B\left(K_{\mathrm{IC}}/\sigma_{\mathrm{m}}\right)^2, \tag{2.65}$$

where K_{IC} is the model I critical stress intensity with units of newtons per meter to the power two thirds and σ_{m} denotes the mean stress. $B = 5$ is used in [146] and $B = 6$ is used in [147]. If the elastic energy in the particle is included in the formulation, a value of $B = 1.875$ can be obtained.

From the elastic finite-element computations of a moving particle normally impacting on a wall, the maximum mean stress obtained can be correlated with the particle normal velocity by a curve fitting to

$$\sigma_{\mathrm{m}} = A\rho_{\mathrm{s}} u_{\mathrm{p}}^2, \tag{2.66}$$

where A is a fitting coefficient. $A = 1.46$ was obtained for an aluminum particle with elastic Young's modulus $E = 7.7 \times 10^{10}\,\mathrm{Pa}$, Poisson's ratio $\nu = 0.33$, density $\rho_{\mathrm{s}} = 2{,}700\,\mathrm{kg\ m^{-3}}$, and $K_{\mathrm{IC}} = 3.0 \times 10^7\,\mathrm{N\ m^{-3/2}}$. Therefore, Grady's model (2.65) can be revised to a relationship with the particle velocity:

$$d_{\mathrm{frag}} = \frac{B}{A^2}\left(\frac{K_{\mathrm{IC}}}{\rho_{\mathrm{s}} u_{\mathrm{p}}^2}\right)^2. \tag{2.67}$$

Solid particle fragmentation will also take place as a shock or detonation wave propagates in condensed matter containing solid particles [116]. The damage and fragmentation of reactive solid particles will change the surface properties and the size distribution of the particles, thus affecting the subsequent ignition and reaction behavior of the particles. While the fragmentation process can be modeled in the same approach discussed above using a source term of particle number change, the relevant physics and criteria for mechanical damage and fragmentation of specific particles are a subject of current research efforts.

Acknowledgements

My first gratitude is to Hans Grönig for initiating my work into multiphase shock and detonation research. He sets a lasting example of how scholarly work should be done. I particularly wish to thank John Lee, Martin Sichel, and Peter Wolanski for many insightful discussions. This chapter would not have been possible without dedicated contributions from Herbert Oliver, Andrias van de Ven, Peter Greilich, Gihui Geng, Paul Thibault, Robert Ripley, Keith Gerrard, Akio Yoshinaka, Julian Lee, and Vincent Tanquay.

References

1. Strauss, W.A.: Investigation of the detonation of aluminum powder–oxygen mixtures. AIAA J. **6**, 1753–1757 (1968)
2. Nettleton, M.A., Stirling, R.: Detonations in suspensions of coal dust in oxygen. Combust. Flame **21**, 307–314 (1973)
3. Cybulski, W.B.: Detonation of coal dust. Bull. Pol. Acad. Sci., **19**, 37–41 (1971)
4. Bartknecht, W.: Explosionen, pp. 5–72. Springer, Berlin (1978)
5. Fangrat, J., Glinka, W., Wolanski, P., Wolinski, M.: Detonation structure in organic dust–oxygen mixtures. Arch. Combust. **7**, 321–332 (1987)
6. Wolanski, P.: Deflagration and detonation of dust mixtures. Prog. Astronaut. Aeronaut. **132**, 3–31 (1991)
7. Kauffman, C.W., Wolanski, P., Arisoy, A., Adams, P.R., Maker, B.N., Nicholls, J.A.: Dust, hybrid and dusty detonations. Prog. Astronaut. Aeronaut. **94**, 221–240 (1984)
8. Peraldi, O., Veyssiere, B.: Experimental study of detonations in starch particle suspensions with O_2/N_2, H_2/O_2 and C_2H_4/O_2 mixtures. Prog. Astronaut. Aeronaut. **106**, 490–504 (1986)
9. Lee, J.H.S.: Dust explosion: an overview. In: Grönig, H. (ed.) Proceedings of 16th International Symposium of Shock Waves, Aachen, Germany, pp. 31–38. VCH, Weinheim (1988)
10. Wolanski, P., Lee, D., Sichel, M., Kauffman, C.W., Nicholls, J.A.: The structure of dust detonations. Prog. Astronaut. Aeronaut. **94**, 241–263 (1984)
11. Lee, D., Sichel, M.: The Chapman–Jouguet condition and structure of detonation in dust-oxidizer mixtures. Prog. Astronaut. Aeronaut. **106**, 505–521 **(1986)**
12. Fan, B.C., Sichel, M.: A comprehensive model for the structure of dust detonations. In: Proceedings of the 22nd International Symposium on Combustion, pp. 1741–1750. The Combustion Institute, Pittsburgh (1988)
13. Tulis, A.J., Selman, J.R.: Detonation tube studies of aluminum particles dispersed in air. In: Proceedings of the 19th International Symposium on Combustion, pp. 655–663. The Combustion Institute, Pittsburgh (1982)
14. Borisov, A.A., Khasainov, B.A., Saneev, E.L., Formin, I.B., Khomik, S.V., Veyssiere, B.: On the detonation of aluminum suspensions in air and in oxygen. In: Borisov, A.A. (ed.) Dynamic Structure of Detonation in Gaseous and Dispersed Media, pp. 215–253. Kluwer, Dordrecht (1991)

15. Gardner, B.R., Winter, R.J., Moore, M.J.: Explosion development and deflagration-to-detonation transition in coal dust/air suspensions. In: Proceedings of the 21st International Symposium on Combustion, pp. 335–343. The Combustion Institute, Pittsburgh (1986)
16. Zhang, F., Grönig, H.: Spin detonation in reactive particles-oxidizing gas flow. Phys. Fluids A **3**, 1983–1990 (1991)
17. Zhang, F., Grönig, H.: Two-headed detonation in reactive particle-oxidizing gas flow, Phys. Fluids A **4**, 2308–2315 (1992)
18. Zhang, F., Greilich, P., Grönig, H.: Propagation mechanism of dust detonations. Shock Waves **2**, 81–88 (1992)
19. Grönig, H.: Dust detonations. JSME Int. J. Ser. B **40** 1–15 (1997)
20. Zhang, F., Grönig, H., van de Ven, A.: DDT and detonation waves in dust–air mixtures. Shock Waves **11**, 53–71 (2001)
21. Ingignoli, W., Veyssiere, B., Khasainov, B.A.: Study of detonation initiation in unconfined aluminum dust clouds. In: Roy, G., Frolov, S., Kailasanath, K., Smirnov, N. (eds.) Gaseous and Heterogeneous Detonations, pp. 337–350. ENAS, Moscow (1999)
22. Zhang, F., Gerrard, K., Ripley, R., Tangury, V.: Unconfined aluminum particles–air detonation. In: Hannemann, K. (ed.) Proceedings of the 26th International Symposium on Shock Waves, Goettingen (2007)
23. Veyssiere, B., Manson, N.: Sur l'existence d'un second front de détonation des mélanges biphasiques hydrogène-oxygène-azote-particules d'aluminium. Note C. R. Acad. Sci. **295 II**, 335–338 (1982)
24. Veyssiere, B.: Structure of the detonations in gaseous mixtures containing aluminium particles in suspension. Prog. Astronaut. Aeronaut. **106**, 522–544 (1986)
25. Zhang, F., Thibault, P.A., Murray, S.B.: Transition from deflagration to detonation in an end multiphase slug. Combust. Flame **114**, 13–25 (1998)
26. Afanasieva, L.A., Levin, V.A., Tunik, Y.V.: Multifront combustion of two-phase media. Prog. Astronaut. Aeronaut. **87**, 394–413 (1983)
27. Khasainov, B.A., Veyssiere, B.: Steady, plane, double-front detonations in gaseous detonable mixtures containing a suspension of aluminium particles. Prog. Astronaut. Aeronaut. **114**, 284–299 (1988)
28. Veyssiere, B., Khasainov, B.A.: Structure and multiplicity of detonation regimes in heterogeneous hybrid mixtures. Shock Waves **4**, 171–186 (1995)
29. Wolinski, M., Teodorczyk, A., Wolanski, P., Klemens, R., Sichel, M., Nettleton, M.: Hybrid detonations in oat dust clouds in methane–air mixtures. Combust. Sci. Technol. **120**, 39–53 (1996)
30. Veyssiere, B., Ingignoli, W.: Existence of the detonation cellular structure in two-phase hybrid mixtures. Shock Waves **12**, 291–299 (2003)
31. Zhang, F., Murray, S.B., Gerrard, K.B.: Hybrid detonations in aluminum dust–gas mixtures. In: Proceedings of the 19th International Colloquium on the Dynamics of Explosions and Reactive Systems, Hakone, pp. 167.1–167.4 (2003)
32. Zhang, F., Murray, S.B., Gerrard, K.B.: Hybrid detonation waves in heterogeneous explosive mixtures. In: Proceedings of the 18th International Symposium on Military Aspects of Blast and Shock, Bad Reichenhall, pp. 75.1–75.14 (2004)
33. Zhang, F., Murray, S.B., Gerrard, K.B.: Hybrid detonation waves. In: Proceedings of the 20th International Colloquium on the Dynamics of Explosions and Reactive Systems, Montreal, pp. 217.1–217.12 (2005)

34. Tulis, A.J., Sumida, W.K., Dillon, J., Comeyne, W., Heberlein, D.C.: Submicron aluminum particle size influence on detonation of dispersed fuel-oxidizer powders. In Proceedings of International Symposium on Hazards, Prevention, and Mitigation of Industrial Explosion, Schaumberg, pp. 68–76 (1998)
35. Li, Y.-C., Alexander, C.G., Wolianski, P., Kauffman, C.W., Sichel, M.: Experimental investigations of accelerating flames and transition to detonation in layered grain dust. Prog. Astronaut. Aeronaut. **154**, 170–184 (1993)
36. Vasil'ev, A.A., Gavrilenko, T.P., Topchian, M.E.: On the Chapman–Jouguet surface in multi-headed detonations. Astronaut. Acta **17**, 499–502 (1972)
37. Edwards, D.H., Jones, A.T., Phillips, D.E.: The location of the Chapman–Jouguet surface in a multiheaded detonation wave. J. Phys. D **9**, 1331–1342 (1976)
38. Weber, M., Olivier, H.: The thickness of detonation waves visualised by slight obstacles. Shock Waves **13**, 351–365 (2003)
39. Zhang, F., Thibault, P.A., Link, R.: Shock interaction with solid particles in condensed matter and related momentum transfer. Proc. R. Soc. Lond. A, **459**, 705–726 (2003)
40. Zeldovich, Ya.B., Kompaneets, A.S.: Theory of Detonation, pp. 133–205. Academic, London (1960)
41. Wood, W.W., Kirkwood, J.G.: Diameter effect in condensed explosives: the relation between velocity and radius of curvature of the detonation wave. J Chem. Phys. **22**, 1920–1924 (1954)
42. Kuznetsov, N.M.: Nonuniqueness and stability of detonation modes. Sov. Phys. JETP **25** 199–204 (1967)
43. Erpenbeck, J.J.: Stability of idealized one-reaction detonations. Phys. Fluids **7**, 684–696 (1964)
44. Fickett, W., Wood, W.W.: Flow calculations for pulsating one-dimensional detonations. Phys. Fluids **9**, 903–916 (1966)
45. Abouseif, G.E., Toong, T.Y.: Theory of unstable one-dimensional detonations. Combust. Flame **45**, 67–94 (1982)
46. Lee, H.I., Stewart, D.S.: Calculation of linear detonation instability: one-dimensional instability of planer detonations. J. Fluid Mech. **216**, 103–132 (1990)
47. He, L., Lee, J.H.S.: The dynamics limit of one-dimensional detonations. Phys. Fluids **7**, 1151–1158 (1995)
48. Sharpe, G.J.: Linear stability of pathological detonations. J. Fluid Mech. **401**, 311–338 (1991)
49. Ng, H.D., Lee, J.H.S.: Direct instability of detonation with a multi-step reaction scheme. J. Fluid Mech. **476**, 179–211 (2003)
50. Gelfand, B.E., Frolov, S.M., Nettleton, M.A.: Gaseous detonations – a selective review. Prog. Energy Combust. Sci. **17**, 327–371 (1991)
51. Powers, J.M., Stewart, D.S., Krier, H.: Theory of two-phase detonations – part II: structure. Combust. Flame **80**, 280–303 (1990)
52. Baer, M.R., Nunziato, J.W.: A two-phase mixture theory for the deflagration-to-detonation transition (DDT) in reactive granular materials. Int. J. Multiphase Flow **12**, 861–889 (1986)
53. Powers, J.M., Stewart, D.S., Krier, H.: Theory of two-phase detonations – part I: modeling. Combust. Flame **80**, 264–279 (1990)
54. Zhang, F., Frost, D.L., Thibault, P.A., Murray, S.B.: Explosion dispersal of solid particles. Shock Waves **10**, 431–443 (2001)

55. Zhang, F.: Numerical studies of detonation propagation in mixtures of combustible gases and inert dust. In: Gottlieb, J.J., Ethier C.R. (eds.) The 2nd Conference of the CFD Society of Canada, pp. 261–268 (1994)
56. Kapila, A.K., Son, S.F., Bdzil, J.B., Menikoff, R., Stewart, D.S.: Two-phase modeling of DDT, structure of the velocity-relaxation zone. Phys. Fluids A **9**, 3885–3897 (1997)
57. Rudinger, G.: Fundamentals of Gas–Particle Flow. Elsevier, Amsterdam (1980)
58. Zhang, F., Lee, J.H.S.: Friction-induced oscillatory behaviour of one-dimensional detonations. Proc. R. Soc. Lond. A **446**, 87–105 (1994)
59. Zhang, F., Chue, R.S., Frost, D.L., Lee, J.H.S., Thibault, P., Yee, C.: Effects of area change and friction on detonation stability in supersonic ducts. Proc. R. Soc. Lond. A **449**, 31–49 (1995)
60. Korobeinikov, V.: Formation of zone with high particle concentrations in dusty gases. Prog. Astronaut. Aeronaut. **132**, 287–292 (1991)
61. Fickett, W., Davis, W.C.: Detonation, pp. 153–191. University of California Press, Berkeley (1979)
62. Khasainov, B.A., Veyssiere, B., Ingignoli, W.: Numerical simulation of detonation cell structure in hydrogen–air mixture loaded by aluminum particles. In: Roy, G., Frolov, S., Netzer, D., Borisov A. (eds.) High-Speed Deflagration and Detonation: Fundamentals and Control, pp. 163–174. ELEX-KM, Moscow (2001)
63. Hayashi, A.K., Fuyuto, T., Fujiwara, T.: Triple-shock structure in dusty gas detonations. In: Sturtevant, B., Shepherd, J.E., Hornung H.G. (eds.) Proceedings of the 20th International Symposium on Shock Waves, pp. 1071–1076. World Scientific, Singapore (1996)
64. Fedorov, A.V., Khmel, T.A.: Types and stability of detonation flows of aluminum particles in oxygen. Fiz. Goreniya Vzryva **32**(2), 74–85 (1996)
65. Fedorov, A.V., Khmel, T.A.: Determination of nonideal self-sustained detonation regimes of aluminum particles in air. Fiz. Goreniya Vzryva **34**(5), 95–102 (1998)
66. Benkiewicz, K., Hayashi, A.K.: One-dimensional parametric studies of an aluminum–dust combustion model for numerical simulations of detonation waves. AIAA J. **44**, 608–619 (2006)
67. Zhang, F., Gerrard, K.B., Ripley, R.: Reaction mechanism of aluminum particles–air detonation. In: Proceedings of the 7th International Symposium on Hazards, Prevention and Mitigation of Explosion, St. Petersburg, Vol. 2, pp. 223–237 (2008)
68. Ripley, R., Zhang, F., Lien, F.S.: Shock interaction of metal particles in condensed explosive detonation. In: Furnish, M.D., Elert, M., Russel, T.P., White C.T. (eds.) Shock Compression of Condensed Matter – 2005, pp. 499–502. American Institute of Physics, Melville (2006)
69. Ripley, R., Zhang, F., Lien, F.S.: Detonation interaction with metal particles in explosives. In: Proceedings of 13th International Symposium on Detonation, pp. 214–223. Office of Naval Research ONR 351-07-01 (2006)
70. Zhang, F., Grönig, H.: Transition to detonation in cornstarch dust–oxygen and –air mixtures. Combust. Flame **86**, 21–32 (1991)
71. Urtiew, P.A., Oppenheim, A.K.: Experimental observation of the transition to detonation on an explosive gas. Proc. R. Soc. Lond. A **295**, 13–29 (1966)
72. Lee, J.H.S., Moen, I.O.: The mechanism of transition from deflagration to detonation in vapour explosions. Prog. Energy Combust. Sci. **6**, 359–389 (1980)

73. Zhang, F., Murray, S.B., Gerrard, K.B.: Aluminium dust–air detonation at elevated pressures. Shock Waves **15**, 313–324 (2006)
74. Craven, A.D., Greig, T.R.: The development of detonation over-pressures in pipelines. Chem. Eng. Symp. **25**, 41–50 (1968)
75. Kogarko, S.M.: Investigation of the pressure at the end of a tube in connection with rapid nonstationary combustion. Sov. Phys. Tech. Phys. **28**, 2041 (1958)
76. Tulis, A.J.: On the unconfined detonation of aluminum powder-air clouds. In: Wolanski, P. (ed.) 1st International Colloquium on Explosibility of Industrial Dusts, Warsaw, Poland, pp. 178–186 (1984)
77. Dove, J.E., Wagner, H.G.: A photographic investigation of the mechanisms of spinning detonation. In: Proceedings of the 8th International Symposium on Combustion, pp. 589–600. The Combustion Institute, Pittsburgh (1960)
78. Manson, N.: Propagations des detonations et des deflagrations dans les melanges gaseaux.Off. Nat. Etud. Rech. Aeronaut. Inst. Fr. Pet. Paris C. R. Acad. Sci. **222**, 46–51 (1947)
79. Denisov, Y.N., Troshin, Y.K.: Structure of gaseous detonation in tubes. Z. Tekh. Fiz. **30**, 450–459 (1960)
80. Voitsekhovskii, B.V., Mitrofanov, V.V., Topchian, M.E.: Structure of a detonation front in gases. Izdatel'stvo Sibirskogo Otdeleniya Akademiya Nauk SSSR, Novosibirsk (1963). English translation: Wright-Patterson Air Force Base Report FTD-MT-64-527 (AD0633821) (1966)
81. Schott, G.L.: Observations of the structure of spinning detonation. Phys. Fluids **8**, 850–865 (1965)
82. Mitrofanov, V.V., Soloukhin, R.I.: The diffraction of multi-front detonation waves. Sov. Phys. Dokl. **9**, 1055–1058 (1965)
83. Strehlow, R.A.: The nature of transverse waves in detonations. Astronaut. Acta **14**, 539–548 (1969)
84. Lundstrom, E.A., Oppenheim, A.K.: On the influence of nonsteadiness on the thickness of the detonation wave. Proc. R. Soc. Lond. A **310**, 463–478 (1969)
85. Edwards, D.H., Hooper, G., Job, E.M., Parry, D.J.: The behaviour of the frontal and transverse shock in gaseous detonation waves. Acta Astronaut. **15**, 323–333 (1970)
86. Strehlow, R.A., Crooker, A.J.: The structure of marginal detonation waves. Acta Astronaut. **1**, 303–315 (1974)
87. Lee, J.H.S.: Dynamic parameters of gaseous detonations. Annu. Rev. Fluid Mech. **16**, 311–336 (1984)
88. Shepherd, J.E., Pintgen, F., Austin, J.M., Eckett, C.A.: The structure of the detonation front in gases. AIAA Pap. 2002-0773 (2002)
89. Shepherd, J.E.: Detonation: a look behind the front. In: Proceedings of the 19th International Colloquium on the Dynamics of Explosions and Reactive Systems, Hakone, Japan, pp. 218.1–218.15 (2003)
90. Zeldovich, Y.B., Kogarko, S.M., Simonov, M.N.: An experimental investigation of spherical detonation of gases. Sov. Phys. Tech. Phys. **1**, 1689–1713 (1956)
91. Benedick, W.B., Guirao, C.M., Knystautas, R., Lee, J.H.: Critical charge for direct initiation of detonation in gaseous fuel–air mixtures. Prog. Astronaut. Aeronaut. **106**, 181–202 (1986)
92. Lee, J.H.S., Knystautas, R., Guirao, C.: The link between cell size, critical tube diameter, initiation energy and detonability limits. In: Lee, J.H.S., Guirao, C.M. (eds.) Fuel–Air Explosions, pp. 157–187. University of Waterloo Press, Waterloo (1982)

93. Vasil'ev, A.A.: Gaseous fuels and detonation hazards. In: Eisenreich, N. (ed.) Proceedings of 28th ICT Conference, Karlsruhe, pp. 50.1–50.14 (1997)
94. Dahab, O., Kapuscinski, M., Wolanski, P.: Influence of dust parameters on detonation velocity, structure and limits. Prog. Astronaut. Aeronaut. **133**, 356–370 (1989)
95. Zhang, F., Grönig, H.: Detonability of organic dust–air mixtures. Prog. Astronaut. Aeronaut. **154**, 195–215 (1993)
96. Kogarko, S.M., Zeldovich, Ya.B.: On detonation of gas mixtures. Dokl. Akad. Nauk SSSR **63**, 553–556 (1948)
97. Shchelkin, K.I., Troshin, Ya.K.: Gasdynamics of Combustion. Academy of Sciences, Moscow. Translated by Kuvshinoff, B.W., Holtschlag, L. Mono Book, Baltimore (1965)
98. Strehlow, R.A., Engel, C.D.: Transverse waves in detonation II: structure and spacing in H_2–O_2, C_2H_2–O_2, C_2H_4–O_2, and CH_4–O_2 systems. AIAA J. **7**, 492–496 (1969)
99. Glassman, I.: Combustion, pp. 168–193. Academic, New York (1977)
100. Friedman, R., Macek, A.: Ignition and combustion of aluminum particles in hot ambient gases. Combust. Flame **6**, 9–19 (1962)
101. Fontijn, A., Felder, W.: HTFFR Kinetic Studies of $Al + CO_2 \rightarrow AlO + CO$ from 300 to 1,800 K, a non-Arrenhius reaction. J. Chem. Phys. **67**, 1561 (1977)
102. King, M.K.: Modeling of single particle aluminum combustion in CO_2–N_2 atmospheres. In: Proceedings of the 17th International Symposium on Combustion, pp. 1317–1328. The Combustion Institute, Pittsburgh (1978)
103. Gurevich, M.A., Lapkina, K.I., Ozerov, E.S.: Ignition limit of aluminum particles. Combust. Explos. Shock Waves **6**, 172–175 (1970)
104. Davis, A.: Solid propellants: the combustion of particles of metal ingredients. Combust. Flame **7**, 227–234 (1963)
105. Pokhil, P.F., Belyayev, A.F., Frolov, Y.V., Logachev, V.S., Kotkov, A.I.: Combustion of powdered metal in active media. Nauka, Moscow (1972). US Air Force Foreign Technology Division Translation FTD-MT-24-551-73 (AD0769576) (1973)
106. Foelsche, R.O., Burton, R.I., Krier, H.: Ignition and combustion of aluminum particles in $H_2/O_2/N_2$ combustion products. J. Propuls.. Power **117**, 1001–1008 (1998)
107. Melcher, J.C., Burton, R.L., Krier, H.: Combustion of aluminum particles in solid rocket motor flows. Prog. Astronaut. Aeronaut. **185**, 723–747 (2000)
108. Melcher, J.C., Krier, H., Burton, R.L.: Burning aluminum particles inside a laboratory-scale solid rocket motor. J. Propuls.. Power **18**, 631–640 (2002)
109. Borisov, A.A., Gelfand, B.E., Timofeev, E.I., Tsyganov, S.A., Khomic, S.V.: Ignition of dust suspensions behind shock waves. Prog. Astronaut. Aeronaut. **96**, 332–339 **(1984)**
110. Boiko, V.M., Fedorov, A.V., Formin, V.M., Papyrin, A.N., Soloukhin, R.I.: Ignition of small particles behind shock waves. Prog. Astronaut. Aeronaut. **87**, 71–87 (1982)
111. Sichel, M., Baek, S.W., Kauffman, C.W., Maker, B., Nicholls, J.A., Wolanski, P.: The shock wave ignition of dusts. AIAA J. **23**, 1374–1380 (1985)
112. Geng, J.H., van de Ven, A., Zhang, F., Grönig, H.: Ignition delay of the cornstarch dust behind an incident shock wave. In: Proceedings of the 14th International Colloquium on the Dynamics of Explosions and Reactive Systems, Coimbra (1993)

113. Servaites, J., Krier, H., Melcher, J.C., Burton, R.L.: Ignition and combustion of aluminum particles in shocked $H_2O/O_2/Ar$ and $CO_2/O_2/Ar$ mixtures. Combust. Flame **125**, 1040–1054 (2001)
114. Tanguay, V., Goroshin, S., Higgins, A.J., Zhang, F.: Aluminum particle combustion in high-speed detonation products. Combust. Sci. Technol. **181**, 670–693 (2009)
115. Lee, J.J., Zhang, F.: Burning properties of aluminum in H_2O or CO_2 gas. In: Proceedings of the 20th International Colloquium on the Dynamics of Explosions and Reactive Systems, Montreal, pp. 179.1–179.7 (2005)
116. Yoshinaka, A., Zhang, F., Wilson, W.H.: Effect of shock compression on aluminum particles in condensed media. In: Elert, M., Furnish, M.D., Chau, R., Holmes, N., Nguryen J. (eds.) Shock Compression of Condensed Matter – 2007, pp. 1057–1060. APS Melville, New York (2007)
117. Fay, J.A.: Two-dimensional detonations: velocity deficits. Phys. Fluids **2**, 283–289 (1959)
118. Manson, N., Brochet, C., Brossard, J., Pujol, Y.: Vibratory phenomena and instabilities of self-sustained detonations in gases. In: Proceedings of the 9th International Symposium on Combustion, pp. 461–469. Academic, London (1963)
119. Dabora, E.K., Nicholls, J.A., Morrison, R.B.: The influence of a compressible boundary on the propagation of gaseous detonations. In: Proceedings of the 10th International Symposium on Combustion, pp. 817–830. The Combustion Institute, Pittsburgh (1965)
120. Vasiliev, A.A.: Gas detonation of a free mixture column. Lavrent'yev Institute of Hydrodynamics, Siberian Branch of the USSR Academy of Sciences, Novosibirsk, (1980)
121. Edwards, D.H., Thomas, G.O., Nettleton, M.A.: The diffraction of a planar detonation wave at an abrupt area change. J. Fluid Mech. **95**, 79–96 (1979)
122. Murray, S.B., Lee, J.H.: The influence of physical boundaries on gaseous detonation waves. Prog. Astronaut. Aeronaut. **106**, 329–355 (1986)
123. Moen, I.O., Sulmistras, A., Thomas, G.O., Bjerketvedt, D., Thibault, P.A.: Influence of cellular regularity on the behavior of gaseous detonations. Prog. Astronaut. Aeronaut. **106**, 220–243 (1986)
124. Moen, I.O., Donato, M., Knystautas, R., Lee, J.H.: The influence of confinement on the propagation of detonations near the detonability limits. In: Proceedings of the 18th International Symposium on Combustion, pp. 1615–1622. The Combustion Institute, Pittsburgh **(1981)**
125. Zhang, F.: Detonation waves in dust media: a review. AIAA Pap. 2002-0772 (2002)
126. Gogulya, M.F., Makhov, M.N., Dolgoborodov, A.Yu., Brazhnikov, M.A., Arkhipov, V.I., Shchetinin, V.G.: Mechanical sensitivity and detonation parameters of aluminized explosives. Fiz. Goreniya Vzryva **40**, 82–95 (2004)
127. Marsh, S.P.: LASL Shock Hugoniot Data. University of California Press, Berkeley (1980)
128. Walsh, J.M., Christian, R.H.: Equation of state of metals from shock wave measurements. Phys. Rev. **97**, 1544–1556 (1955)
Note to reference stylist: Please add the publisher city location. N
129. Lee, E., Hornig, H.C., Kury, J.W.: Adiabatic expansion of high explosive detonation products. Lawrence Livermore National Laboratory report UCRL-50422. Lawrence Livermore National Laboratory, Livermore, CA (1968)

130. Fried, L.E., Howard, W.M., Souers, P.C.: Cheetah 2.0 User's Manual. Lawrence Livermore National Laboratory report UCRL-MA-117541 revision 5. Lawrence Livermore National Laboratory, Livermore, CA (1998)
131. Lun, C.K.K., Savage, S.B., Jeffrey, D.J., Chepurniy, N.: Kinetic theories for granular flow: inelastic particles in couette flow and slightly inelastic particles in a general flowfield. J. Fluid Mech. **140**, 223–256 (1984)
132. Gidaspow, D.: Multiphase flow and fluidization. Academic, London (1994)
133. Fan, B.C., Chen, Z.H., Jiang, X.H., Li, H.Z.: Interaction of a shock wave with a loose dusty bulk layer. Shock Waves **16**, 179–187 (2007)
134. Blazer, G., Simonin, O., Boelle, A., Lavieville, J.: A Unifying modelling approach for the numerical prediction of dilute and dense gas-solid two phase flow. In: Proceedings of 5th International Conference on Circulating Fluidized Bath, Beijing (1996)
135. Gonor, A.: High-pressure vaporization and boiling of condensed material: a generalized Clausius–Clapeyron equation. In: Furnish, M.D., Thadhani, N.N., Horie, Y. (eds.) Shock Compression of Condensed Matter – 2001, pp. 63–66. American Institute of Physics, Melville (2002)
136. Price, E.W.: Combustion of metalized propellants. Prog. Astronaut. Aeronaut. **90**, 479–513 (1984)
137. Elperin, I., Igra, O., Ben-Dor, G.: Analysis of normal shock wave in a carbon particle-laden oxygen gas. Trans. ASME **108**, 354–359 (1986)
138. Schlichting, H.: Boundary-Layer Theory, 7th edn. McGraw-Hill, New York (1979)
139. Bailey, A.B.: Sphere drag coefficient for supersonic speeds in continuum and free-molecule flows. J. Fluid Mech. **65**, 401–410 (1974)
140. Henderson, C.B.: Drag coefficient of spheres in continuum and rarefied flows. AIAA J. **14**, 707–708 (1976)
141. Igra, O., Takayama, K.: Shock tube study of the drag coefficient of a sphere in a nonstationary flow. In: Takayama K. (ed.) Proceeding of the 18th International Symposium of Shock Waves, pp. 491–497. Springer, Berlin (1991)
142. Sommerfeld, M., Decker, S.: On the importance of the Basset history term on the particle motion induced by a plane shock wave. In: Brun, R., Dumitrescu L.Z. (eds.) Proceedings of the 19th International Symposium of Shock Waves, pp. 37–42. Springer, Berlin (1995)
143. Smirnov, N.N.: Combustion and detonation in multi-phase media, initiation of detonation in dispersed film systems behind a shock wave. Int. J. Heat Mass Transfer **31**, 779–793 (1988)
144. Fox, T.W., Rackett, C.W., Nicholls, J.A.: Shock wave ignition of magnesium powders. In: Proceedings of the 11th International Symposium on Shock Waves and Tubes, Seattle, pp. 262–268 (1978)
145. Frost, D.L., Goroshin, S., Janidlo, S., Pryszlak, J., Levine, J., Zhang, F.: Fragmentation of reactive metallic particles during impact with a plate. In: Furnish, M.D., Gupta, Y.M., Forbes, J.W. (eds.) Shock Compression of Condensed Matter – 2003, pp. 451–454. American Institute of Physics, Melville (2004)
146. Grady, D.E.: Local inertial effects in dynamic fragmentation. J. Appl. Phys. **53**, 322–325 (1981)
147. Yew, C.H., Grady, D.E., Lawrence, R.J.: A simple model for debris clouds produced by hypervelocity particle impact. Int. J. Impact Eng. **14**, 851–862 (1993)